TECHNISCHE UNIVERSITÄT
CHEMNITZ

Integrated Micro-Supercapacitor: Design, Fabrication, and Functionalization

von der Fakultät für Elektrotechnik und Informationstechnik
der Technischen Universität Chemnitz

genehmigte

Dissertation

zur Erlangung des akademischen Grades

Doktor der Ingenieurwissenschaften
(Dr.-Ing.)

vorgelegt

von: M. Sc. Jinhui Wang

geboren am: 12. Januar 1988 in Shandong, China

eingereicht am: 19. November 2019

Gutachter: Prof. Dr. Prof. h.c. Oliver G. Schmidt
Prof. Dr. Feng Zhu

Tag der Verleihung: 15. Juli 2020

Bibliografische Beschreibung

Jinhui Wang

Integrated Micro-Supercapacitor: Design, Fabrication, and Functionalization

Dissertation an der Fakultät für Elektrotechnik und Informationstechnik der Technischen Universität Chemnitz, Dissertation, 2019

137 Seiten, 59 Abbidungen, 1 Tabellen, 232 Referenzen

Abstract

Owing to the advantages of high power density, fast charge/discharge rates as well as long lifetime, micro-supercapacitor (MSC) has drawn much attention for its potential application in miniaturized electronics. Many efforts have been devoted to the design and fabrication of high-performance MSCs. On the other hand, the integration of MSCs with multiple functional materials and devices has emerged with the development of portable and wearable microelectronics. To date, the biggest challenge in research is to develop a reliable and smart fabrication technology/strategy, which can integrate diverse objective materials into compact devices.

Rolled-up nanotechnology is a unique approach to self-assemble 2D nanomembranes into 3D structures by using strain engineering. This self-assembly process smartly combines top-down and bottom-up methods to pattern functional nanomaterials into ordered 3D micro- and nanostructure arrays. One promising advantage of this approach is that such a self-assembled structure can endow micro-devices with functionality and high performance under a limited footprint area.

The first part of this thesis focuses on the fabrication of planar interdigital MSCs with thermo-responsive function. Based on this work, the second part involves the research on novel tubular MSC which was fabricated by employing shapeable materials and strain engineering. A polymeric framework consisting of swelling hydrogel and polyimide layers ensures excellent ion transport between electrodes and provides efficient self-protection of the tubular MSC against external compression. Such tubular device also exhibits excellent areal capacitance, and an improved cycling stability compared to that of planar MSCs. The third part introduces the step-by-step experiments towards the fabrication and optimization of inorganic strained layer-based tubular MSC. Al_2O_3/Ni/Cr/Al_2O_3 strained nanomembrane is designed and can successfully drive the rolling up of MnO_2 electrodes with a high yield under magnetic fields.

Keywords: strain engineering, energy storage, supercapacitor, miniaturization, integration, functionalization

Table of Contents

List of Abbreviations and Acronyms

Micro-supercapacitor	**MSC**
Internet of Things	**IoT**
Microelectromechanical systems	**MEMS**
Three-dimensional	**3D**
Double-layer capacitor	**EDLC**
Activated carbons	**ACs**
Carbon nanotubes	**CNTs**
Helmholtz plane	**IHP**
Outer Helmholtz plane	**OHP**
Poly(3,4-ethylenedioxythiophene)	**PEDOT**
3,4-ethylenedioxythiophene	**EDOT**
Fiber-based MSCs	**FSCs**
Ultraviolet	**UV**
Nanoelectromechanical systems	**NEMS**
Physical vapor deposition	**PVD**
Lithium phosphorous oxynitride	**LiPON**
Carbide-derived carbon	**CDC**
Polyethylene terephthalate	**PET**
Chemical vapor deposition	**CVD**
Piezoelectric supercapacitor	**PESC**
Triboelectric nanogenerator	**TENG**
Photo-rechargeable supercapacitor	**PRSC**
Dye-sensitized solar cell	**DSSC**
Electrochromic	**EC**
Polyaniline	**PANI**
Polyacrylic acid	**PAA**
Polyurethane	**PU**
One dimensional	**1D**
Diarylethene derivatives	**DAEs**
Miniaturized energy autonomous systems	**MEAS**
Ultracompact capacitors	**UCCaps**

Methylcellulose	**MC**
Li-ion batteries	**LIBs**
Polydimethylsiloxane	**PDMS**
Poly(ethylene-alt-maleic anhydride)	**PEMA**
N-(2-hydroxyethyl) methacrylate	**HEMA**
N-(2-hydroxyethyl) methacrylamide	**HEMAm**
Indium gallium zinc oxide	**IGZO**
Atomic layer deposition	**ALD**
Counter electrode	**CE**
Working electrode	**WE**
Reference electrode	**RE**
Scanning electron microscopy	**SEM**
Focused ion beam	**FIB**
Cyclic voltammetry	**CV**
Galvanostatic charge/discharge	**GCD**
Polyimide	**PI**
Diethylenetriaminepentaacetic acid	**DTPA**
Polyvinyl alcohol	**PVA**
Sodium dodecyl sulfate	**SDS**
Internal resistance	**IR**
Electrochemical impedance spectra	**EIS**
Reactive-ion etching	**RIE**

Chapter 1. Introduction

1.1. General background

With the rapid development of Internet of Things (IoT), human life has become more intelligent and convenient. The application of miniaturized electronic devices in IoT, such as wireless sensor networks, microelectromechanical systems (MEMS), portable electronics, etc., has triggered tremendous research activities on micro-scale energy storage units (Figure 1).[1–4] On the other hand, green energy harvesters (*e.g.* solar cells and nanogenerators) have much promise for sustainable self-powered devices. Due to the lack of power storage capacity and stability, the energy harvesters are required to work with energy storage units together.

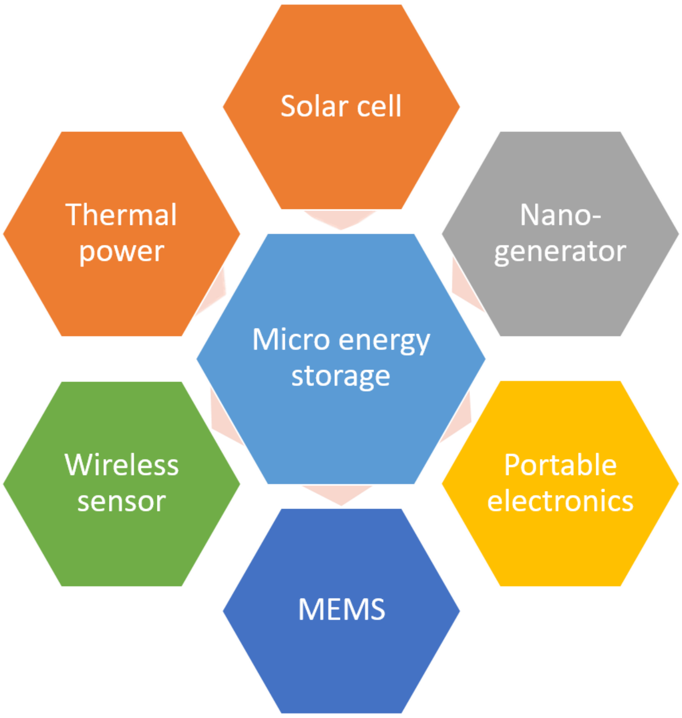

Figure 1.1. Schematic diagram showing the applications of micro energy storage.

Generally, micro-batteries are primary choices for the self-powered systems. The sufficient energy density of micro-batteries can ensure a stable current supply or deliver a high peak current.[5–8] However, the charge/discharge mechanism of batteries resulted in a limited lifetime and power density,[9,10] thus restricting the further application in smart microelectronics where high-power storage micro-devices are highly demanded.[11] Despite the lower energy density than batteries, micro-supercapacitors (MSCs) can make up for some shortcomings of batteries such as longer operating lifetime (> 100 000 cycles), faster charge/discharge rates as well as higher power density.

1.2. Motivation of this work

1.2.1. Integration of micro-supercapacitors

The miniaturization of energy storage significantly decreases the footprint area and thus more functional devices have the opportunity to be integrated with MSCs into microelectronics. This versatile integration within a limited space/footprint area can greatly promote the development of microelectronic devices with higher working efficiency and reduced maintenance/energy cost. To date, the biggest challenge in MSC's research is to develop a reliable and smart fabrication strategy which can integrate diverse objective materials into compact devices with high electrochemical performance. This requires a good compatibility of MSC with other electronic components in the whole fabrication process. For instance, high-temperature treatment or inevitable chemical residue in MSCs may generate a negative influence on the integration of multiple-function devices.

1.2.2. Thermo-responsible micro-supercapacitors

In general, the operating temperatures of processors and circuit boards in a mobile phone or computer should be critically controlled to be below 80 °C. Previous studies on preventing thermal runaway have been focused on using thermally controlled functional modules. Nevertheless, these modules are not suitable for on-chip electronics due to space limitation, process complexity, and cost-efficiency. Thus a rational design of thermal control systems towards high performance, safe on-chip electronics is highly attractive.

1.2.3. 3D tubular functional micro-supercapacitors

Nowadays, considerable attention has been focused on developing multifunctional MSCs. These multi-function integrations can promote the potential applications of MSCs in intelligent on-chip microelectronics and wearable/portable electronics. Currently, it is still a challenge to increase the integration degree of multiple functions on a single device. This is mainly reflected by how much the performance of overall integrated device/materials declines compared to the individual devices/materials. On the other hand, the space utilization and circuit design of integrated devices are another important considerable factor.

Conventional capacitors used in electronic circuits often adopt a cylinder shape, in which the capacitor laminates consisting of planar electrodes and insulating layers are folded or wound into “Swiss-roll” structures. This origami design compresses large-area membranes into compact tubular structures, massively improving the form factor and electrochemical performance in electronic circuits. Besides, the cylinder geometry can provide fixation and mechanical protection, which are required for the integration of capacitors into circuits by automated pick-and-place processes. Hence, inspired by origami art, the technology transfer of this assembling route into the microscale represents an efficient strategy for constructing integrated three-dimensional (3D) MSCs with high electrochemical performance under a limited footprint area.

1.3. Dissertation structure

This dissertation is organized in the following way:

Chapter 1 introduces the research background of micro-supercapacitors and the motivation of this work.

Chapter 2 gives an overview of micro-supercapacitors, including the configuration, fabrication strategies, fabrication methods of active materials, and the functionalization.

Chapter 3 gives a detailed overview of rolled-up nanotechnology, including the self-assembly of inorganic nanomembranes and polymeric layer stacks.

Chapter 4 commences the overall experimental methods in this work. MSC fabrication, characterization, and electrochemical measurements are also introduced.

Chapter 5 presents the microfabrication of planar interdigital micro-supercapacitors with the function of thermo-response. Wafer-scale fabrication of these functional devices is also demonstrated.

Chapter 6 demonstrates a novel tubular micro-supercapacitors with greatly reduced footprint area. Tubular micro-supercapacitors based on this platform have improved areal electrochemical performance. The polymeric framework as the strained layer ensures ion transport between electrodes and provides efficient self-protection of device against external compression.

Chapter 7 discusses the exploration of the rolling of inorganic nanomembranes. With high assembly yield and high-aspect-ratio, Al_2O_3/Ni/Cr/Al_2O_3 nanomembranes are successfully rolled up in magnetic fields.

Chapter 8 concludes the whole work in this dissertation and presents an outlook for future work.

Chapter 2. Overview of micro-supercapacitors

2.1. Introduction to MSCs

2.1.1. Capacitor

A conventional capacitor consists of two stacked metal plates which are separated by the dielectric layer, as shown in Figure 2.1. This type of capacitor is charged by applying a voltage across the electrodes, causing positive and negative charges respectively migrating towards two electrode surfaces. However, the energy storage capability is generally limited by its intrinsic charge storage in the electrostatic field.

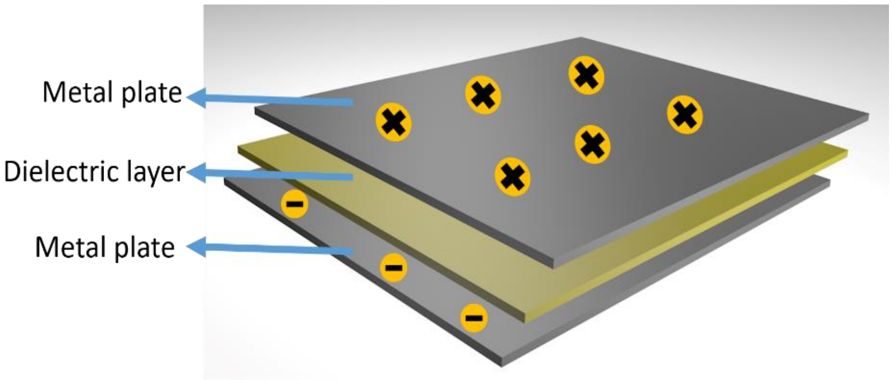

Figure 2.1. Schematic of a conventional capacitor

2.1.2. Electric double-layer capacitor

In 1957, the earliest supercapacitor, also known as an electric double-layer capacitor (EDLC), was invented to provide high energy density and power density for electronic components. EDLCs store energy based on the ion adsorption/desorption during the charge/discharge processes on the electrolyte/electrode interface.[12] This process involves highly reversible non-faradaic reactions, thus endowing EDLCs fast energy storage and long cycling life. Therefore, it has a stronger capability for the charge storage than the capacitor, and higher power delivery than lithium-ion batteries (Figure 2.2a). In recent years, high surface area carbon materials, including activated carbons

(ACs), carbon nanotubes (CNTs), graphene, and porous carbon have been widely used as the electrode materials for EDLCs. Their capacitive behaviors are strongly dependent on the specific area (Figure 2.2b). It can be expressed as follows:

$$C = \frac{\varepsilon_r \varepsilon_0 A}{d}$$

where C (F) is the capacitance of EDLCs, ε_r is the electrolyte dielectric constant, ε_0 is vacuum permittivity (8.854×10^{-12} F m^{-1}), d is the effective thickness of the electrical double-layer, and A is the electrode surface area.[13,14]

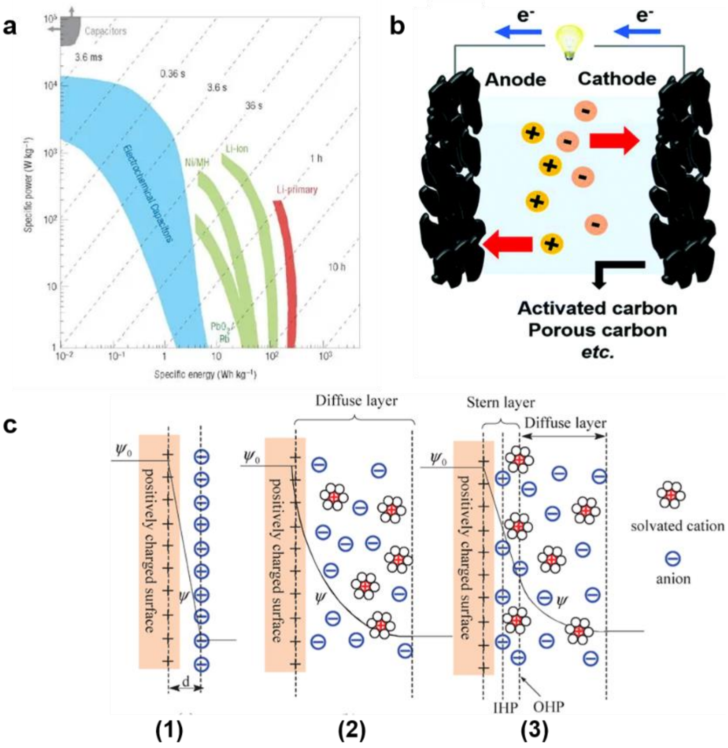

Figure 2.2. a) Ragone plot showing the performance comparison of different energy storage devices.[15] b) Schematic of an electric double-layer capacitor.[16] c) Models of the electric double-layer at a positively charged surface: (1) the Helmholtz model, (2) the Gouy-Chapman model, and (3) the Stern model.[17]

For the energy storage mechanism of EDLCs, Helmholtz firstly proposed a theory that describes the charge distribution at the interface of colloidal particles.[18] As shown in Figure 2.2c$_1$, this Helmholtz model states that two layers of opposite charge form at the electrode/electrolyte interface and are separated by electrolyte ions with an atomic distance “d”. Based on this model, Gouy and

Chapman[19,20] further proposed that a diffuse layer with electrolyte ions (cations and anions) exists on the electrode surface and the potential difference at electrode/electrolyte interface decreases exponentially due to the distribution of counter-ions (Figure 2.2c$_2$). Later, Stern proposed a model by combining the Helmholtz model with the Gouy–Chapman model together. This model explicitly describes that there are two regions on the electrode surface: diffuse layer and Stern layer (see Fig. 2.2c$_3$).[21] In the Stern layer, ions (very often hydrated) are strongly and compactly adsorbed by the electrode. The inner Helmholtz plane (IHP) and outer Helmholtz plane (OHP) are used to distinguish the two types of specifically adsorbed ions and non-specifically adsorbed counter-ions.

2.1.3. Pseudocapacitor

In contrast to the physical charge storage of EDLCs, the operation of pseudocapacitors involves a fast and reversible redox (faradaic) reaction at the electrolyte/electrode interface. Therefore, pseudocapacitors display higher specific capacitance and energy density than carbon materials of EDLCs. Simultaneously, they often suffer from lower power density and worse cycling lifetime. Generally, three types of faradaic mechanisms can be distinguished (Figure 2.3):[22] 1) underpotential deposition, 2) redox pseudocapacitance, 3) intercalation pseudocapacitance. Underpotential deposition occurs when metal ions (*e.g.* Au, Pt, Rh, and Ru) form an adsorbed monolayer at a different metal surface well above their redox potential. Redox pseudocapacitance occurs when ions in the electrolyte are electrochemically adsorbed on the surface or near-surface of electrode, accompanied by the charge transfer process. Various active materials with redox pseudocapacitance have been widely investigated, such as transition metal oxides (RuO_2,[23] MnO_2[24]) and conducting polymers (polyaniline (PANI),[25] polypyrrole[26], Poly(3,4-ethylenedioxythiophene) (PEDOT)[27]). For intercalation pseudo-capacitance, it occurs when ions intercalate into the tunnels or layers of an active material accompanied by a faradaic charge-transfer with no crystallographic phase change.[22] Currently, the most widely investigated electrode materials for intercalation pseudocapacitance are mainly nanostructured TiO_2, Nb_2O_5, V_2O_5 and MoO_3.[28–31]

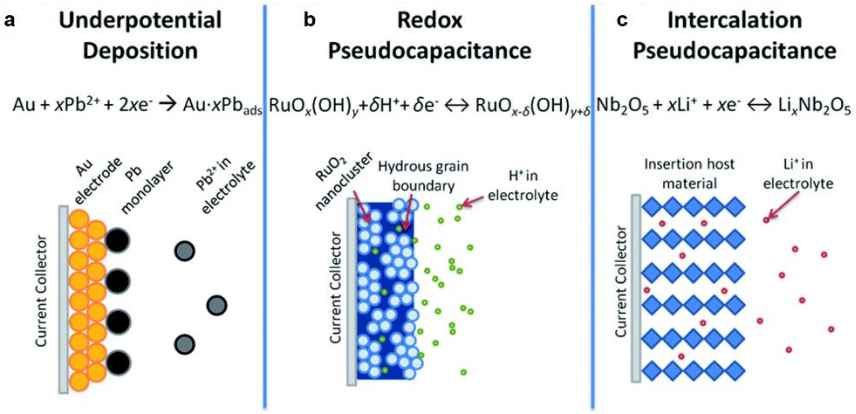

Figure 2.3. Different types of reversible redox mechanisms that give rise to pseudo-capacitance:[22] a) underpotential deposition, b) redox pseudocapacitance, and c) intercalation pseudocapacitance.

2.2. MSC configuration

As an electrochemical energy storage device, the basic structure of MSCs consists of a positive and a negative electrode separated by an ionic conductor electrolyte (Figure 2.4a). MSCs in the early stage adopted a “Sandwich” configuration in which two stacked electrode films are separated by solid electrolytes. This sandwich design often suffers from the short circuit and unacceptable position dislocation of the film electrodes. Another limitation lies in the difficulty in achieving precise control on the distance between the thick solid electrolyte layer and the electrodes, which can lead to an increased ion transport resistance and a great power wastage.[32]

In contrast, patterned in-plane interdigital electrodes can overcome the above-mentioned issues (Figure 2.4b). Two co-planar electrodes are physically separated on insulating substrates and the covered electrolyte on electrodes ensures the effective ion transport between electrodes. The thickness of electrode materials and the gap distance between electrodes can be achieved precise control in the microfabrication process. In practical applications, solid-state or gel-type electrolytes are preferred due to the requirement of leakage-free devices.[4]

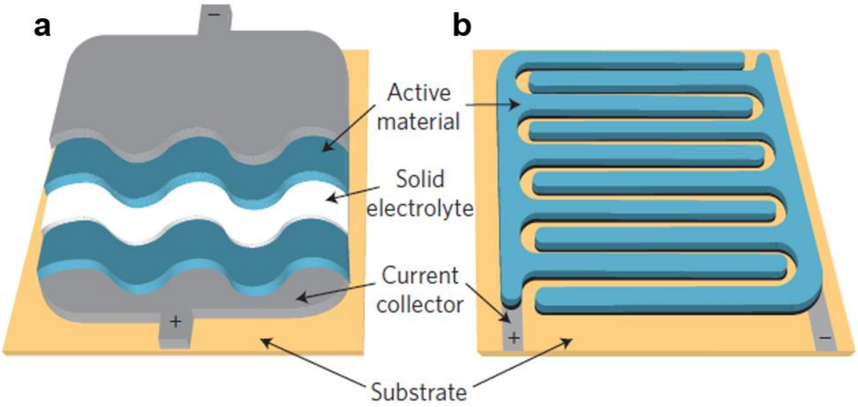

Figure 2.4. Schematics of the configurations of on-chip MSCs.[4]

Furthermore, fiber-based MSCs (FSCs) which use one-dimensional cylindrically shaped fibers as electrodes have also attracted significant interests. FSCs possess unique merits of being ultrathin, highly flexible, and convenient integration with wearable electronics and smart textiles. They also show great application potential as micro-scale devices in micro-electromechanical systems and miniaturized electronics. There are mainly three types of configurations: i) parallel fibers, ii) twisted fibers, and ii) coaxial fibers.[33–36] FSC electrodes can be fabricated using conductive fibers made from polymer, metal, carbon, piezoelectric materials, and conventional fibers which surfaces are modified with various functional materials.[37] Gel-type electrolyte is wrapped between electrodes. To realize large scale applications of the FSCs, various methods have been employed to synthesize fiber electrode, assemble FSCs, and integrate with other electronic components.

2.3. Fabrication strategies of interdigital MSCs

Photolithography, also known as ultraviolet (UV) lithography, is a mature technology utilized in MEMS and nanoelectromechanical systems (NEMS) because of its reliable fabrication process, high resolution and high yield of mass production. Normally, the photolithography by the cost-effective equipment can achieve a precision of sub-one micron.[38,39] In the microfabrication process of MSCs, photolithography is generally utilized to fabricate the current collector. However, this technology needs indispensable sacrificial templates in fabricating on-chip integrated devices.

In contrast, as a scalable and direct-writing technique, laser scribing has been applied to synthesis electrode materials with high-resolution patterns by using the heat effect of laser.[40–42] A typical application is to convert GO to reduced graphite oxide (rGO) by laser irradiation due to the photothermal effect. Researchers can directly pattern the GO surface into “rGO-GO-rGO” structures with micro-scale resolution.[43,44] Another application is to cut some other active material films to expected patterns, which is imperative in the fabrication procedure of MSC (Figure 2.5a). For instance, Kurra *et al.* fabricated a two-dimensional titanium carbide-based interdigital MSC on the paper with a scalable direct laser writing method.[45] However, laser scribing can only work for limited active materials, restricting the applications in the fabrication of on-chip MSCs based on diverse materials.

Inkjet printing is a familiar method of preparing interdigital electrode arrays via pushing droplets of liquid active materials on diverse substrates (Figure 2.5b). Because of the superiorities such as low cost, room-temperature operation, fast process, and scalability, inkjet printing has been extensively used in the fabrication of on-chip devices.[46–48] The solubility and chemical stability of the printing inks are the critical factors of determining the printing quality. In practical applications, excellent ink can generate droplets during the printing procedure without clogging the nozzle. Besides, some critical properties such as surface tension, viscosity, and the objective material particle size, are also important for the ink. In the future, the main challenge for this technique is the resolution of electrode patterns and the preparation of inks with active materials.

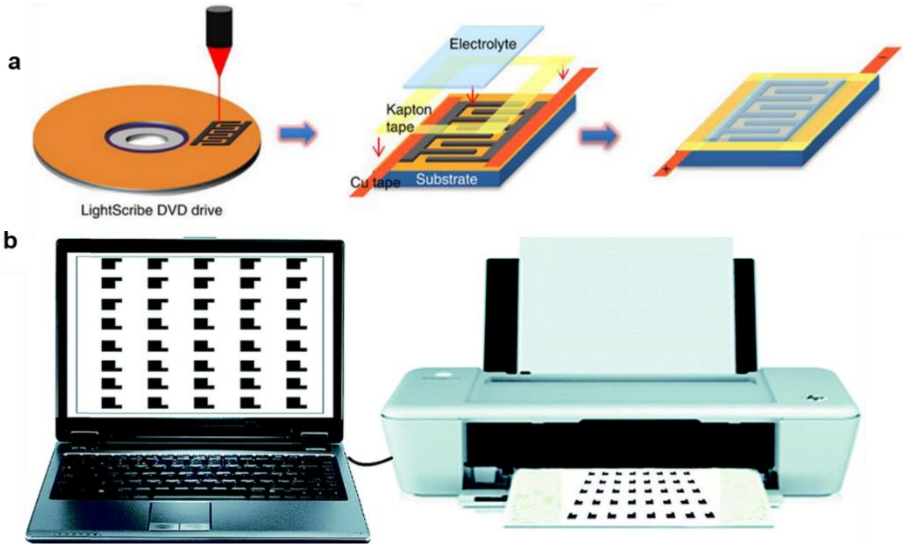

Figure 2.5. a) Schematic of the fabrication of rGO-based MSC via the writing laser.[49] b) The fabrication process for inkjet-printing: Design using a personal computer and inkjet-printing using a home printer.[50]

Screen printing is a mature printing technique applied to diverse substrates such as paper and cloth. A woven mesh is usually utilized during the printing procedure to support an ink-blocking stencil to prepare an expected image. The desired pattern can be obtained after the ink adheres and dries on diverse substrates.[51–53] As shown in Figure 2.6a, a facile strategy was demonstrated for fabricating high performance in-plane MSCs using screen printing and Electroless copper deposition (ECD). The interdigital current containing catalyst ink in ECD firstly formed copper. The last two ECD processes promoted the formation of $Cu(OH)_2$@FeOOH NTs.[54] The superiorities of screen printing strategy such as simple processes and not requiring expensive equipment, make it a potential method for the fabrication of electronic devices.

3D printing, also known as the additive-manufacturing technique, is a fast and low-cost technology for fabricating on-chip energy storage systems (Figure 2.6b). 3D printing has attracted much attention in fields of energy[55–58] and electronics.[59,60] It provides a powerful way to fabricate miniaturized MSC devices with various 3D structures, which is helpful to improve the power and energy density. Compared to conventional fabrication processes, 3D printing offers several advantages: 1) 3D printing demonstrates excellent process flexibility and geometry controllability; 2) 3D printing can well control the thickness of electrodes because of the layer by layer additive manufacturing nature; 3) The performance of 3D printed energy device typically outweighs their bulk counterparts; 4) 3D printing is a cost-effective and environment-friendly technology, which is attributed to the much-simplified process that enables one-step fabrication.

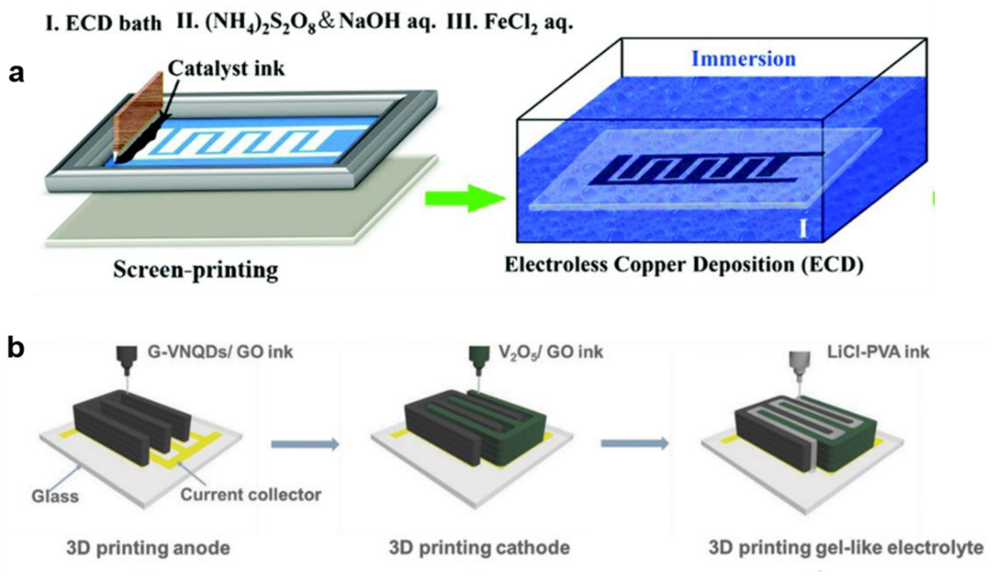

Figure 2.6. a) Schematic of the electrode fabrication by screen-printing method.[54] b) Schematic of a 3D-printed asymmetric MSC with interdigitated electrodes.[61]

2.4. Fabrication methods of active materials

For all MSCs with different configuration, *e.g.* sandwich-type MSCs, interdigital in-plane MSCs, and fiber-like MSCs, it is important to choose a reasonable fabrication method to synthesize the electrode materials, which not only exhibit excellent electrochemical performance but also match the post-fabrication process such as patterning and full device integration.

Physical vapor deposition (PVD) (*e.g.* thermal evaporation, sputtering) technique can deposit dense and uniform coatings on substrates, which is particularly beneficial for the synthesis of active materials, solid-state electrolytes, and protective shells. For example, Theresia *et al.* reported a symmetric sandwich-type MSC in which the sputtered lithium phosphorous oxynitride (LiPON) acted as the electrolyte and the sputtered cobalt oxide (Co_3O_4) acted as the electrode material (Figure 2.7b).[62] The configuration of this MSC is a stacked multilayer system consisting of $Cr/Co_3O_4/LiPON/Co_3O_4/Cr$, which was fabricated by a series of sputtering process on-chip. The deposition rate and the thickness of the film can be precisely controlled. Sputtering techniques usually produce films with no internal porosity, which is not desired for MSCs with high electrochemical performance. To solve this issue, Huang reported a scalable fabrication approach for preparing porous carbide-derived carbon (CDC) films and interdigital MSCs (Figure 2.7a).[63] TiC was deposited by utilizing the direct current magnetron sputtering technology under high temperature, and then TiC films transformed to porous CDC under partial chlorination without film delamination. The capacitance can reach up to 410 F cm^{-3}/200 mF cm^{-2} in aqueous electrolytes and 170 F cm^{-3}/85 mF cm^{-2} in organic electrolytes.

Spray coating of active materials on patterned electrodes is an affordable, easy-to-use and equipment-free physical method to covert as-prepared active materials onto objective substrates (Figure 2.7c). Currently, carbon nanomaterials (*e.g.* graphene and CNT), are the most frequently used materials in this method. Apart from this, spin-coating and film transfer are also common techniques to fabricate active material films in the MSC system. For example, Xiao *et al.* demonstrated an one-step mask-assisted simplified fabrication of high-energy MSC based on the interdigital electrode patterns (Figure 2.7d).[64] The phosphorene nanosheets/exfoliated graphene films with interdigital patterns were directly manufactured through step-by-step vacuum filtration and directly transferred onto a polyethylene terephthalate (PET) substrate. The patterned exfoliated graphene films exhibit good uniformity, mechanical flexibility, high conductivity (319 S cm^{-1}) and excellent structural integration, which can directly serve as binder- and additive-free flexible electrodes for MSCs.

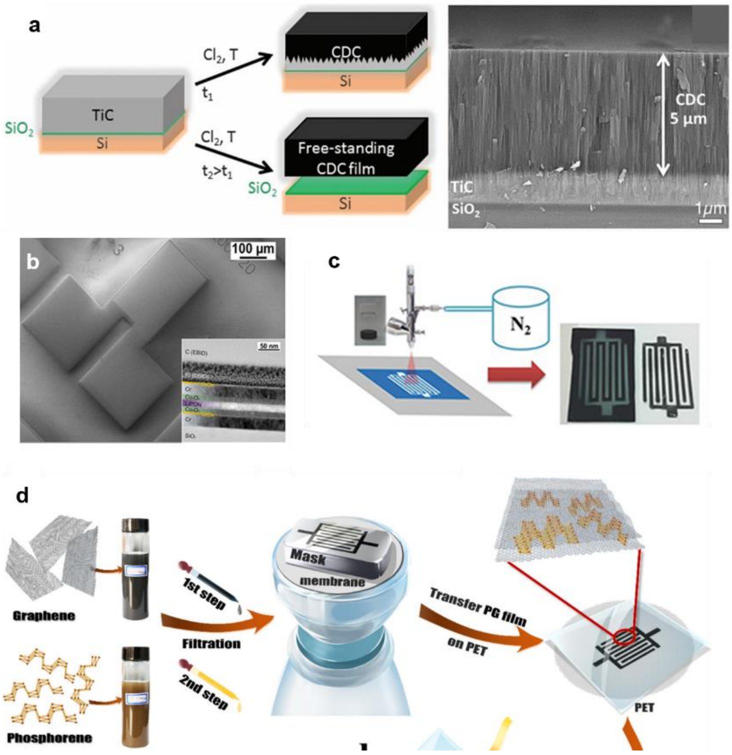

Figure 2.7. a) Preparation scheme of the chlorination process for sputtered TiC and SEM cross-section of SiO_2/TiC/CDC structure.[63] b) SEM image of overall sputtered MSC (The inset shows the cross-section imaged by Transmission electron microscopy (TEM)).[62] c) Schematic of the fabrication of single MSC devices by mask-assisted spray coating.[65] d) illustration of the fabrication of exfoliated graphene-MSCs, including the synthesis of graphene and phosphorene inks, step-by-step filtration of graphene and phosphorene, dry transfer of the hybrid film onto PET substrate.[64]

Chemical vapor deposition (CVD) is another very attractive deposition method for electrode materials, especially for the carbon materials (*e.g.* graphene and CNTs). With the atomic level of precise control, CVD technique can achieve a high quality of synthesis for the ultra-thin nanomembrane. For example, Lin and co-workers developed a simple CVD process for fabricating graphene-CNT based MSCs.[66] As a result, this MSC can deliver a high energy density of up to 2.42 m Wh cm^{-3}. Simultaneously, the superior rate capability of 400 V s^{-1} enables the micro-devices to exhibit a maximum power density of 115 W cm^{-3} in aqueous electrolytes.

2.5. Functionalization of supercapacitors

Along with the development of high-capacity materials and devices, it is intensively expected to integrate versatile materials with different properties into MSCs for enriching the functionalities. These smart MSCs can self-charge through integrating with solar cells and nanogenerators, and also are responsive to external stimuli, such as voltage, mechanical deformation, and temperature as well as light. Herein, recent studies on multifunctional devices are reviewed from the perspectives of device-level and material-level integration.

2.5.1. Tribo/piezoelectric driven self-charging function

Piezoelectric supercapacitor (PESC) is a novel self-powered device that can effectively store electrical energy by converting the mechanical energy from surroundings into a supercapacitor. Such an integrated system can meet the potential demands for miniature and wearable electronics. For instance, Ramadoss *et al.*[67] presented a piezoelectric-driven sandwich supercapacitor of which MnO_2 nanowires were employed as active materials and PVDF-ZnO film acted as a separator/piezoelectric layer (Figure 2.8a). The power supply of this piezoelectric unit relied on the flow of electrons in PVDF-ZnO materials which are driven by the externally compressive stress.[68] The result showed that it could achieve a potential change from 35 to 145 mV (110 mV charged) in 300 s.

Besides, the triboelectric nanogenerator (TENG) has been another attractive self-powered mechanical harvester to be integrated with a supercapacitor. The working of TENG relies on the conjunction of contact electrification and electrostatic induction.[69,70] It possesses advantages of unprecedented output performance, low cost in fabrication as well as excellent robustness, and it can efficiently harvest mechanical energy from the living environment.[71–74] Song *et al.* created a sandwich-shaped TESC in which supercapacitor was designed between the wrinkle polydimethylsiloxane (PDMS) films with fluorocarbon plasma treatment (Figure 2.8b).[75] During ambient vibrations, the middle supercapacitor can be charged up to 900 mV in 3 h with a compressive stress of 8 Hz.

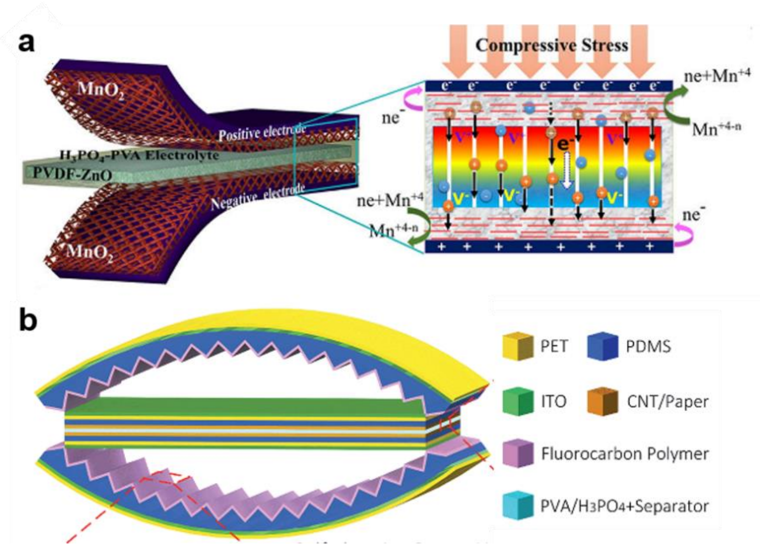

Figure 2.8. a) Scheme of the structure and mechanism of a sandwich SCSPC using MnO_2 electrodes and a PVDF-ZnO layer as a separator/piezoelectric layer.[67] b) Scheme of the sandwich TESC.[75]

Nevertheless, the energy conversion efficiency of TENG may still suffer from the energy loss in the sliding process (heat dissipation and the normal force on contact surfaces). In this regard, some researchers proposed a triboelectric-pyroelectric-piezoelectric hybrid system to charge SCs, resulting in an increased energy harvesting efficiency of 26.2% and charging rate about twice higher than that of TENG.[76] With higher integration and functionalization, Wang's group further demonstrated a self-powered system by integrating hybrid TENG/PENG and solid-state electrochromic MSCs array.[77]

2.5.2. Solar cell driven self-charging function

Photo-rechargeable supercapacitor (PRSC) is a self-charged energy storage device which mainly relies on the power supply from the solar cell. Under sunlight illumination, this green energy can be converted effortlessly to electricity and further stored in supercapacitors in a small space.[78–85] With the demand for miniaturization, convenience and lightweight of PRSC in practical applications, the high integration of PRSC with excellent performance has been intensively expected.

In the early stage, researchers mainly focused on the study of fiber-shaped PRSC which could have the potential application in the wearable and stretchable field. For instance, an integrated twisted wire-shaped PRSC was developed through fabricating aligned CNT and TiO_2 tubes on titanium wire.[86] The overall energy conversion efficiency was increased to 1.5%. However, the instability in bending and the liquid electrolytes in solar cells were the negative factors influencing the practical application. To solve this issue, a coaxial all-solid-state “energy fiber” consisting of a dye-sensitized solar cell (DSSC) and a CNT/TiO_2-based SC was reported (Figure 2.9a).[87] The overall conversion efficiency can achieve as high as 2.73%, while the energy storage efficiency can reach up to 75.7%.

Apart from the fiber-shaped device, a stacked planar all-solid-state PRSC was developed by integrating organic photovoltaics with supercapacitors.[88] The organic photovoltaics exhibited a photoelectric conversion efficiency of 3.39%. Later on, the highly integrated PRSC was improved in a configuration that the solar cell and supercapacitor shared one electrode. For instance, a type of porous silicon as a shared electrode connected the DSSC and porous silicon-based supercapacitor by a simple wafer-scale process.[89] An overall conversion efficiency of 2.1% was achieved. The designed supercapacitor which can discharge at high frequency has the potential to overcome performance fluctuations during solar energy harvesting. This highly integrated design reduced the size of the whole device and the energy loss in external connections. Base on this strategy, a wearable energy-smart ribbon PRSC was reported by integrating the perovskite solar cell and a symmetric supercapacitor (Figure 2.9b).[90]

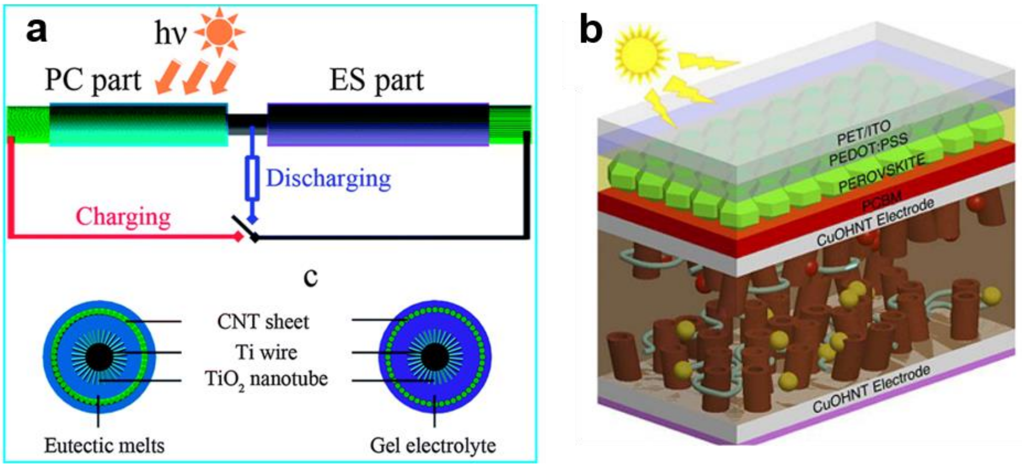

Figure 2.9. a) Schematic of the structure of the coaxial PRSC with the integration of DSSC and supercapacitor.[87] b) Schematic of PRSC ribbons with a shared copper electrode.[90]

2.5.3. Electrochromic function

Due to the electrochemical reduction/oxidation process, some active materials in energy storage devices have shown the ability to reversibly change their colors.[91–103] This electrochromic (EC) feature can be integrated with supercapacitors to monitor the real-time charge/discharge working states by simple visual inspection while allowing reliable energy storage. Besides, this electrochromic energy storage device has also potential applications in smart systems such as variable-transmittance windows and miniature indicators.[104,105]

Normally, some material candidates like metal oxides or conductive polymers can be employed as the EC supercapacitor electrodes because of the pseudocapacitive property. As an example, NiO uniform film is capable of changing color from the transparent (bleached state) to brown (Ni^{2+} of NiO was oxidized to Ni^{3+} of NiOOH).[106] An optical modulation of 63.6% and a high coloration efficiency of 42.8 $cm^2\ C^{-1}$ at 550 nm can be achieved. Zhang *et al.* presented the first stimulus-responsive MSCs by employing exfoliated graphene/V_2O_5 nanoribbons as electrode materials and methyl viologen as EC materials.[107] When a voltage was applied from 0 to 1 V, the methyl viologen in electrolyte enabled the device a remarkable reversible electrochromic effect (Figure 2.10a).

Among conducting polymers, PANI exhibited obvious color changes during its redox reactions. In Chen’s report,[96] PANI/CNT composites as two symmetric electrodes were wounded on an elastic fiber. The device showed the fast and reversible color change between blue, green, and light yellow under a corresponding voltage of 1, 0.5 and 0 V (Figure 2.10b). The asymmetric design can simultaneously increase the potential window and coloration range. Therefore, an asymmetric EC supercapacitor was further designed to achieve a wide potential window of 1.4 V, accompanying the color change from light green (bleached state) to dark blue.[95]

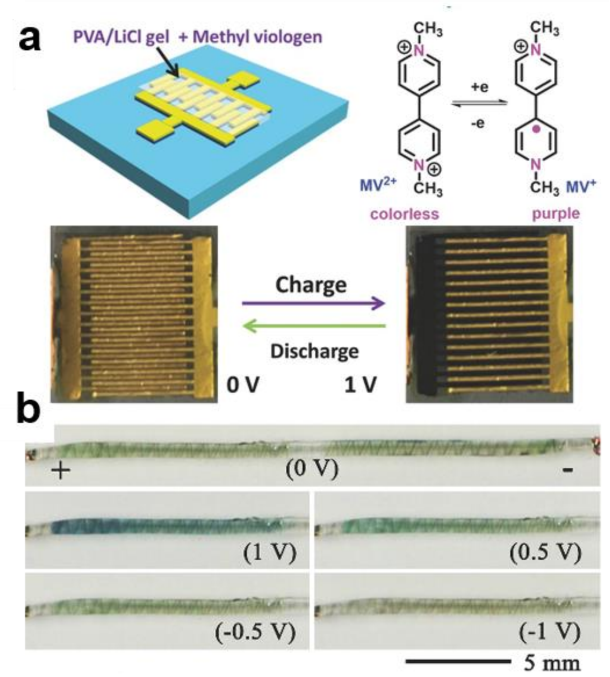

Figure 2.10. a) Scheme of the fabrication of stimulus-responsive MSCs, the electrochromic mechanism of methyl viologen, and photographs of the reversible EC behavior.[107] b) Photographs of the color change process for the PNAI/CNT based fiber-shaped electrochromic supercapacitors.[96]

2.5.4. Self-healing function

With the exploration of MSCs in wearable and portable electronics, MSCs may undergo external mechanical damage caused by deformation or fracture.[108] The undesirable wound in supercapacitors would result in a performance degradation and even breakdown of operation in electric circuits. To date, a key solution is to develop multifunctional supercapacitors through integrating with healing materials.

Wang *et al.*[109] reported the first self-healing supercapacitor by spreading functionalized SWCNT films on supramolecular network/TiO_2-based substrates. The self-healing of substrates and SWCNT films relies on the re-contact and reconnection between damaged sections by hydrogen bonds, hence enabling the functional and structural restoration of the device. To further improve the healing efficiency, cyclability as well as stretchability, Huang *et al.*[110] developed a polyacrylic acid (PAA)-based self-healing electrolyte crosslinked by hydrogen bonds and vinyl hybrid silica nanoparticles. This polyelectrolyte could be easily stretched over 3,700% strain. As an example, a supercapacitor consisting of this polyelectrolyte and PPy/CNT active materials could be simply self-healed during all 20 breaking/healing cycles by reconnecting the damaged interfaces (Figure 2.11a). Besides, carboxylated polyurethane (PU) as another self-healable electrolyte was designed into an interdigital 3D MSC to fabricate aerogel electrodes composed of MXenes and rGO (Figure 2.11b).[111] After the fifth cutting, this MSC maintained high electrochemical performance and specific capacitance retention up to 81.7%.

For fiber-shape supercapacitor, Huang *et al.*[112] studied the self-healability of assisted yarn-based supercapacitor by wrapping magnetic electrodes into a PU shell (Figure 2.11c). The magnetic force can promote the correct alignment of damaged electrodes, thereby enabling the reconnection and the restoration of device. The resulting specific capacitance can maintain 71.8% after the fifth healing.

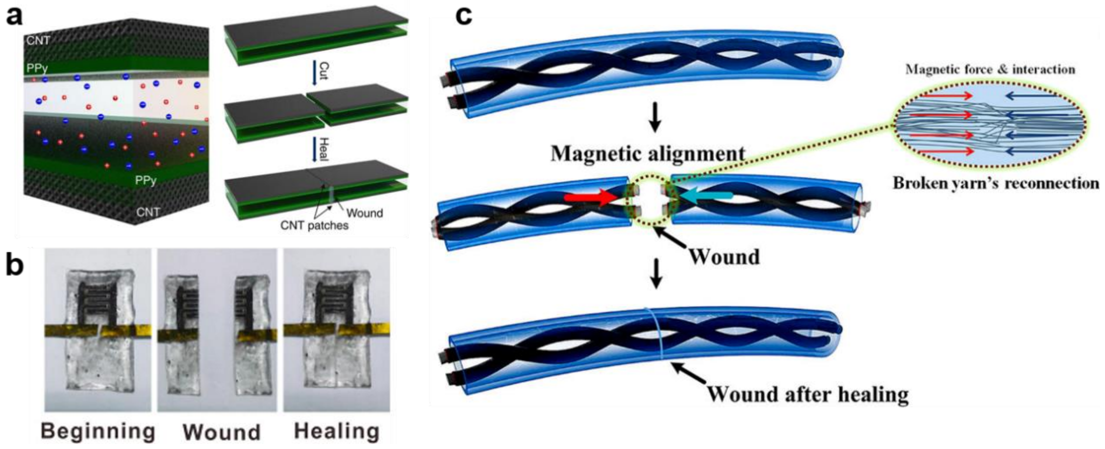

Figure 2.11. a) Schematic of fabrication strategies for self-healable and stretchable supercapacitor with dual crosslinked PAA electrolyte.[110] b) Schematic and photographs of the 3D self-healing MSC.[111] c) Schematic of the yarn-shape fibrous supercapacitor's self-healing process assisted by the magnetic alignment.[112]

2.5.5. Sensing function

Portable and wearable sensors have attracted considerable attention due to their potential in monitoring personal health and the environment. The current trend for those miniaturized sensing systems is to integrate with MSCs, which can avoid the external power supply and thus decrease the overall volume as well as weight. For this motivation, numerous studies on sensor/MSCs self-powered systems including photodetectors, gas sensors, and strain sensors have been reported.[113–117] For instance, Kim *et al.* reported on the fabrication of flexible MSC arrays with hybrid electrodes of MWCNT/V_2O_5 nanowire composites, which powered the SnO_2 NW UV sensor on the same substrate.[114] The discharge rate dramatically increased with UV due to the improved photocurrent through the SnO_2 NW sensor. Chen *et al.*[118] even simply fabricated photosensitive TiO_2 nanoparticles on one electrode of sandwich-type MSCs to prepare bifunctional integrated devices. The result showed that those devices not only almost remained the intrinsic capacitance behavior but also showed an excellent sensitivity of detecting white light. Gas sensor is another common example of the integration with MSCs. Yun *et al.* developed a stretchable NO_2 gas sensor driven by MSC array on planar Ecoflex substrate with minimized strain.[119] This NO_2 gas sensor can also be designed into a wire-type configuration, providing great potential application in self-powered sensing systems consisting of electronic textiles.[120] Besides photodetectors and gas sensors, Song *et al.* studied the integration of the piezoresistance sensor with MSCs, in which the interdigital MSCs were fabricated on top of the porous CNT-PDMS elastomer.[121] The entire device exhibited reliable electrochemical performance and cycling stability.

2.5.6. Stretchable function

Stretchable electronics is an emerging research area. The stretchable devices are required to have the capacity of accommodating large levels of strain and simultaneously maintaining their performance under mechanical deformation. To date, great efforts have been made in developing stretchable MSCs, including one dimensional (1D) linear and planar type configurations. For 1D MSCs, in the early stage, Peng’s group studied stretchable aligned CNT sheets which were wrapped on an elastic fiber.[122] The fabricated CNT sheets exhibited remarkable performances such as flexibility, tensile strength, electrical conductivity, mechanical as well as thermal stability. An excellent specific capacitance of approximately 18 F g^{-1} was achieved after 100 cycles of stretching by 75%. Besides, spring-like CNT fibers prepared by twisting several CNT fibers together can be easily stretched and released up to 100%.[123]

For planar configuration, wavy-like electrodes with pre-stretched substrates or electrolytes have been proven to be an effective strategy to realize stretchable MSCs. For instance, Qi *et al.* rationally designed suspended wavy graphene microribbons on tripod-structured PDMS substrates.[124] The performances of MSCs were well maintained at 100% of stretching, even after 5000 cycles of stretching and release.

2.5.7. Thermo-responsive function

In practical electronics, frequent operation of energy storage devices may lead to mass heat generation and decrease of device lifespan.[125–128] To efficiently address these issues which are critical for practical safety and usage, thermosensitive electrolytes have been applied in supercapacitors due to their capability of sensing surrounding thermal risk and reversibly controlling the operation of supercapacitors. For instance, a thermo-responsive polymer p(N-isopropylacrylamide-co-2-acrylamido-2-methyl propane sulfonic acid) has been successfully used as electrolyte, and demonstrated as the function of protective switches in supercapacitors.[129] This polymer electrolyte served as ion channels for electrode materials, facilitated/inhibited the ion transport in the on/off state between 20 ^{o}C and 40 ^{o}C. Later on, a novel copolymer poly(N-isopropylacrylamide-co-acrylamide) was prepared using free radical polymerization.[130] Due to the sol-gel transition at high temperature, this functional electrolyte can inhibit the ion transport between two electrodes and further provide thermal protection for the device. Another type of thermo-sensitive electrolyte, poly(ethylene oxide)-block-poly(propylene oxide)-block-poly(ethylene oxide), was used for realizing self-protection of supercapacitors.[131] With the temperature increased, this electrolyte transformed into a gel state, which would inhibit the motion of ions and shut down the supercapacitor device. The gelation of Pluronic solution-based electrolytes significantly inhibited the migration of ions, leading to a nearly 100% decrease in specific capacitance.

Besides, another type of thermo-sensitive electrolyte, poly(ethylene oxide)-block-poly(propylene oxide)-block-poly(ethylene oxide), was used for realizing self-protection of supercapacitors.[131] With the temperature increased, this electrolyte transformed to a gel state, which would inhibit the motion of ions and shut down the supercapacitor device. The gelation of Pluronic solution-based electrolytes significantly inhibited the migration of ions, leading to a nearly 100% decrease in specific capacitance. The transition temperature and the degree of capacity loss would be readily tuned over a wide range by optimizing the solution concentration and molecular weight of the polymeric materials.

2.5.8. Photo-switchable function

Recently, Liu *et al.* reported a photo-switchable MSC for the first time. A thin layer of photochromic diarylethene derivatives (DAEs) was coated on the surface of interdigital graphene electrodes to form the MSCs (Figure 2.12).[132] The fabricated MSCs were linearly responsive to the stimulation of UV light and visible light irradiation. The areal capacitance showed a reversible modulation of up to 20%. It was proposed that this functional switch for real-time monitoring is related to the charge transfer at the DAE-graphene interface. Besides, the MSC device can be operated at an ultrahigh rate of 10^4 V s^{-1}, which is four times higher than those of conventional supercapacitors and twice higher than those of other graphene-based MSCs.

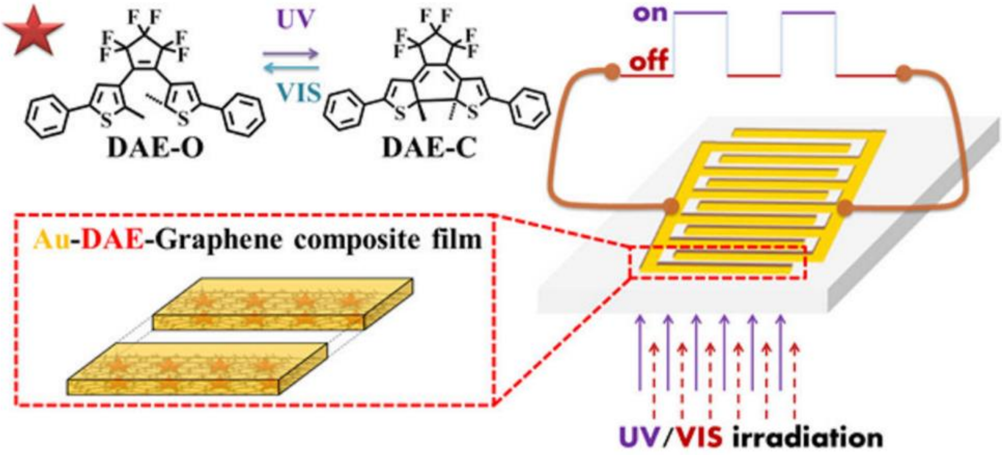

Figure 2.12. Schematic illustration of photo-responsive MSC device with DAEs on the top of graphene electrodes.[132]

2.6. Conclusion and outlook

The recent research advances of MSCs in the fabrication technologies, strategies, as well as their integration with functional devices and materials, are summarized. The miniaturization of electronics has triggered numerous studies on the microfabrication of MSCs. These methods exhibit their advantages and limitations. For example, although multiple processing steps and the requirement on the ultraclean working environment make the photolithography technology time-consuming and complicated, photolithography can provide high resolution and precision for mass micro/nanofabrication of MSCs. Ink-jet printing and screen printing technology are much simple and highly efficient, because they can accomplish the patterning and the deposition in the same step. It means this method does not involve a complicated lithography process, toxic chemical treatments, or expensive rigid template, thus reducing the complexity and material usage in the process. Furthermore, it has good control in the printing precision through computer programs by propelling droplets of ink onto paper, plastic, or other substrates on demand. Therefore, inkjet printing and screen printing are expected to be both beneficial and applicable to fabricate MSCs. Similarly, 3D printing is also expected to be a prospective technology for the production of on-chip MSCs. However, one critical disadvantage of these prevalent printing techniques is that the precision is not as high as photolithography. This restricts their application in creating ultra-compact MSCs and integrated micro-autonomous systems.

Demanded by next-generation microelectronics, the integration of MSCs with more functions has aroused great interests in recent years. From the perspective of device-level integration, renewable energy harvesters like nanogenerators and solar cells have been integrated with miniaturized supercapacitors, making them promising candidates in self-powered systems. Advanced materials and novel designs were employed to improve the performances of integrated devices (*e.g.* total conversion efficiency). In particular, the design for shared electrodes in those devices have reduced the usage of external electric circuit connections and decreased the size/weight of the whole system. From the perspective of material-level integration, electrochromic, self-healing, and photo-switching functional materials have been explored and utilized to integrate with electrodes and electrolytes in MSCs. Those multifunctional MSCs exhibited a fast response to the external stimuli. In the latest research, some novel functional materials have been employed to fabricate MSCs towards a direction of intelligence.[27,77,78,132,133]

Despite the aforementioned encouraging progress, the development of the new generation of MSCs is still at its early stage. More efforts should be taken toward future practical applications:

(1) For pursuing high energy density, the high load of active electrode materials per footprint area should be taken into consideration for improving MSCs. One strategy is to construct deep cavities on substrates by etching. Nevertheless, the active materials may be only deposited on the surface of the cavities, limiting the further improvement in performance. Therefore, another strategy is to fill the active materials in 3D electrodes with high load, while ensuring the smooth transport of electrolyte ions inside. Currently, the development trend towards 3D MSCs is to construct the porous structure, for instance, porous graphene/MnO_2 via laser-scribing,[134] porous gold/RuO_2[23] and carbide-derived carbons[63] via an etching process. For other technologies, the convenient 3D printing should be a prospective technology for fabricating the 3D structures.[135] The height of electrodes or the load of active materials can be controlled from hundreds of nanometres to millimetres on target substrates. Besides, the direct printing of asymmetric is still challenging for conventional technologies. Furthermore, in recent years, rolled-up nanotechnology has emerged as a unique method to self-assemble thin-films into 3D tubular structures by using strain engineering.[8,136–140] By this approach, the active materials in supercapacitors can be wrapped inside this configuration with a decreased footprint area. As a future concept, this microfabrication technology would be a great choice for developing 3D MSCs with high performance while maintaining a small footprint.

(2) For the functional self-powered system, most of the above-mentioned integrated energy harvesters and MSCs are still at the stage of proof-of-concept. The performance, especially total energy conversion efficiency of them should be further improved through optimizing the design of overall structures and the match degree between energy conversion and energy storage. For miniaturized and intelligent microelectronics, it would be a very critical and challenging topic to pursue higher integration and smaller device volume for those integrated MSCs.

(3) Synthesizing various functional materials into a single electrode component of MSC would be a hopeful direction to accommodate with different specific requirements with a limited footprint. On the other hand, the integration of functional devices (*e.g.* solar cells and photodetectors) with MSCs is still at a primary level. Currently, the joint between these devices is merely based on wire connection in external circuits. Therefore, it will be essential to improve the MSCs integration and smartness level by combining advanced micro-/nanofabrication methods with the integrated circuit design.

This chapter is based on the publication of *Small Methods,* **2019**, 8, 1800367, titled "*Recent Progress in Micro-Supercapacitor Design, Integration, and Functionalization*".

Chapter 3. Overview of rolled-up technology

Over the past few decades, 3D micro/nanostructures with various shapes, architectures, and materials have been developed for the application in microelectronic systems, because their dimensionality can endow micro-devices new functionalities and higher integration densities as compared to 2D micro/nanostructures.[141,142] Rolled-up nanotechnology is an unique approach to self-assemble 2D nanomembranes (*e.g.*, metals, semiconductors, oxides, molecules, and polymers) into 3D structures by using strain engineering. This self-assembly process smartly combines top-down and bottom-up methods to pattern functional nanomaterials into ordered 3D micro- and nanostructure arrays. One promising advantage of this approach is that such a self-assembled structure can endow micro-devices (*e.g.* supercapacitor) with functionality and high performance under a limited footprint area. In this chapter, the 3D self-assembly of the inorganic and polymeric film as a strain layer will be fundamentally discussed.

3.1. 3D self-assembly of the inorganic nanomembrane

3.1.1. Introduction

More than 100 years ago, Stoney reported the study on the tension of metallic films deposited by Electrolysis.[143] Based on this type of phenomenon, the rolled-up nanotechnology was introduced by Prinz in 2000 and then by Schmidt as well as Eberl in 2001 in journal *Nature*.[136] To date, this technique has proven to be an intriguing approach for extensive promising applications in the growing interdisciplinary field of the micro- and nanosciences. The principle of this technique involves the release of an inorganic nanomembrane with an internal strain gradient on the substrate after selectively etching a sacrificial layer, as shown in Figure 3.1. Such nanomembrane consists of a bilayer of two materials with material1 and material 2, which are subject to two different biaxial strain ε_1 and ε_2, respectively. When the strain gradient $\Delta\varepsilon$ (ε_1-ε_2) across the bilayer is sufficiently large ($\Delta\varepsilon > 0.5\%$), the nanomembrane could roll-up. In the case of a small vertical strain gradient, the nanomembrane may corrugate and form into wrinkles instead.[144]

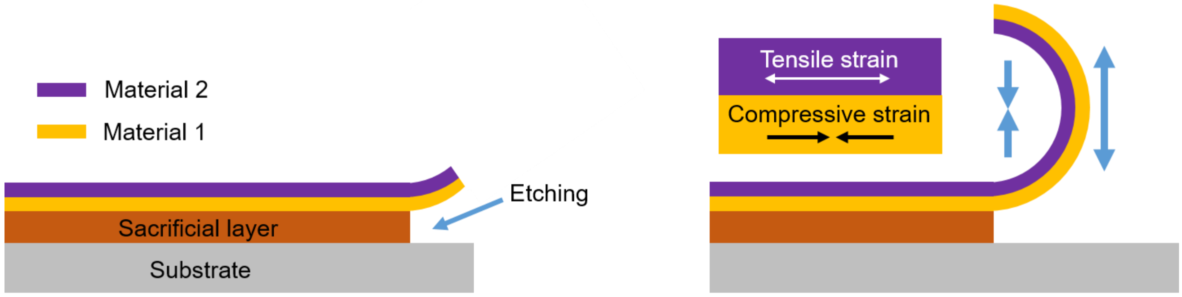

Figure 3.1. A scheme showing the method to create the tubular structure by rolled-up technology.

Theoretical investigations reveal that the diameter of the created tubes is mainly determined by the thickness and the intrinsic properties of the materials.[144] By using the above-mentioned simplified bilayer model, the radius of the tubular structure can be written as the following formula:

$$\mathrm{R}_0 = \frac{(d_1 + d_2)^3}{6(1 + v)d_1 d_2 \Delta\varepsilon}$$

where d_1 and d_2 are the thickness of material 1 and material 2, and v is the Poisson ratio between the two materials.

3.1.2. Rolled-up nanomembranes for capacitors

In the case of miniaturized energy autonomous systems (MEAS) containing microelectronic devices, energy harvesters and energy-storage elements (*e.g.*, wireless sensor networks and medical device implants), the reduction of the entire system must be addressed.[145] Rolled-up nanotechnology of nanomembranes offers a feasible route towards reducing the footprint of microcomponents in MEAS as well as the incorporation of appealing physical and electrochemical properties. For the above-mentioned capacitor, Bufon *et al.* successfully fabricated self-wound ultracompact capacitors (UCCaps) by this technique.[138] As shown in Figure 3.2, the process starts with the fabrication of a planar strained multilayer nanomembrane by the sequential deposition of metal and dielectric thin films on top of Ge/GeO_x sacrificial layer. In this approach, the corresponding planar devices are fabricated on pre-strained hybrid nanomembranes by the standard photolithography technique. The optimization of the intrinsic mechanical strain in the device's layers allows the autonomously rolling of the planar structure once it is released from the host substrate. Interestingly, in addition to reducing the device footprint by the rolling process, the bottom metallic plate mechanically touches the top oxide layer so that the final active capacitor area increases. The rolling of the tubular nanomembrane capacitor shown in Figure 3.2 results in the reduction of the footprint to about 0.002 mm^2, representing a compactification of 25 times compared to the original unrolled size (0.050 mm^2). It can also be engineered in a variety of configurations to increase the capacitance. For instance, Sharma *et al.* tailored the electrical properties by combining different high-*k* dielectrics such as Al_2O_3, TiO_2, and HfO_2.[137] Self-rolled double-tube capacitors electrically connected in parallel were successfully fabricated. They also demonstrated that 1600 of double-tube UCCap array could be fabricated on a 4-inch wafer.

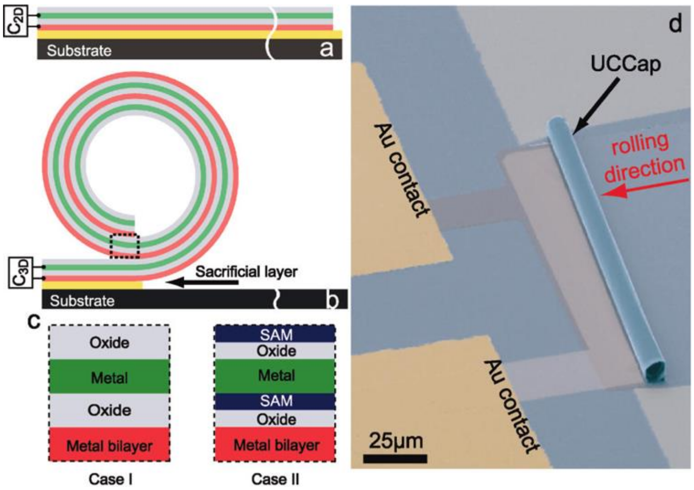

Figure 3.2. a,b) Planar capacitor and rolled-up capacitor after removing sacrificial layer. c) Layer sequence for inorganic and hybrid organic/inorganic capacitors. d) Typical SEM image of UCCaps.[138]

From the above researches for the tubular capacitor, we know that the sacrificial layer is generally the first step to be fabricated for rolled-up devices. This requires that the sacrificial layer is not only chemically stable in the subsequent fabrication process, but also can be removed in the etching solution which has no negative effect on nanomembranes. To date, Ge/GeO$_x$ layer has been proved to be a successful sacrificial layer that can be etched away in water. However, the slow etching rate of Ge/GeO$_x$ increases the rolling time of devices, thus enlarging the risk of intrinsic strain release in nanomembranes. This tiny fluctuations in the formation process can lead to large deviations in the final shape and structure of each device. Especially, when rolling high length-to-width aspect ratio nanomembranes, reliable and reproducible self-assembly of such nanomembranes has become an increasingly challenging task.[146] As an alternative strategy, Gabler *et al.* developed a novel approach for the self-assembly of 3D nanomembrane architectures by the assist of magnetic fields. The methylcellulose (MC) as sacrificial layer has high solubility in water, leading to the fast rolling of the large length scale nanomembrane in seconds and the enhanced overall assembly yield to values >90%. Besides, misassembly issues occurring during the mechanical transformation of planar nanomembranes into 3D "Swiss-roll" architecture have been carefully addressed by simulating and experimental testing of their assembly behavior in external static and dynamic magnetic fields of two orientations.

3.1.2. Rolled-up nanomembranes for Li-ion batteries

Over the last decade, alloys (*e.g.* Si, Ge, Sn) and transition metal oxides (*e.g.* Fe_2O_3, MnO_2, NiO) have been vastly explored as electrode materials for the next generation of Li-ion batteries (LIBs).[8] However, these materials generally suffer from poor charge transfer kinetics and large volume changes during charge/discharge reactions, which easily leads to electrode degradation and limited cycle life, thus impeding practical applications of LIBs in advanced consumer electronics and electric transport systems. To solve these issues, rolled-up nanotechnology provides an intelligent way to release the strain caused by lithiation or delithiation as well as provide extra interior space for electron and ion transport, thus improving the electrochemical performance of the LIBs.

Tubular nanomaterials used in LIBs can be prepared by photolithography and physical deposition techniques. Utilizing conventional photolithography, the nanomembranes can be correctly patterned on a photoresist sacrificial layer during deposition, which provides the obvious convenience of the accurate positioning of microtubes and module integration on a single chip.[145] Such a simplified process facilitates practical applications and mechanistic investigations at the microscale level. It is worth noting that the deposition rate, base pressure, and the nanomembrane thickness need to be taken into account during nanomembrane deposition. Various diameters can be obtained by changing the thickness and the strain gradient of nanomembranes. As shown in Figure 3.3a, the first attempt at studying tubular electrode materials for LIBs was made by Ji *et al.*[147] In their work, a self-wound 3D bilayer RuO_2/C tubular structure was fabricated by sputtering nanoscale RuO_2/C layers on a photoresist sacrificial layer. The strained composite nanomembranes can be quickly rolled-up and free-standing through dissolving the sacrificial layer in acetone. The composite including RuO_2/C microtubes, PVDF binder as well as carbon black was then used for the anode materials of LIBs. The electrochemical measurement showed that such RuO_2/C tubular nanomembranes exhibits a discharge capacity of 830 mAh g^{-1} with a Coulombic efficiency of 99%, implying enhanced lifetime and good reversibility of the hybrid tubes enhanced cycling stability. The improved electrochemical properties can be ascribed to the tubular nanomembrane structure, allowing for strain-relaxation, along with the stable supporting carbon layer, which maintains the electrode integrity during the conversion reaction of the active layer. Afterward, various kinds of tubular nanomembranes (C/Si/C, SiO_x/SiO_y, Si/graphene, GeO_2/graphene, Ge/Ti, NiO, SnO_2/Cu, Pd/MnO_x/Pd, TiO_2) with different architectures using rolled-up nanotechnology were explored for their potential applications as high-performance electrodes for LIBs.[148–156]

Despite appealing mechanical and electrical properties of tubular electrode materials, a deeper understanding of the relationship between the tubular structure, electrical/ionic conductivity, the electrochemical kinetics as well as the lithium storage performance still needs to be explored. Therefore, Si *et al.* presented a lab-on-chip electrochemical device platform to probe the electrochemical kinetics, electrical properties, and lithium-driven structural changes.[157] Figure 3.3b shows a schematic of a micro-LIB based on a single Si tubular nanomembrane. A single Si tube and a strip of lithium foil were used as the working electrode and counter electrode, respectively, and a PDMS chamber served as the electrolytic cell. Figure 3.3c reveals an optical microscopy image of the single rolled-up Si tubular nanomembrane with a diameter of around 30 μm, and three Ti contacts were made with one in the middle of the tube and two at its two ends. Cyclic voltammetry (CV) curves of the Si tube exhibit sharp, better-resolved peaks compared to that of a planar Si film due to the enhanced diffusion effect in the unique tubular structure, which makes the rolled-up tube a promising candidate for an ultramicroelectrode for electrochemical studies. A maximum electrical conductivity occurs after the lithiation of the Si tube. After three cycles, the tube exhibits a highly wrinkled structure due to the strain-induced local deformation, which could be exploited to maintain a stable charge/discharge cycling.

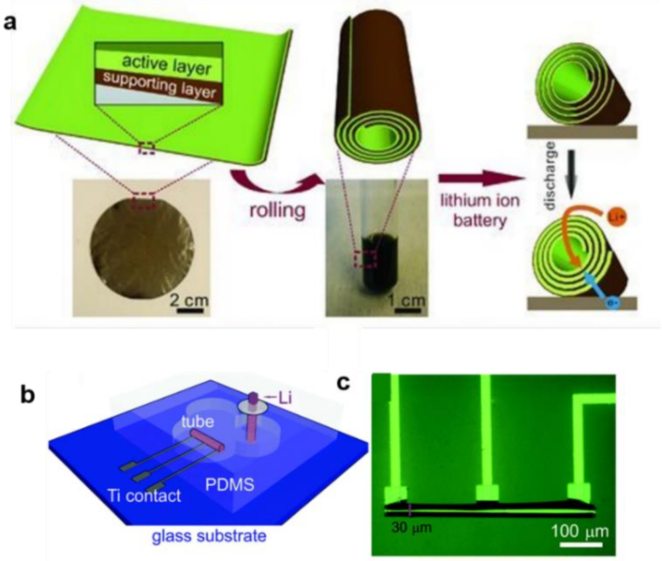

Figure 3.3. a) Schematic illustration of the process for rolled-up RuO_2/C bilayer microtubes.[147] b) Schematic illustration of an encapsulated LIB with a single Si microtube as the anode.[157] c) Optical microscopy image of a single rolled-up silicon tube.[157]

3.2. 3D self-assembly of the polymeric layers

3.2.1. Introduction

As introduced from the last section, we know that inorganic nanomembranes could be directly deposited onto the sacrificial layer using the conventional physical deposition method. Though removing the sacrificial layer in an etching solution, they can be self-assembled into tubular materials/devices with the release of intrinsic strain. The optimized thickness of inorganic nanomembranes (*e.g.* Cr/Ti) for rolling should be lower than 100 nm, owing to their brittleness. This extremely low thickness implies that they are not suitable for the self-assembly of thicker film. Therefore, it is essential to develop a novel rolled-up technology which can self-assemble micro-thickness film into tubular devices, thus opening up the possibility of creating novel 3D microelectronic devices.

Nature is inspiring researchers to conceive enormous ideas for the design of intelligent materials with superior properties. Self-assembled stimuli-responsive polymer films are examples of biomimetic materials. Such films can mimic movement mechanisms of plants (*e.g.* pine-cone) and form self-assembled complex 3D structures. Hydrogels, for instance, are of particular interest to design self-assembled 3D functional microstructures due to their high water content, permittivity, and mechanical properties which resemble those of non-osseous living tissues. Generally, homogeneous swelling/deswelling for single hydrogel only affects the size of an object and the self-assembly of the shape requires the incorporation of proper reinforcement material.

In recent five years, a novel platform based on a new type of hydrogel, polyimide (PI), and sacrificial layer has been studied to construct 3D tubular micro-devices.[139,140,158,159] These polymers are highly stable to tolerate multiple lithography steps and various processes with harsh chemical and vacuum treatments.[160] In addition, key issues of adhesion between layers and compatibility with microfabrication processes have been addressed. As shown in Figure 3.4, the crosslinked hydrogel layer can swell and release volumetric stress as carboxyl groups uptake a large amount of etching solution. PI as a reinforcement layer is inert to the external stimuli due to its stable chemical properties. This strain mismatch between the bilayer generates the self-assembly force and detaches the whole structure from the substrate with the etching of sacrificial layer. In the end, this polymeric bilayer is transferred to the “Swiss-roll” structure under precise control.

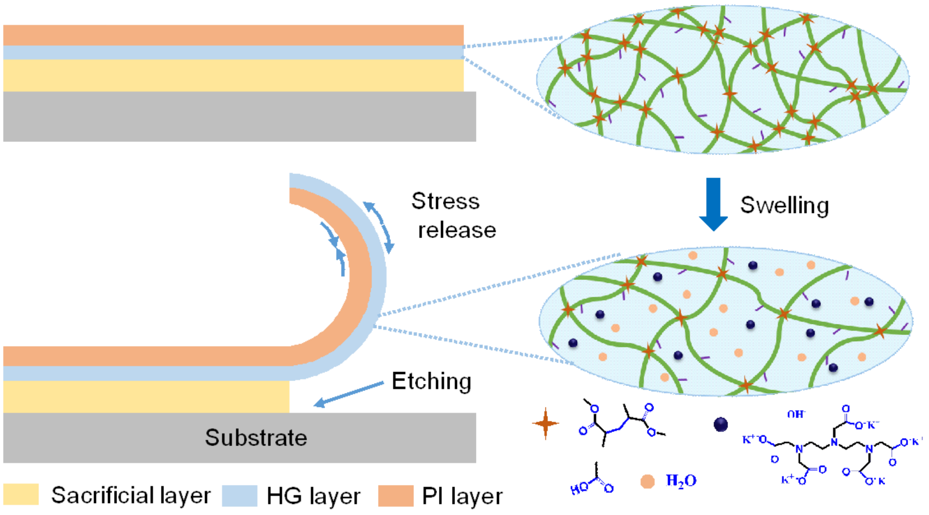

Figure 3.4. Diagram of self-assembly process of polymeric bilayer induced by hydrogel swelling.

To construct polymeric “Swiss-roll” structure，sacrificial layer as the first step in the microfabrication is required to be patterned and stable in is water, organic solvents as well as the developer of strain bilayer. Thus, a special metal-organic framework was synthesized based on the lanthanum (La)-acrylic acid (AA) complex. Under the action of photosensitizer, a standard 365-405 nm UV radiation can initiate the photopolymerization of La-AA complex to form a polyacrylic acid (PAA) network (Figure 3.5a).[160] The hydrogel part was prepared from poly(ethylene-alt-maleic anhydride) (PEMA) by grafting *N*-(2-hydroxyethyl) methacrylate (HEMA) or *N*-(2-hydroxyethyl) methacrylamide (HEMAm) onto its anhydride groups (Figure 3.5b). The final modified polymer contains acrylate functional groups which would then polymerize via radical polymerization with the help of a UV radical initiator. For the reinforcement layer (Figure 3.5c), photosensitive PI layer with pendant acrylate functional groups was specially synthesized to meet requirements including thermal, chemical and mechanical stability, good adhesion to the hydrogel layer and a direct UV patternability.

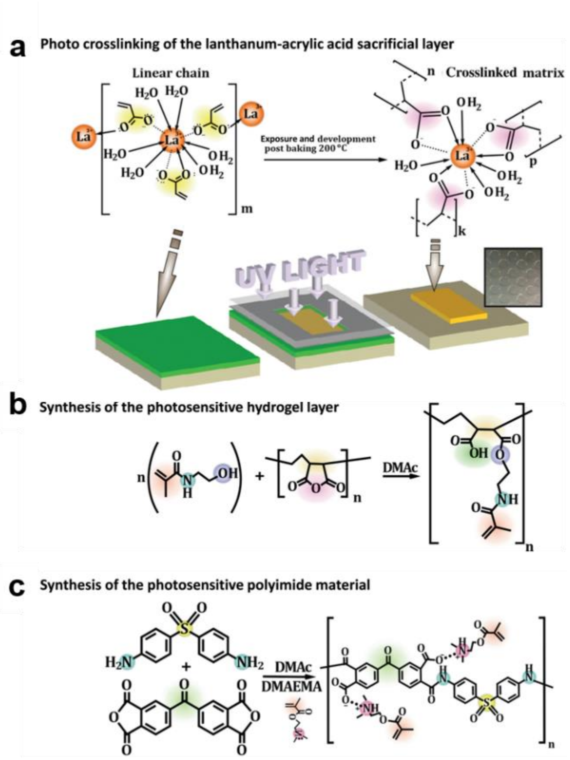

Figure 3.5. a) Modification of poly(ethylene-alt-maleic anhydride) by grafting *N*-(2-hydroxyethyl) methacrylamide in *N*,*N*-dimethylacetamide solvent. b) Photocrosslinking of the lanthanum-acrylic acid complex by UV radiation in the presence of a photoinitiator followed by development and postbaking leads to lithography compatible sacrificial layer patterns. c) Synthesis of the photosensitive PI precursor material via the reaction of 3,3′,4,4′-benzophenonetetracarboxylic dianhydride and 3,3′-diaminodiphenylsulfone, with a subsequent modification with dimethylaminoethyl methacrylate and the inclusion of a photoinitiator.[160]

3.2.2. Self-assembled polymeric layers for microelectronics

The operating efficiency of antennas can be enhanced by small antennas with 3D architectures.[160] Therefore, “Swiss-roll” antenna using rolled-up technology was explored by Karnaushenko *et al.* (Figure 3.6a-c).[158] Two linear metal layers consisting of Ta (10 nm)/Cu (100 nm)/Ta (10 nm) were fabricated on the polymeric layer stacks and then transferred into the helical structure after being rolled up. The advantage of this geometry is that different antennas with various electromagnetic properties can be created by adjusting the planar pattern of the conductors and defining the diameter, winding number, and the interwinding spacing for precise impedance matching. This enables the operation of an antenna free of additional external matching components while maintaining optimal transmission efficiency at mesoscopic scales. Another benefit of this tubular geometry is its mechanical stability that maintains the helical shape under external compression and physical manipulation, regardless of whether the antenna is encapsulated or not.[159]

Ideal inductors should possess high inductance values and minimized wire resistance as well as magnetic core losses. By reconstructing a conductor into a loop profile, an ideal inductor with the circular profile is formed and supports the highest magnetic flux for a given piece of wire by carrying an electrical current with the lowest possible losses.[142] Therefore, the tubular structure is beneficial for constructing 3D inductors. More recently, a self-assembled solenoid with high inductance on a large scale and parallel lithographic fashion was realized (Figure 3.6d).[159] The self-assembly process was harnessed to form two flat, cable-like solenoid inductors with a diameter of 300 μm by applying planar layouts of various Π-shaped loops. They showed for the first time that shaping of the initially planar structure like a conductor can lead to >50 times more compact 3D inductive coils with enhanced up to four times inductance, reaching >100 nH at MHz regime.

The swiss-roll architecture can also be used for the sensing of ultra-small magnetic fields, achieved through measuring the inductive response of the coil when the core is subjected to an alternating current.[160] Thus, tubular giant magneto-impedance sensors which are integrative in CMOS compatible process were created by self-assembling initially planar NiFe-/Cu/NiFe-based heterostructures into 3D tubular architecture (Figure 3.6e). In this way, the most crucial aspect of giant magneto-impedance fabrication technology, i.e., the formation of a circular magnetization, was overcome.

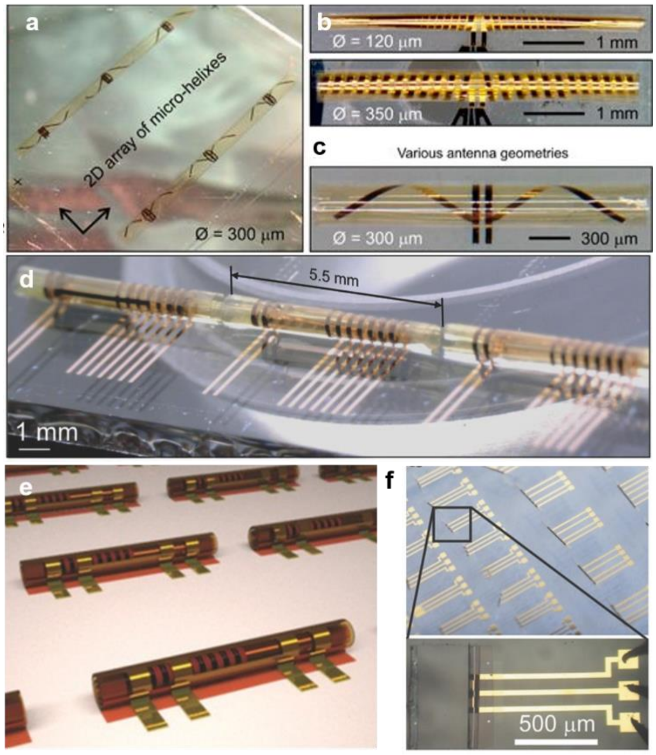

Figure 3.6. a,b,c) Different 3D self-rolled helical impedance matched antennas fabricated on glass substrates enabled by strained polymer layer bending.[158] d) Self-assembled microcoil structures that include inductors and their mutually coupled configurations-transformers.[159] e) Array of self-assembled giant magneto-impedance sensors with pick-up coils.[139] f) Array of self-assembled IGZO transistors, logic elements, and amplifiers. The inset in (b) shows a tubular architecture accommodating one IGZO transistor device with the channel along the tube axis.[140]

Combining mechanical adaptivity of soft actuators with the imperceptibility of microelectronics paves the way toward an entirely new class of devices-smart biomimetics. Smart biomimetics can mechanically adapt to and deterministically impact the environment electrically or mechanically.[140] Rolled-up technology based on polymeric platform was utilized for the construction of novel microscale regenerative neuronal cuff implants (Figure 3.6f).[140] In this work, they realized mechanically adaptive microchannels with integrated microelectronics, including signal amplifiers and logics based on high-performance indium gallium zinc oxide (IGZO) transistors. The shape of the device can be deterministically chosen to be planar, bent, or self-assembled into a “Swiss-roll” like microtube with a tunable diameter down to 50 µm. The integrated microelectronics also allows monitoring the presence of tiny amounts of ionic liquids in the channel, mimicking the detection of polarization/depolarization processes in neural micro-conduits.

Chapter 4. Experimental methods

4.1. Deposition methods

4.1.1. Photolithography

In this work, several commercial photoresists are used. AZ5214E as the example is an image reversal photoresist. With negative exposure, its pattern has a large undercut profile after the development procedure. This feature enables physically deposited nanomembrane easily being lifted off from the substrate. ARP 3510 is a positive type photoresist, which is stable in acid solution and is usually used as a protection mask for the wet-etching process. Another advantage of this photoresist is its slope structure at the edge of the pattern. After the deposition of nanomembranes using a titling deposition method, rolled-up tubes have good detachment properties on the substrate.

4.1.2. Electron beam evaporation

Electron beam evaporation, also known as e-beam evaporation, is a mature technique for preparing metal and oxide thin film. As shown in Figure 4.1, the e-beam evaporator usually consists of an electron source, a crystal detector, crucible with target on holder, and water cooling system. In the high vacuum (10^{-6} mbar~10^{-8} mbar) chamber, an electron beam can be generated by applying a high voltage in electron source, and then focused onto the target material in the crucible by using a magnetic field. Thus, the thermally heated target material is evaporated onto the top substrate in an atomic form. Simultaneously the thickness and deposition rate of the thin film can be monitored by the frequency change in crystal detector.

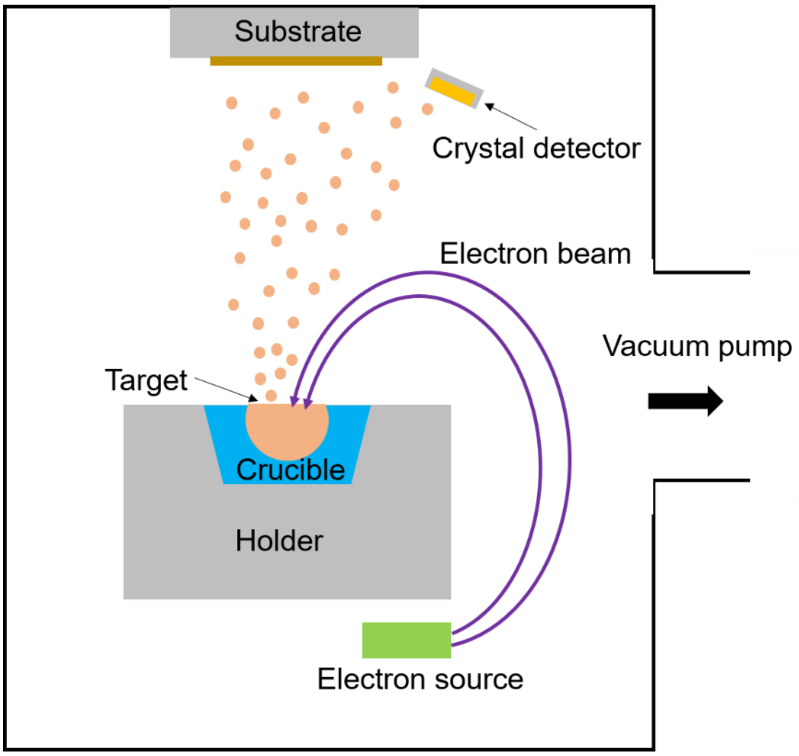

Figure 4.1. Schematic diagram of electron beam evaporation system.

In this thesis, e-beam evaporation (Edwards auto 500 FL500, England) was used for the fabrication of current collectors (*e.g.* Cr/Au). On the other hand, thin films deposited by e-beam evaporator possess large residual stress by controlling deposition parameters like the substrate temperature, chamber pressure, film thickness and deposition rate. Thereby e-beam deposition method was also used for the study on the rolling of inorganic nanomembrane (*e.g.* Ni, SiO_2, Au/Ti/Cr).

4.1.3. Atomic layer deposition

Atomic layer deposition (ALD) has emerged as an important technique for depositing thin films for a variety of applications. ALD can meet the needs of atomic layer control and conformal deposition using sequential, self-limiting surface reactions.[161] In the typical ALD process for a binary compound, two gas-phase molecules are alternately exposed to a substrate in an ABAB... sequence. The (A) gas exposure reacts with surface species, adds the first desired atomic element, and changes the surface species. The subsequent (B) gas exposure reacts with the new surface groups and adds the second desired atomic element. This second reaction also changes the surface groups back to the original surface species.[162]

In this work, Al_2O_3 ALD (FlexAL, Oxford instruments) was used for fabricating of insulting layer of micro-devices. A schematic showing one cycle of Al_2O_3 deposition during ALD is displayed in Figure 4.2. The ALD processes are based on binary reaction sequences where two surface reactions occur and deposit a binary compound film. The hydroxyl-terminated starting surface is exposed to a metal-organic precursor (Trimethylaluminum, TMA) that reacts with the surface in a self-limiting reaction. Once the system is purged with an inert gas to remove excess precursors and by-products, a second co-reactant (water) is introduced and reacts to form one monolayer of Al_2O_3 ALD. The ending hydroxyl-terminated surface is similar to the starting surface, allowing the process to be cycled to grow the desired film thickness.

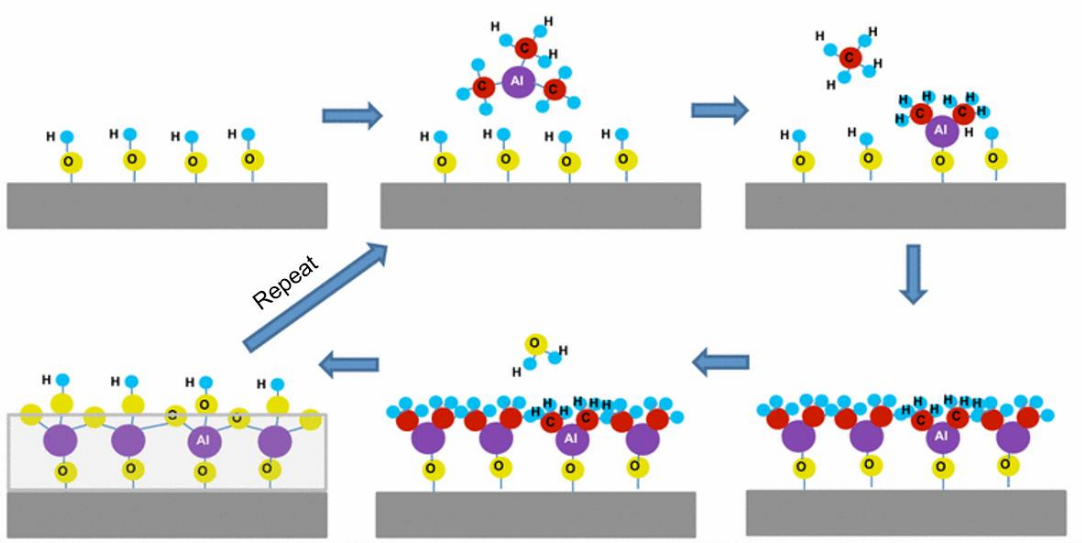

Figure 4.2. ALD process: schematic of one cycle of Al_2O_3 ALD growth.[163]

4.1.4. Electrochemical deposition

Electrochemical deposition is a method using the redox reaction to synthesize films on a conductive substrate. In this process, the electricity from an external power supply is introduced at the interface between the electrode and the electrolyte. Subsequently, the precursor ions of objective materials in the electrolyte adhere to the electrodes by electrostatic attractive interaction followed by chemical synthesis. Electrochemical deposition can achieve an extremely thin deposition layer via a cost-effective process and also create very strong bonds between the two materials, allowing the finished products to have a durable coating. Up to now, electrochemical deposition process has been widely used to fabricate thin-film electrodes of carbon materials such as activated carbon,[39] CNTs,[164] and graphene,[165–168], as well as metals[29,169], transition metal oxides[23,169–177] and conducting polymers.[27,178–182]

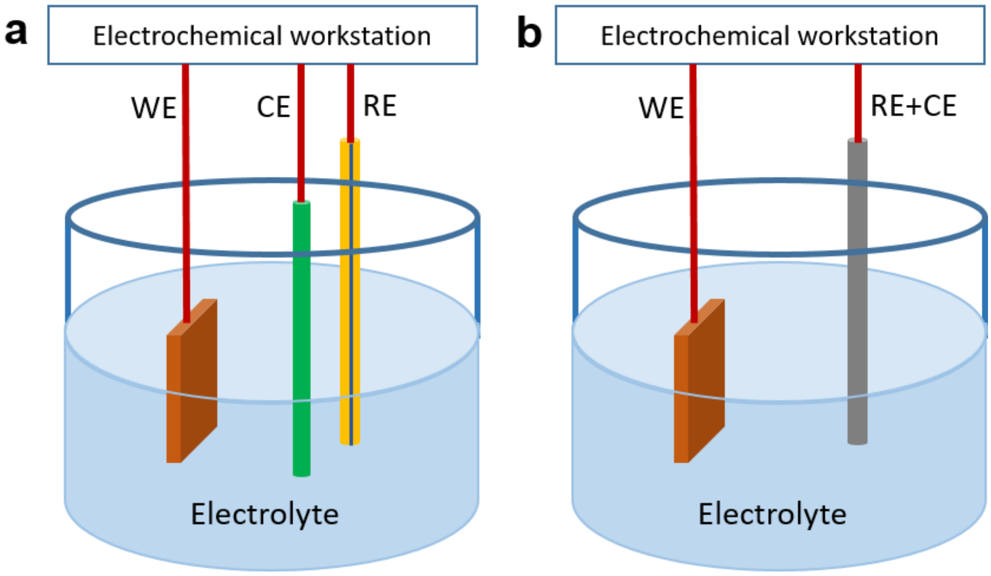

Figure 4.3. Electrochemical deposition configurations: a) three-electrode system and b) two-electrode system in which the counter and the reference electrodes are shorted.

To electrodeposit the material on a conductive substrate, both two-electrode and three-electrode configurations can be performed. Figure 4.3 gives a schematic view of a cell connected to an electrochemical workstation. The current flows through the counter electrode (CE) and the working electrode (WE), and the voltage is measured (or controlled) between the reference electrode (RE) and the WE. Generally, the electrodeposition occurs on WE. For a three-electrode cell (Figure 4.3a), the RE (*e.g.* Ag/AgCl, Hg/HgO) should exhibit an ideal non-polarizable behavior, meaning that its voltage is constant over a large range of current densities. In this way, the WE voltage is accurately measured (or controlled). For a two-electrode cell (Figure 4.3b), the voltage measured (or controlled) is the cell voltage since the CE and the RE are shorted. In this work, the active materials were electroplated on WE by using the three-electrode system (μAutolabIII, Metrohm).

4.2. Characterization methods

4.2.1. Scanning electron microscopy and focused ion beam milling

Scanning electron microscopy (SEM) is a precious tool for the analysis of the most different materials including organic and inorganic materials on a nanometer to micrometer scale. The popularity of the SEM can be attributed to many factors: the versatility of its various imaging modes, the excellent spatial resolution, the modest requirement on sample preparation and condition, the relatively straightforward interpretation of the acquired images, the accessibility of associated spectroscopy and diffraction techniques. And most importantly its user-friendliness, high levels of automation, and high throughput make it accessible to most research scientists.[183]

When the primary electron beam scans the sample surface, depending on the material and the set acceleration voltage, secondary products are created in a so-called interaction volume (excitation bulb) that can be used for imaging and analysis. The signals used most frequently for the creation of images are the secondary electrons and backscattered electrons. In addition, materials are often identified by using the generated X-rays that are analysed using an energy dispersive X-ray or wavelength dispersive X-ray spectrometer.

In this work, focused ion beam (FIB) milling combined with SEM (CrossBeam Workstation NVision40, ZEISS) was also used for imaging the cross-section of samples. The FIB can directly modify or "mill" the specimen surface with an ion beam (*e.g.* Ga ions), and this milling can be controlled with nanometer precision.

4.2.2. Electrochemical characterization

CV, a widely used potential-dynamic electrochemical technique, can be employed to obtain qualitative and pseudo-quantitative data about electrochemical reactions including electrochemical kinetics, reaction reversibility, reaction mechanisms, electrocatalytic processes, and effects of electrode structures on these parameters. The principle of this technique is to apply a linear voltage ramp to an electrode (or a device) between two voltage limits and to measure the resulting current. The applied voltage in the first cycle of CV is as follows:

$$V\ (t) = V_1 + \vartheta t \ \text{ for V } \geq V_1$$

$$V\ (t) = V_2 - \vartheta t \ \text{ for V } \leq V_2$$

where ϑ is the scan rate (V s^{-1}), V_1 and V_2 are the boundaries of voltage window. The areal specific capacitance (C_A) of the device can be calculated from CV curves according to equation as follows:

$$C_A = \frac{1}{2A\vartheta(V_2 - V_1)} \int_{V_1}^{V_2} I\, dV$$

where A is the footprint area of device, I is the current in CV measurement.

Galvanostatic charge/discharge (GCD) is carried out by applying constant current on device and monitoring its voltage along with time. It is one of the most reliable approaches to determine capacitance energy density, power density, equivalent series resistance, and cycle life of a supercapacitor. In this work, the areal specific capacitance (C_A) of the device was calculated from GCD curves according to equation as follows:

$$C_A = \frac{I}{A} \times \frac{\Delta t}{\Delta V} \qquad 1)$$

where C_A (in mF cm^{-2}) is the areal capacitance of device. For tubular device, the footprint area A is equal to the length multiplied by the average diameter of the 3D tubular device, ΔV is the difference between the final potential and initial potential (v), I is the applied constant current (A), and Δt is the discharge time (s).

The gravimetric specific capacitance (C_M) and volumetric specific capacitance ($C_{V\text{-Planar}}$, $C_{V\text{-Roll}}$) of the device were calculated from GCD curves according to Equation 2, Equation 3 and Equation 4:

$$C_M = \frac{I}{M} \times \frac{\Delta t}{\Delta V} \qquad 2)$$

$$C_{V-Planar} = \frac{I}{V1} \times \frac{\Delta t}{\Delta V} \qquad 3)$$

$$C_{V-Roll} = \frac{I}{V2} \times \frac{\Delta t}{\Delta V} \qquad 4)$$

where M is the mass of the electrode, $C_{V\text{-}Planar}$ is the volumetric capacitance of the planar device, V1 is the volume of the planar device (Footprint area × Thickness), $C_{V\text{-}Roll}$ is the volumetric capacitance of tubular device, V2 is the tube volume of tubular device.

The areal energy density (E_A, Wh cm^{-2}) and power density (P_A, W cm^{-2}) were calculated according to Equations S5 and S6:

$$E_A = \frac{1}{2} \times C_A \times \frac{(\Delta V)^2}{3600} \qquad 5)$$

$$P_A = \frac{E_A}{\Delta t} \times 3600 \qquad 6)$$

Chapter 5. An integrated MSC with thermo-responsible function

5.1. Introduction

Thermo-responsive electrolytes introduced in Chapter 2 have greatly promoted the development of thermo-responsive supercapacitors. Those supercapacitors not only possess high electrochemical performance with good durability but also is endowed with impressive capability to respond to the external temperature change. Therefore, the integration of MSCs with thermo-responsive electrolyte can open the opportunity to realize intelligent thermal protection towards miniaturized electronic devices.

This chapter is based on the publication of *Energy Environ. Sci.,* **2018**, 7, 1717-1722, titled “*Thermoswitchable On-Chip Microsupercapacitors: One Potential Self-Protection Solution for Electronic Devices*”. My contribution to this work mainly includes the design and the microfabrication of planar interdigital MSC electrodes using standard photolithography technology. In this regard, single devices and multiple devices connected in parallel/series were designed and investigated. Besides, SEM was carried out to characterize the morphology of the PEDOT active material.

5.2. Fabrication and characterization of thermo-responsible MSCs

5.2.1. Single thermo-responsible MSCs

The fabrication process of interdigital electrodes on Si/SiO_x and PI film is illustrated in Figure 5.1. Firstly, samples were cleaned by solvents including the acetone and isopropanol. An O_2 plasma cleaner with the power of 100 W was further used to remove the residue on the sample surface. Photoresist AZ5214E was spun coated at 6000 rpm for 60 s over the cleaned Si/SiO_2 or PI substrates. Photoresist coated substrates were soft-baked to remove the solvent at 90 ^oC for 4 min. The negative exposure was performed using maskless aligner (Heidelberg μPG 501, Germany) to establish the interdigital patterns. In the case of low intensity of UV exposure (7 mS), the exposed photoresist areas near the substrate receive substantially less UV light than the photoresist surface resulting in a more pronounced undercut of the resist profile (Figure 5.1c).[184]

After this, hard-baking at 120 °C for 2 min crosslinked the exposed photoresist and simultaneously unexposed areas have not been affected. Then, flood exposure for 30 s were further performed to expose the unexposed photoresist. The treated substrates were developed in AZ726 MIF developer solution for 1 min to remove the uncrosslinked photoresist and form interdigital patterns on the substrate. After the O_2 plasma cleaning, metallic layers of 30 nm Au/10 nm Cr were deposited by e-beam evaporator (Edwards auto 500 FL500, England) over the patterned photoresist layer. Benefit from the undercut profile, the Au/Cr deposited on the photoresist layer was completely lifted off in hot DMSO and thus patterned interdigital Au/Cr with desired structure was achieved on substrates.

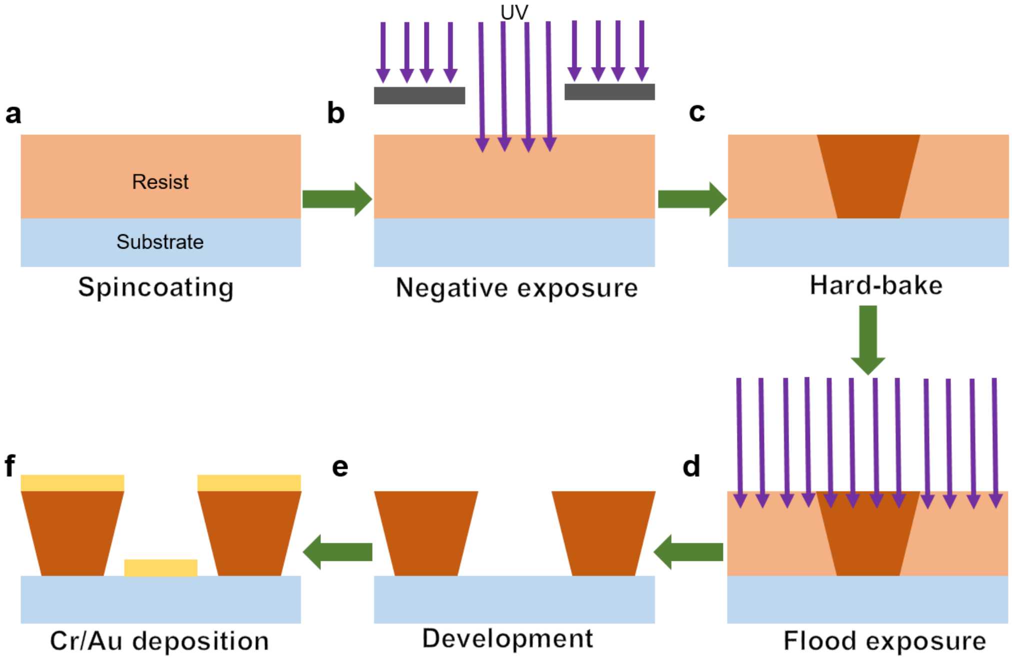

Figure 5.1. Schematic illustration of the microfabrication of interdigital electrodes.

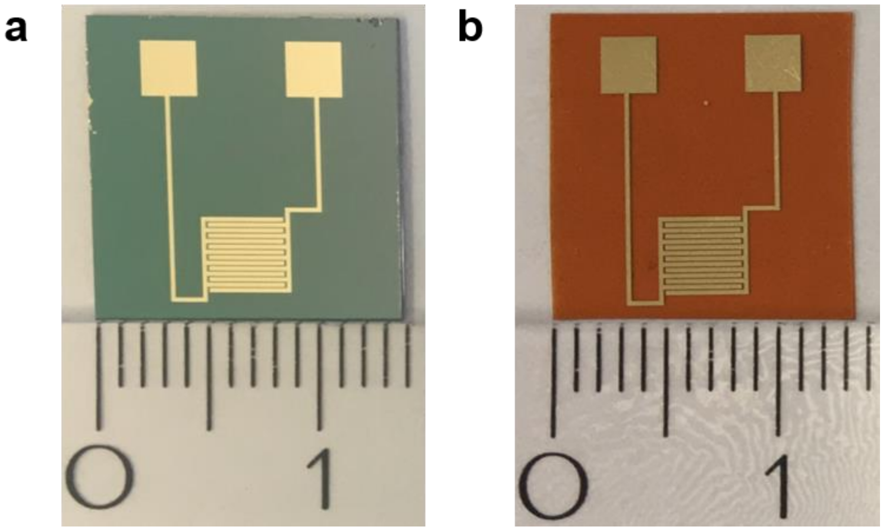

Figure 5.2. Digital photographs of patterned interdigital electrodes on a) Si/SiO$_x$ and PI substrates.

PEDOT was electrochemically polymerized on Au electrodes in a standard three-electrode system using a patterned interdigital Au/Cr electrode as the working electrode, a Pt wire as the counter electrode, and Ag/AgCl (saturated KCl) as a reference electrode. The electrolyte solution contained 10 mM of 3,4-ethylenedioxythiophene (EDOT), 10 mM of sodium dodecyl sulfate (SDS), and 1 M of H_2SO_4. A constant anodic potential of 0.9 V was applied for 3 min during the process. Then the interdigital PEDOT/Au/Cr electrode was washed with deionized water and air dried at room temperature.

Furthermore, poly(N-isopropylacrylamide)-g-methylcellulose (PNIPAAm/MC) as thermo-responsive electrolyte mixed with LiCl gel was performed by Prof. Xinliang Feng's group to endow in-plane PEDOT based MSCs thermo-responsible function. As shown in Figure 5.2, MSCs on SiO$_x$ and PI substrates were gradually heated from room temperature, while the gel-type electrolyte on electrodes was simultaneously gradually transformed from a brightly transparent state to a dimly white state. When the device temperature was cooled to room temperature, the state of electrolyte was also transformed to the origin. The mechanism of this phenomenon is based on reversible sol-gel transition under different temperatures in PNIPAAm/MC material. During the heating treatment, side-chain PNIPAAm collapses and forms hydrogels through hydrophobic association, which can thus inhibit the free movement of Li^+ ions in gel-type electrolyte, implying the elimination of the conductive pathway between electrodes. When turning to the cooling process, such a copolymer can easily stretch back into a relaxed state due to the formation of hydrogen bonds between *N*-isopropyl groups and water.

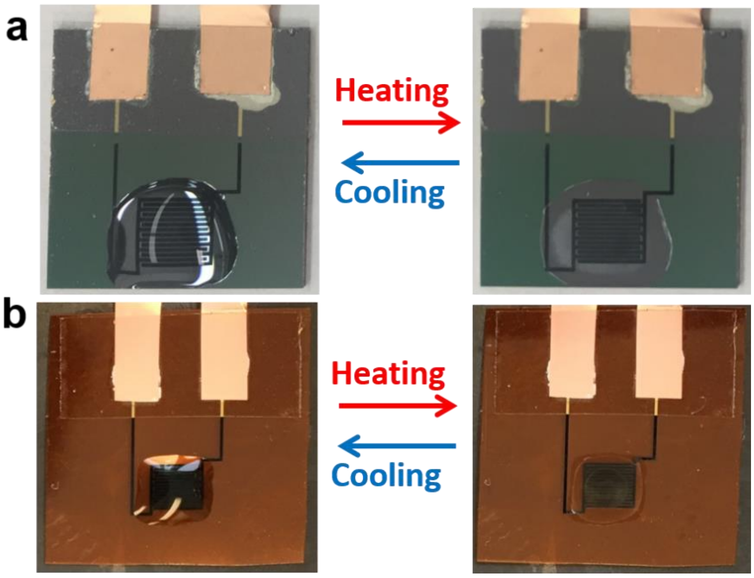

Figure 5.3. Digital photographs of single thermo-response MSCs upon heating and cooling on a) a rigid Si/SiO_2 wafer and b) a flexible PI film

PEDOT was selected as the active electrode material for thermo-responsive MSCs, as it can be deposited over large area and is electrochemically stable.[185] Electrochemical polymerization of PEDOT is a process by imposing a sufficiently positive potential through the solution of EDOT. The PEDOT film can progressively grows at the Au electrode surface. Generally, thiophene and its derivatives require anhydrous organic medium for the electro-polymerisation process as they are weakly soluble in water. In addition, the higher oxidation potentials of thiophene derivatives would pose a challenge for the electro-deposition process as the stable potential window of aqueous media is only up to 1.23 V.[186] To solve these issues, anionic surfactants such as SDS was employed to increase the solubility of the EDOT while reducing the oxidation potential required for the electrodeposition process. This surfactant media can also help in stabilizing the thienyl cation radicals ($EDOT^{\cdot +}$), simultaneously produce template effects at thee-electrode surface in obtaining the nanostructured conducting polymer.[184,187] The electro-polymerization process of PEDOT can be illustrated as follows:[188]

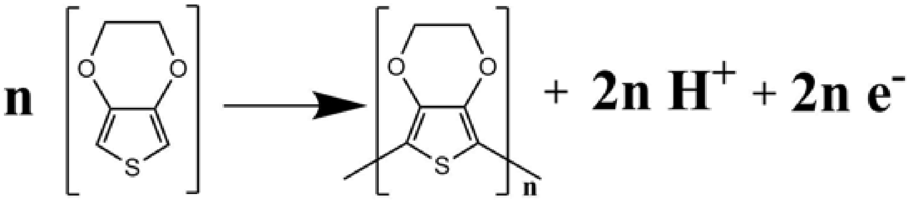

This electro-oxidation process results in linear polymer chains, with chemical bonds between neighbouring monomer units formed in the way that the chain also corresponds to a conjugated structure.[188] The SEM image in Figure 5.3a shows a representative morphology of the PEDOT thin films (3 mins of deposition time). Numerous nanoscale porous structures can be discovered in the PEDOT film. Thus, it greatly improves the specific area of electrodes and the infiltration efficiency of electrolyte ions.

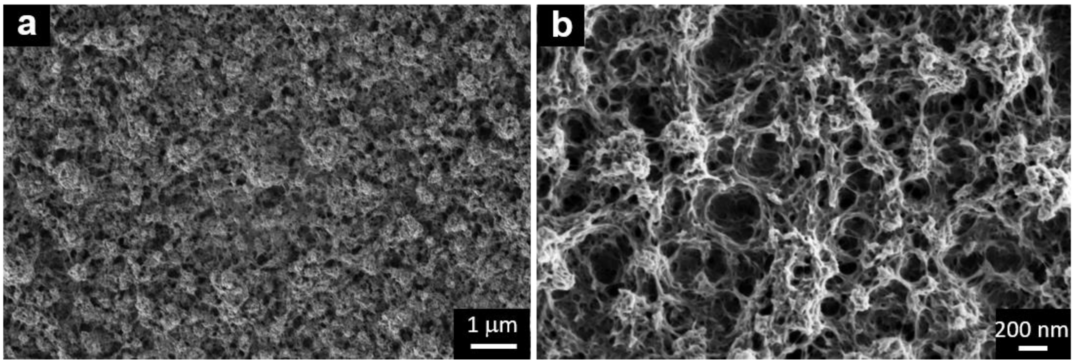

Figure 5.4. SEM images of PEDOT surface with a) low magnification and b) high magnification.[189]

5.2.2. The array of thermo-responsible MSC

The voltage and capacity of single MSCs are limited and hard to meet the demands of many portable and wearable electronics. It is effective to solve this problem by connecting multiple MSCs in series and parallel to enhance the output voltage and capacity respectively. As shown in Figure 5.5, four MSCs connected in serial and parallel on shared substrates were designed and fabricated with photolithography technique by one step. The MSCs are connected by sharing current collectors instead of additional circuits. The electrochemical performance was then measured by Prof. Xinliang Feng’s group, the MSC array with four units connected in series can reach a high operational voltage of 3.2 V (Figure 5.5b). In this tandem MSC, one of the units was covered with thermo-responsive electrolyte. After it was heated to 80 ^{o}C from 30 ^{o}C, the GCD curve clearly shows that the decrease of the charge and discharge time. Under high temperature, thermo-responsive electrolyte can cut off the entire power supply from tandem MSCs. In addition, the MSC array in a parallel configuration exhibits an enhanced capacitance compared with that of a single unit. Similarly, one of the parallel MSCs was also covered with thermo-responsive electrolyte. After devices were heated under 80 ^{o}C, the capacitance of parallel devices has an obviouse decrease, but part of the original capacitance is still maintained.

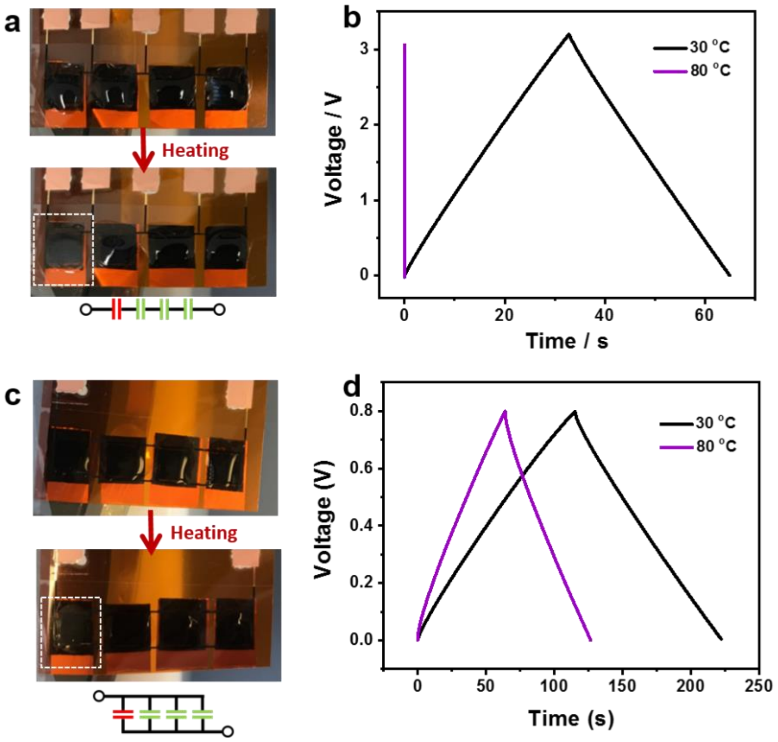

Figure 5.5. Digital photographs of four thermo-response MSCs connected in a) series and c) parallel upon heating on a flexible PI film; GCD curves of thermo-responsive MSCs connected in b) series and d) parallel under cooling and heating states.

To further satisfy the demands of future microelectronics, developing integrated power sources with ultra-high voltage and capacitance output is highly required. Based on the advantage of photolithography technique, 100 interdigital Cr/Au current collectors concocted in parallel for each line and 10 lines in series were successfully fabricated on a 3-inch SiO_x wafer (Figure 5.6). Afterward, the electrodeposition method was employed to deposit PEDOT on the electrode surface. This fabrication process demonstrates that such two techniques (photolithography and electrodeposition) can be combined to fabricate wafer-scale MSCs. In addition, two separate electrical circuits are extending to outside for each line of 100 MSCs. Thus, it has a highly adjustable voltage and capacitance output according to actual requirements.

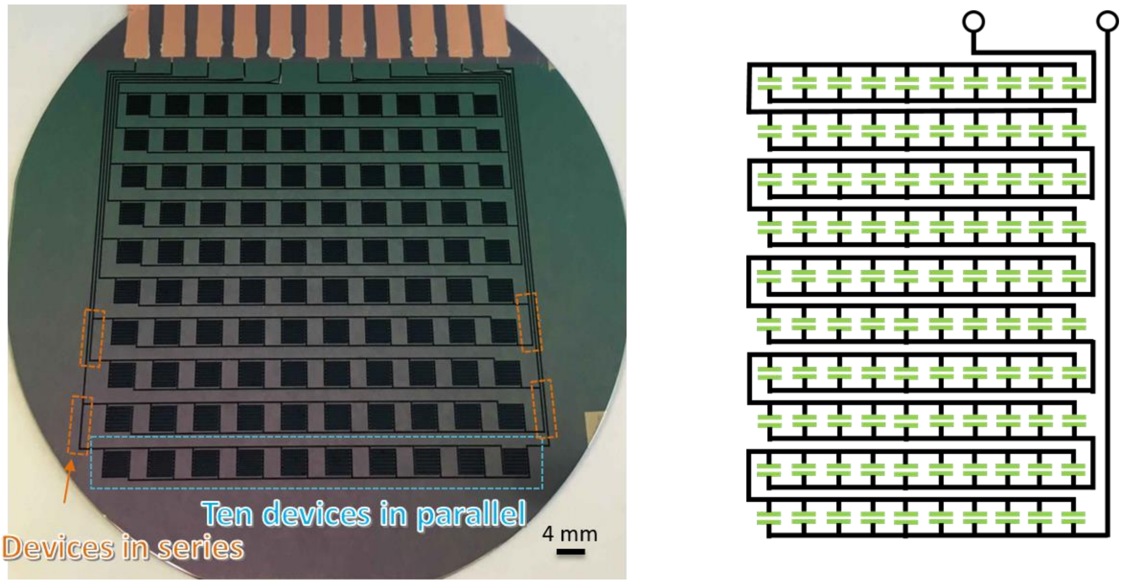

Figure 5.6. Digital photograph of 100 MSCs with 10 MSCs in parallel for each line and 10 lines in series on a 3-inch SiO_x wafer.

5.3. Conclusion

In conclusion, planar interdigital MSCs were successfully fabricated with the combination of the photolithography technique and electrodeposition method. Among this, PEDOT material was primarily explored as the active electrode to achieve MSCs with the thermo-responsible function. The porous structure of PEDOT can greatly improve the specific area of electrodes and the infiltration efficiency of electrolyte ions. Such fabricated MSC exhibited a broad temperature window (30-80 ^oC) and switch-off behavior at 80 ^oC. In addition, four MSCs and 100 MSCs connected in series and parallel were also designed and fabricated, demonstrating that the voltage and capacitance output can be adjustable by such fabrication techniques.

Chapter 6. Self-assembly of 3D tubular MSCs

This chapter is based on the publication of *ACS Nano,* **2019**, 7, 8067-8075, titled "*Self-Assembly of Integrated Tubular Microsupercapacitors with Improved Electrochemical Performance and Self-Protective Function*". My contribution here mainly includes: 1) the microfabrication of tubular MSCs. 2) electrochemical measurements for on-chip and free-standing tubular MSCs with different thickness of PEDOT. 3) the exploration of the self-protection function of tubular MSCs.

6.1. Introduction

MSCs are important components for a variety of applications, including portable/wearable devices, implantable medical devices, lab-on-a-chip devices, micro-autonomous systems and maintenance-free electronics which make up the Internet of Things.[2,3,190–193] Owing to major advantages such as long operating lifetime (> 100 000 cycles), fast charge/discharge rates as well as high power density,[4,63] MSCs are not only complementary to micro-batteries, but can also store renewable electricity which is converted from solar, mechanical, and thermal energy.[1,194] However, a cost-effective and reliable fabrication procedure which is compatible with modern microelectronics industry has not been sufficiently well developed for MSCs, so far. Several features are critical for production and application of MSCs, for instance, 1) high areal performance within small footprint; 2) integration of multiple properties and functions such as mechanical and thermal protection; 3) compatibility with parallel facile mass production, transfer, encapsulation and integration with microelectronic circuitry.[4,111,195–199] These demands require clever exertion of diverse materials and micro-/nanofabrication technologies.

Conventional capacitors used in electronic circuits adopt a cylinder shape, in which capacitor laminates consisting of planar electrodes and insulating layers are folded or wound into "Swiss-roll" structures. This origami design compresses large-area membranes into compact tubular structures, massively improving the form factor and electrochemical performance in electronic circuits. In addition, the cylinder geometry can provide fixation and mechanical protection, which are required for the integration of capacitors into circuits by automated pick-and-place processes. Hence, inspired by origami art, the technology transfer of this assembling route into the microscale represents an efficient strategy for constructing integrated 3D MSCs.[200]

Similar to the curling of a strained metal layer which was reported more than 100 years ago by Stoney,[143] nanomembranes consisting of different materials (*e.g.* metals, semiconductors, oxides, molecules, and polymers) can self-assemble into rolled-up microtubes when the layers are delaminated and built-in strain is released.[136,137,145,201–205] This self-assembly process smartly combines top-down and bottom-up methods to pattern functional nanomaterials into ordered 3D micro-/nanostructure arrays. For instance, planar nanomembranes can be reshaped into their “Swiss-roll” counterparts to create new energy storage materials and 3D generations of devices such as sensors, passive and active electronic devices as well as soft organic and bio-interfaces.[138,159,206–208] One promising advantage of this approach is that such origami structure endows devices and materials better functionality and performance.

In this work, a universal microfabrication route is present to achieve “Swiss-roll” MSCs by employing shapeable materials and strain engineering. The PI-reinforced hydrogel layer can induce mechanical strain when the sacrificial layer below is selectively etched away and the hydrogel swells in water. Based on the experience of the microfabrication and PEDOT deposition in the last chapter, PEDOT functionalized interdigital electrodes are self-assembled into compact “Swiss-roll” structures to deliver power within greatly reduced footprint areas. Simultaneously, hydrogel incorporated into the shapeable polymer framework wraps around and moisturizes the electrodes, generating efficient ion transport. Such on-chip tubular MSCs show areal capacitance up to 82.5 mF cm^{-2} at a current density of 0.3 mA cm^{-2}, which is 900 % higher than for state-of-the-art PEDOT-based MSCs. The robust structure of tubular MSC is the key to improve the capacitance retention up to 96.6 % over 5000 cycles, and it surprisingly provides an efficient protection against the external compression up to a pressure of about 30 MPa. Moreover, “free-standing” tubular MSC arrays can be transferred onto objective paper/glass substrates. Tubular MSCs connected in parallel and series significantly improve energy density and enhance voltage output. Such free-standing devices provide a feasible route for mass production of stand-alone integrated tubular MSCs compatible with modern microelectronics and automated “pick-and-place” processes.

6.2. Fabrication of tubular MSCs

6.2.1. Diagram of processing flow

The fabrication flow for PEDOT-based tubular MSCs is illustrated in Figure 6.1. First, a metalorganic La-acrylic acid complex was patterned on SiO_2/Si or flexible PI substrate to form the sacrificial layer followed by patterning a shapeable bilayer consisting of a 700 nm-thick hydrogel layer and a 1400 nm-thick PI layer. These materials rely on acrylate-based chemistry allowing a direct lithographic definition of the structures, which are compliant with regular parallel planar photoresist patterning routines of microfabrication technologies. Their chemical and thermal stabilities provide further reliable microfabrication on their surface of, for instance, interdigitated electrodes, which were prepared by lithography and electrodeposition.[139,140,158,159] The planar MSC was self-assembled into a tubular architecture by selectively etching the sacrificial layer in potassium diethylenetriaminepentaacetic acid (DTPA) solution (pH=10).

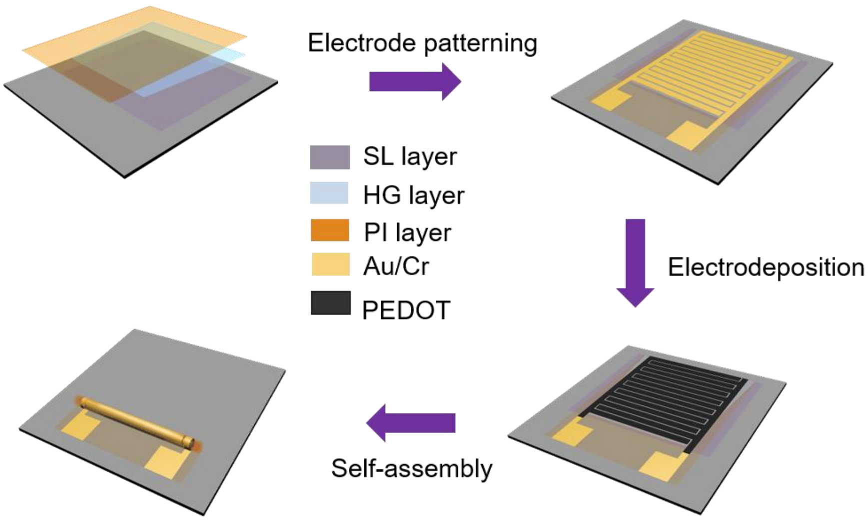

Figure 6.1. Schematic illustration of the fabrication of a tubular MSC based on interdigital PEDOT electrodes.

6.2.2. Polymeric layer stack

Sacrificial layer: 10 g of acrylic acid was partially neutralized using NaOH until the solution reaches pH = 5.5. Then 7.36 g of $LaCl_3 \cdot 7H_2O$ dissolved in 50 ml of DI was added to achieve the proportion of AA: La = 7:1. In the subsequent stirring, the pH was slowly increased to 10 by adding NaOH. The lanthanum complex precipitates were collected and washed by DI water until litmus test paper showing a neutral reaction. As a final step, the dried and milled powder was dissolved in AA at the concentration of 33% (wt/wt), photosensitized using 2% (wt/wt) of 2-Benzyl-2-(dimethylamino)-4-morpholino-butyrophenone and 4% (wt/wt) methyl diethanolamine. The sacrificial layer solution was spin-coated onto O_2 plasma-cleaned substrates at 5000 rpm for 90 s. The samples were then baked at 40 ^oC for 10 min for solvent removal and further exposed (365 nm, 15 W cm^{-2}) for 4 min through a glass/Cr photomask using a SÜSS MJB4 mask aligner (SÜSS MicroTec SE, Garching, Germany). The patterned samples were developed in deionized water for 4 min and finally baked at 220 ^oC for 20 min to obtain a stable sacrificial layer.

Hydrogel layer: For the preparation of hydrogel solution, 6 g of poly(ethylene-alt-maleic anhydride) was dissolved in the 50 ml of N,N-Dimethylacetamide, then 5.66 g of N-(2-hydroxyethyl)methacrylate was added. All components were mixed thoroughly for 24 h at room temperature by roll-mixer to finish the reaction. In the end, the hydrogel solution was photosensitized with 4% (wt/wt) of 2-Benzyl-2-(dimethylamino)-4-morpholinobutyrophenone. Then it was then spin-coated on top of the sacrificial layer at 5000 rpm for 90 s. After baking at 40 ^oC for 5 min, samples were exposed under UV light (365 nm, 15 W cm^{-2}) for 6 min through the glass/Cr photomask using SÜSS MJB4 mask aligner. The development of hydrogel layers was done in 2-(2-Methoxyethoxy) ethanol for 2 min and rinsed in propylene glycol methyl ether acetate to remove unexposed polymer. Finally, the samples were hard-baked at 220 ^oC for 5 min, resulting in a layer with the thickness of ~800 nm.

Polyimide layer: The polyimide solution was firstly prepared by the reaction of 12 g of 4,4'-Methylenedianiline and 19.65 g of 3,3',4,4'-Benzophenonetetracarboxylic dianhydride. Both monomers were dissolved in 20 ml N,N-Dimethylacetamide and gradually over an hour reacted together under culling conditions at 15 °C, resulting in the highly viscous solution. Then a dimethylaminoethyl methacrylate was added in a 1:1 molar ratio to the number of carboxylic groups in BPDA. The solution was left in the mixer for 4 h under cooling condition to complete the reaction. In the end, the polyimide solution was photosensitized with 4% (wt/wt) of 2-Benzyl-2-(dimethylamino)-4-morpholinobutyrophenone and then spin-coated at 2000 rpm for 90 s and baked at 50 ^{o}C for 10 min. After exposed under UV light (365 nm, 15 W cm^{-2}) for 6 min through the glass/Cr photomask, PI layers were developed in the solution of solvents: 40 ml of 1-ethyl-2-pyrrolidone, 20 ml of 2-(2-methoxyethoxy) ethanol and 10 ml of ethanol for 90 sec with a subsequent washing in propylene glycol methyl ether acetate for 5 s. After the development layers were hard-baked at 220 °C for 10 min.

6.2.3. Microelectrodes, self-assembly and capsulation

Standard lithography was used to achieve a negatively patterned AZ 5214E photoresist layer on the polymeric layer stack coated substrates. In detail, AZ5214E was firstly spin-coated on substrates with 5000 rpm for 45 s and soft-baked at 90 ^{o}C for 4 min to remove the solvent of photoresist. After exposed under UV light (365 nm, 15 W cm^{-2}) for 0.7 s through the glass/Cr photomask, samples were then hard-baked at 120 ^{o}C for 2 min to enable the exposed area of photoresist chemically stable in the development procedure. Flood exposure for overall samples for 30 s was carried out. Thus, the interdigital pattern appeared in the development procedure and simultaneously undercut structure at the edge was created.

Electron beam evaporation was used to pattern the interdigital current collectors on the PI layer. 10 nm Cr and 50 nm Au were successively deposited at 0.5 Å s^{-1} in the e-beam evaporator (Edwards auto 500 FL 500, England). Finally, a lift-off process was performed in acetone and isopropyl to remove the photoresist and metal layer on its surface. The finger width and gap are 200 μm and 50/70 μm, respectively, as shown in Figure 6.2b and 6.1c.

To easily achieve electrodeposition process on electrodes, samples were firstly fixed on special designed printed circuit boards (PCBs) via VGE-7031 adhesive with subsequent Au-wire bonding for connecting the pads of the device to PCBs outside. The above device was immersed in an aqueous electrolyte containing 10 mM EDOT, 10 mM SDS, and 1 M H_2SO_4, followed by electrodeposition (also called electropolymerization) at a potential of 0.9 V with different time using Platinum wire (a diameter of ≈1 mm, Autolab) and Ag/AgCl (saturated KCl) as counter and reference electrodes, respectively.

The rolling process of planar devices was controlled by selectively etching the sacrificial layer in the solution of 0.5 M potassium diethylenetriaminepentaacetic acid (DTPA) (pH=10) adjusted by potassium hydroxide. After the rolling process completed, the 3D devices were continuously immersed in the etching solution for 2 h to make the 3D architecture stable. Finally, the devices were taken out of the solution and then sealed by 5 M LiCl/ Polyvinyl alcohol (PVA) gel electrolyte which was prepared by mixing 2 g PVA powder and 4.24 g LiCl in 20 mL deionized water. Finally, the gel electrolyte outside the tube was dried in air for two days.

6.3. Results and discussion

6.3.1. On-chip and free-standing sample morphology

For the design of polymeric layer stacks, the hydrogel layer was designed into a trapezoidal shape (Figure 6.2a) so that the area close to the longer edge of the hydrogel layer has a larger strain. A strain gradient along the “Y” direction was formed and the rolling direction (from top to bottom) was well confined. Figure 6.1a also shows that polymeric layer stacks were successfully fabricated according to the homogenous film without defects. Cr/Au interdigital current collectors with 50/70 μm of finger gaps were then patterned on their top.

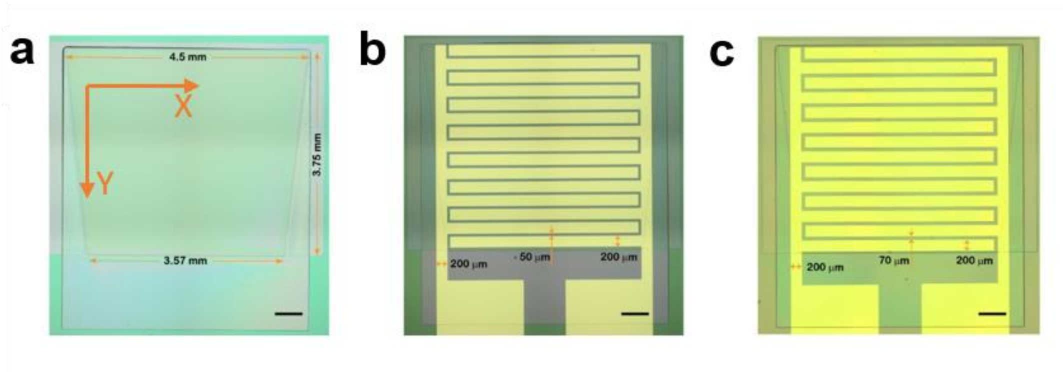

Figure 6.2. a) Optical microscope image of the patterned polymeric layer stack for on-chip tubular device, including sacrificial, hydrogel and PI layers. Scale bar: 500 μm. b,c) Optical microscope images of interdigital Cr/Au current collectors on the polymeric layer stack. Scale bar: 500 μm.

The initial thickness of films and stress distribution determine some of the major structural properties of a tubular device such as curvature radius and fabrication yield. Therefore, PEDOT electrodes with different thicknesses were electrodeposited on polymeric layer stacks by controlling the electrodeposition time (3 min, 10min, and 30 min). The electrodes are denoted by PEDOT-3, PEDOT-10, and PEDOT-30, respectively. As shown in Figure 6.3, the corresponding thickness of the PEDOT electrodes increases from 0.52 μm to 2.91 μm. It is worth noting that PEDOT is horizontally and vertically grown at the same time, being reflected from the decreased electrode gaps. To avoid the contact between electrodes, an electrode gap with 70 μm (Figure 6.2c) is, therefore, designed for the PEDOT-30 device.

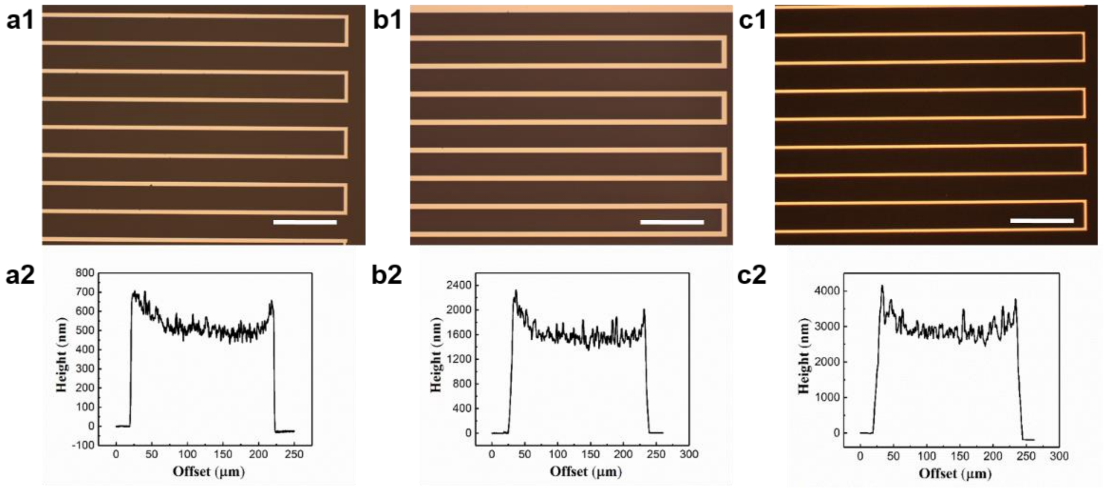

Figure 6.3. Optical microscope images and corresponding section analysis of interdigital PEDOT electrodes with a) PEDOT-3, b) PEDOT-10, c) PEDOT-30. Scale bar: 500 μm.

Planar MSCs can be successfully self-assembled into compact 3D tubular architectures in the DTPA etching solution (Figure 6.4). Even though the interdigital electrodes generate inhomogeneous stress in the layer stack, the yield of tubular devices is > 90 %. In addition, the electrodeposited PEDOT film was deformed along with the rolling process and its stability in solution provides the possibility for the subsequent energy storage of tubular devices. It is also obviously observed that the footprint area of tubular devices is greatly reduced compared to the planar device before rolling. Thus, this tubular MSC possesses improved mass loading of the electrode under a limited footprint area.

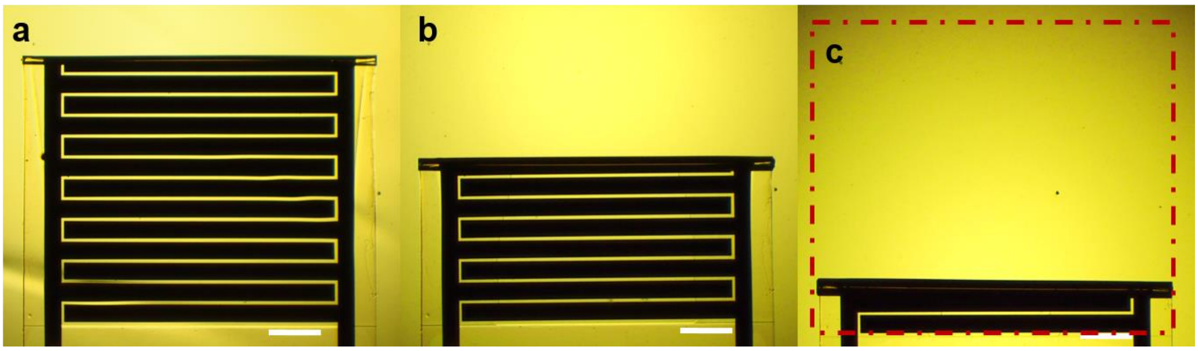

Figure 6.4. Real-time optical microscope images for the rolling process of planar MSC from a) the starting stage, b) intermediate stage, to c) the end stage. Scale bar: 500 μm.

From PEDOT-3 to PEDOT-30, these planar devices were fabricated into tubular architectures with the tube diameter from 205 μm to 351.4 μm (Figure 6.5a). Tube diameter and PEDOT thickness are positively correlated (Figure 6.5b). When the electrodeposition time is increased more than 30 min, 2 μm thickness of polymeric strain layers is not capable of the electrodes rolling, owing to the non-deformable of thick PEDOT. However, it is an efficient way to address this issue by increasing the thickness of polymeric strain layers. Figure 6.5a also shows that their footprint areas are reduced to 0.9 mm^2 (PEDOT-3) and 1.58 mm^2 (PEDOT-30), compared to the footprint area of planar devices (16.88 mm^2).

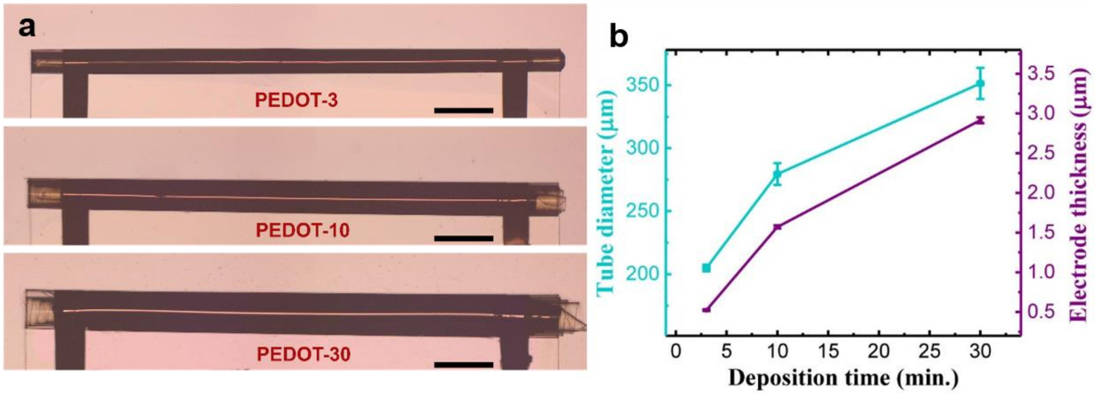

Figure 6.5. a) Optical microscope images of tubular MSCs with PEDOT-3, PEDOT-10, and PEDOT-30. Scale bar: 500 μm. b) The tube diameter and the electrode thickness with respect to electrodeposition time (3 min, 10 min, 30 min).

In Figure 6.6a, the SEM image shows an opening of the tubular structure with multiple windings. The outer part of the tube wall was cut by a focused ion beam (FIB) to reveal the internal structure (Figure 6.6b). This cut shows three outside windings of the “Swiss-roll” architecture, which consists of the thick polymeric bilayer (composed of the hydrogel layer and PI layer; total thickness ca. 3.4 μm), the current collector (bright) and the PEDOT film (thickness ca. 500 nm). Hydrogel and PI layers could not be distinguished in the SEM images because of the low contrast difference without heavy metal staining. In addition, the tubular devices maintained their shape when they were taken out of the etching solution. The remaining etching solution (outside and inside of the hydrogel layers) stayed inside the tubular structure providing ionic conductivity of 85.7 mS cm^{-1} and therefore contributed excellently to the tubular MSC operation. In the gap between different windings, a certain amount of dried salt was found on the surface of the hydrogel layer, indicating that the etching solution was filled into the tube efficiently.

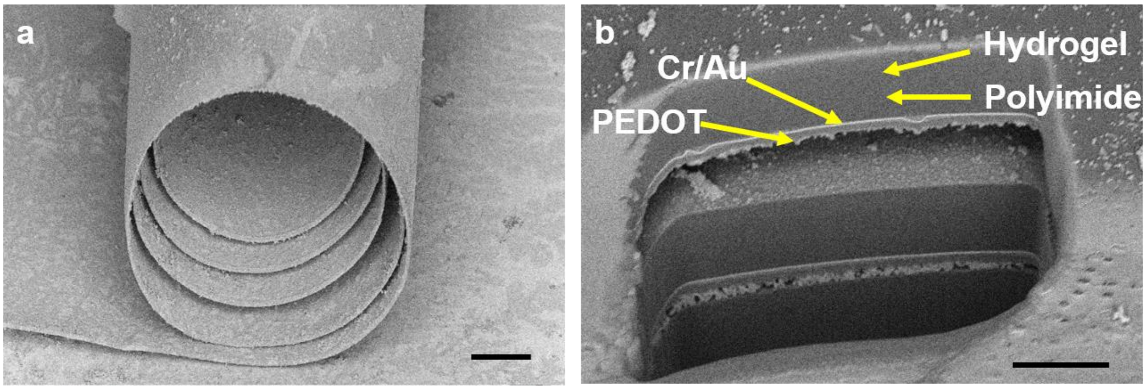

Figure 6.6. a) SEM image of a tube opening with multiple windings. Scale bar: 50 μm. b) Cross-section of the upper wall of a tube prepared by FIB-cutting. Scale bar: 5 μm.

6.3.2. Electrochemical characterization of tubular MSCs

Tubular MSC with PEDOT-3 was removed from the etching solution after self-assembly. Its electrochemical performance was then investigated using CV at 0.1 V s^{-1} in a potential window of 0.8 V, as shown in Figure 6.7. In the beginning, a symmetric and closed CV curve with a certain area is present, demonstrating that the etching solution could be used as the electrolyte. After 15 min and 30 min of operation, the device appeared the phenomenon of solution evaporation, reflecting from unstable CV curve shapes. Tubular MSC was then recovered to the original performance again after adding the etching solution. This measurement illustrates that the etching solution as the electrolyte is not enough to support the long-term charge/discharge process owing to its evaporation, although it has a good effect on the ionic conductivity at the beginning.

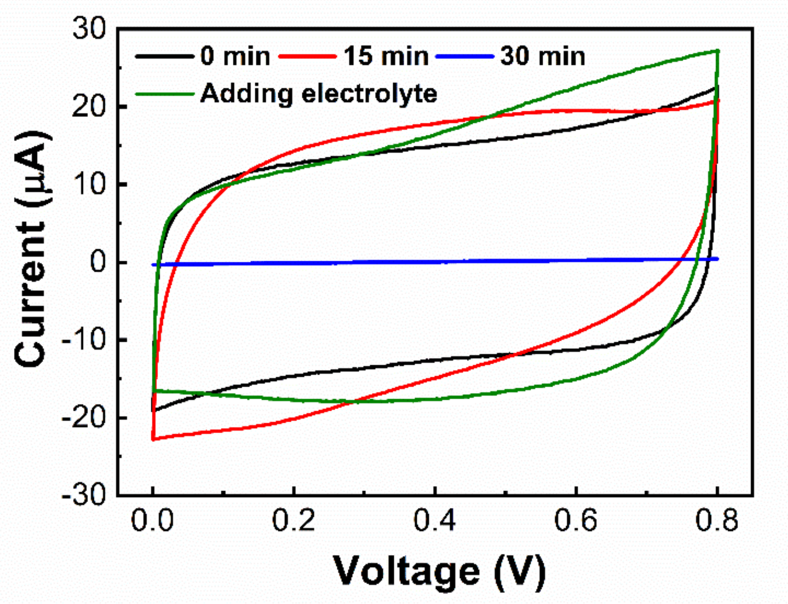

Figure 6.7. CV curves of 3D tubular MSC with PEDOT-3 over time after taken out from etching solution. Scan rate: 0.1 V s^{-1}.

PVA/LiCl gel was further used to seal the tubular structure. Owing to the existed etching solution in the tube, ions in the external gel can easily diffuse to the electrode surface, and instead, the ions and water in etching solution cannot be easily evaporated. The reason should be that PVA/LiCl is a gel electrolyte with a moisturizing property better than for pure LiCl aqueous solution. Although there is an issue of water evaporation, PVA can store most of the water for the long term (*e.g.* one month) and provide a stable ionic environment.[209] To verify it, long-term (up to 30 days) capacitance retention of a tubular MSC was investigated. The electrochemical measurement was performed every five days. As shown in Figure 6.8, the CV characteristics spanning over 30 days of a tubular MSC are almost identical, indicating the good electrolyte performance of PVA/LiCl gel for long-term operation. The electrochemical performance maintains 99 % of capacitance retention after 30 days. In addition, the rectangular and symmetric nature of curves in Figure 6.8a illustrates that tubular MSC possesses ideal capacitor behavior.

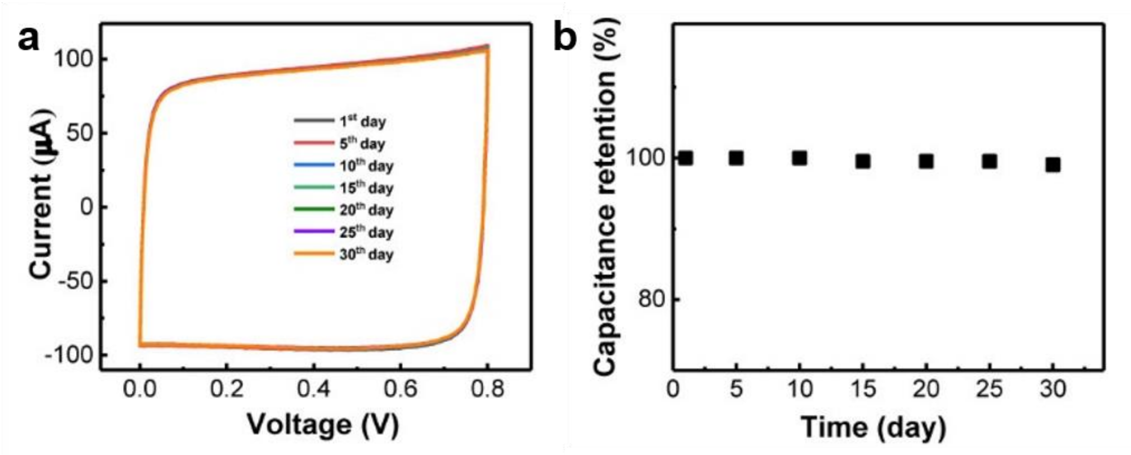

Figure 6.8. a) CV curves of a typical tubular MSC at scan rates of 0.1 V s^{-1} for one month. b) Capacitance retention *vs.* time.

It is worth noting that the hydrogel layer after rolling mechanically touches the PEDOT electrode (Figure 6.9a). This special configuration supported by hydrogel provides a space for Li^+ accommodation and the ion transport between electrode fingers in the tube. The electrochemical performance of tubular MSCs (PEDOT-3, 10 and 30) with gel encapsulation was then investigated using CV technique over a wide range of scan rates from 0.01 to 10 V s^{-1} in a potential window of 0.8 V, as shown in Figure 6.9b-6.9e. At a slow scan rate, the surface of PEDOT can fully react with the electrolyte. CV curves of tubular MSCs at 0.01 Vs^{-1}, indicates that the highly symmetric and rectangular shape of devices without reaction peak is well maintained. Such an ideal electrochemical performance can be attributed to the porous nanostructures of curled PEDOT and efficient ion transport between electrodes in tubes. At scan rates larger than 1 V s^{-1}, the CV curve becomes skewed and the voltammogram edges round off, resulting in a declined capacitance (Figure 6.9e). As abovementioned content, the capacitance of the MSC is generally related to its scan rate, current window as well as the potential window. Therefore, the increasing area of closed curves from PEDOT-3 to PEDOT-30, suggests that their capacitance positively correlated to the loading of the PEDOT active material.

Figure 6.10a presents the galvanostatic charge-discharge (GCD) curves of tubular MSCs in a potential range of 0-0.8 V at a current density of 0.5 mA cm^{-2}. Those highly symmetric and linear shapes indicate their high reversibility between the charge and discharge processes. In addition, the internal resistance (IR) drop at the beginning of the discharge curves is not observed, suggesting that they exhibit exhibited a low equivalent series resistance. GCD measurements were also performed to investigate the feasibility of PEDOT-30 tubular MSC at broad current densities range, are shown in Figure 6.10b. From 0.5 mA cm^{-2} to 5 mA cm^{-2}, the GCD curves show that it still can maintain excellent charge-discharge performance in spite of the high PEDOT loading.

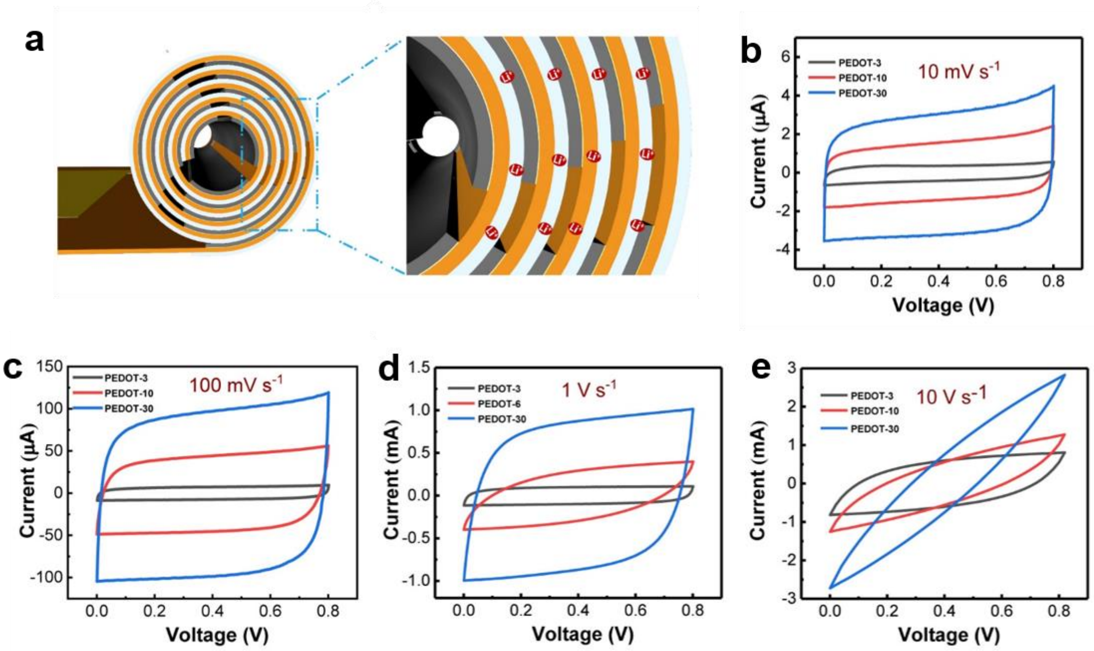

Figure 6.9. a) Schematic of the cross-section of tubular MSCs with Li ion transport between electrodes supported by the hydrogel. b-e) CV curves of three tubular MSCs (PEDOT-3, 10, 30) over a scan rate range from 10 mV s^{-1} to 10000 mV s^{-1}.

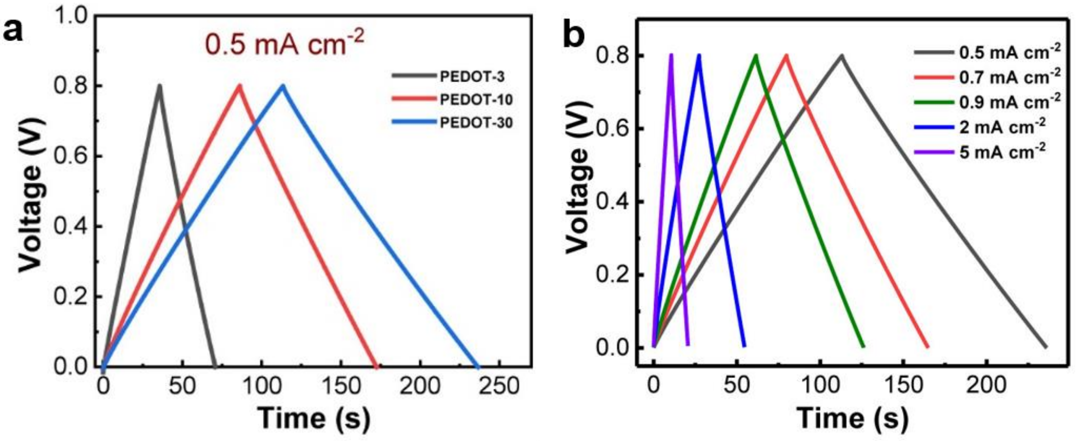

Figure 6.10. a) GCD curves of three tubular MSCs at a current density of 0.5 mA cm^{-2}. b) GCD curves of tubular MSC with PEDOT-30 at different current densities.

Based on the GCD curves from PEDOT-3 to PEDOT-30, the areal capacitances of tubular MSCs showed higher areal capacitance than the planar device (Figure 6.11a). The PEDOT-30 tubular MSC possesses the highest areal capacitance among all of the fabricated devices reaching 82.5 mF cm^{-2} at a current density of 0.3 mA cm^{-2}. This is because the rolling technique can greatly reduce the footprint of MSC. For instance, the footprint area of the PEDOT-30 tubular MSC is 14.6 times smaller than that of its planar counterpart, and the resultant areal capacitance is 900 % times higher than the previous record value for PEDOT-based MSCs.[210] Figure 6.11a also shows the dependency of specific capacitance on current densities. The observed decrease in specific capacitance with increasing current densities can be explained by the limited transfer of ions to the PEDOT surface.

Apart from the footprint area, the mass of PEDOT and volume of MSC are the other two critical parameters to evaluate the electrochemical performance of tubular MSC. Especially due to the small space available for practical miniaturization, the volume of tubular MSC should be considered. As shown in Figure 6.11b and Figure 6.11c, the gravimetric and volumetric capacitances of PEDOT-30 tubular MSC are presented. The tubular MSC exhibits a gravimetric capacitance of 17.7 F g^{-1} with a density of 2.2 g cm^{-3} at 64 mA g^{-1} and 2.7 F cm^{-3} of volumetric capacitance (28.5 F cm^{-3} of planar MSC) at 5 μA. The volumetric performance of tubular MSCs in this work is lower than the values of planar MSCs before rolling. The reason is that the hollow part of the tubular structures formed after rolling increases the volume of 3D structures, decreasing the calculated volumetric performance. In future studies, by further improving our methods, with more winding numbers and thicker layers of high-performance active materials, both the areal and volumetric performance of tubular MSCs are expected to be much improved, simultaneously maintaining the limited footprint areas. The overall capacitance performance of the planar MSC and tubular MSC was also studied (Figure 6.11d). Compared to the planar MSC (with pure PVA/LiCl as electrolyte), the capacitance of the tubular MSC decreased from 1.2 mF to 0.95

mF at 50 μA, owing to the influence of the etching solution on the PVA/LiCl electrolyte. Despite this, tubular MSC still exhibits higher capacitance as compared to planar devices. Overall, the measured electrochemical performance indicates that rolled-up nanotechnology based on strained polymeric layers can provide an advanced and reliable approach to fabricate compact tubular MSCs and micro-batteries.

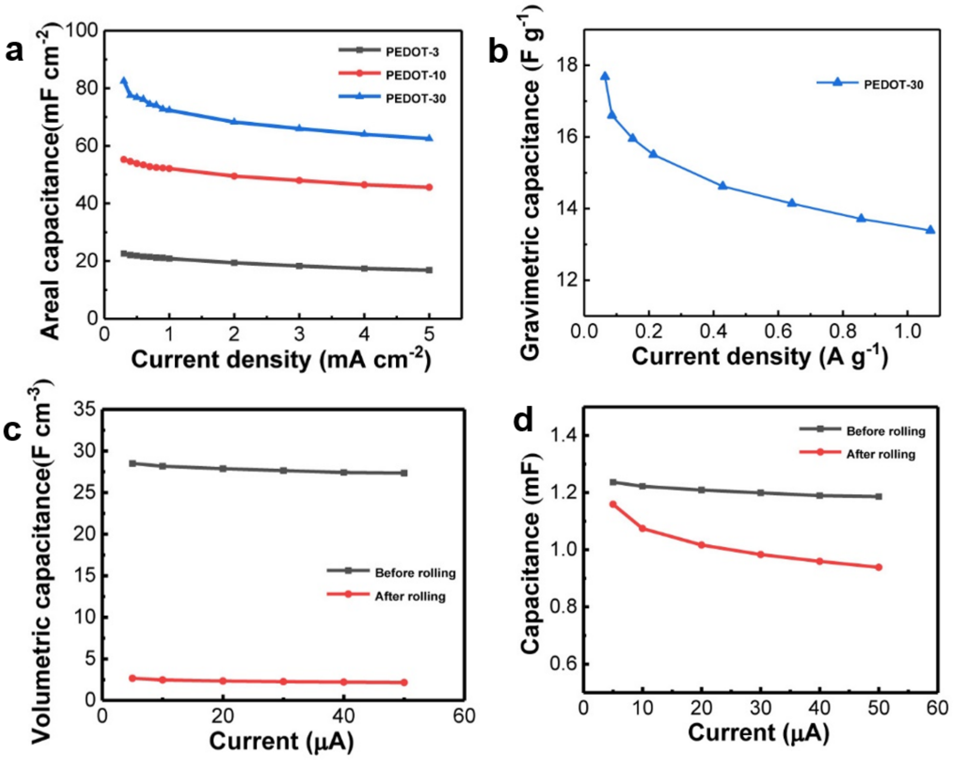

Figure 6.11. a) Areal capacitance comparison of tubular MSCs as a function of various current densities. b) Gravimetric capacitance of PEDOT-30 tubular MSC as a function of various current densities. c) Volumetric capacitance comparison of MSCs before rolling and after rolling. d) Capacitance comparison of MSC before and after rolling.

The electrochemical impedance spectra (EIS) of tubular MSCs were further analyzed (Figure 6.12a). Nyquist plots over a frequency range from 0.01 Hz to 100 kHz exhibit vertical character with respect to the –Z'' axis at low frequencies, which reflects a pronounced capacitive behavior. The zoom-in view of the impedance spectra (inset of Figure 6.12a) at high frequencies shows a small inner resistance which can be attributed to the good inner electrical conductivity of the tubular devices.

As the performance per footprint area is key to benchmark MSCs in miniaturized electronics, a Ragone plot is presented to compare the areal energy density and power density of PEDOT-30 tubular MSC with representative MSCs and micro-batteries from earlier reports. As shown in Figure 6.12c, the performance of this tubular device shows high energy density and comparable power density to other MSCs including graphene-carbon nanotube (CNT) carpets,[211] polyaniline (PANI),[212] PEDOT,[210] carbide-derived carbons (CDC, with H_2SO_4 electrolyte),[213] RuO_2[23] and MnO_2.[214] It can also be comparable to the state-of-the-art micro-batteries composed of Ni-Zn and carbon-dodecylbenzenesulfonate doped polypyrrole (PPYDBS).[215] In addition, such a tubular MSC device exhibits much higher areal capacitance under a small footprint area than most reported works using carbon materials and conducting polymers (Figure 6.12d),[39,57,180,210,216–221] indicating that rolled-up technology is a powerful tool to self-assemble thin films into tubular energy storage device with a limited footprint area.

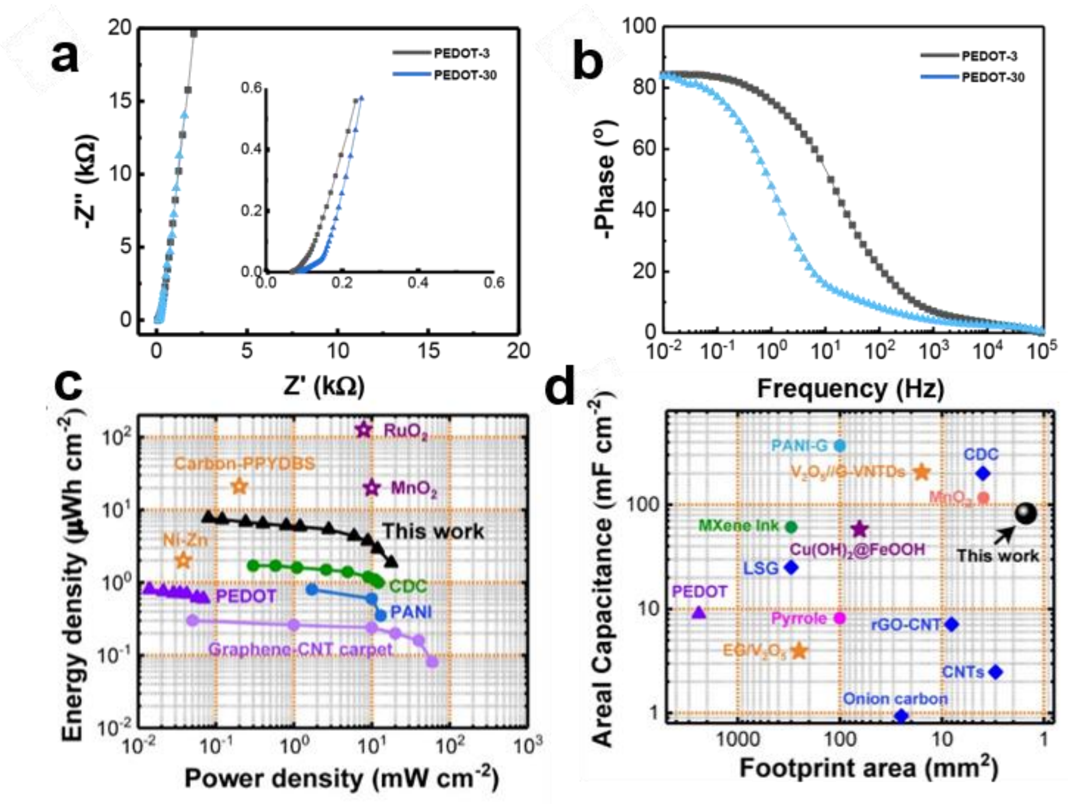

Figure 6.12. a) Electrochemical impedance spectra of three typical tubular MSCs from 0.01 Hz to 10^5 Hz. b) Impedance phase angle *vs.* frequency for PEDOT-3 and PEDOT-30. c) Areal-normalized Ragone plots comparing PEDOT-

30 tubular MSC with MSCs using graphene-CNT carpets, PEDOT, PANI, CDC and state-of-the-art micro-batteries using Ni-Zn, carbon-PPYDBS. d) Comparison of the areal capacitance and the footprint area of tubular MSCs with reported interdigital MSCs.

The capacitance retention was evaluated by performing GCD measurements over 5000 cycles (Figure 6.13a and Figure 6.13b). A high capacitance retention of more than 94 % after 5000 cycles is obtained for all tubular MSCs (PEDOT-3: 96.6 %; PEDOT-10: 95.8 %; PEDOT-30: 94.1 %). The inset of Figure 2H shows the first and the last five GCD curves of the PEDOT-30 tubular MSC. The symmetric curves and the ratio of discharge and charge time confirm that the tubular MSCs still possess high Coulombic efficiency and reversibility after 5000 cycles (Figure 6.13c). For comparison, the planar PEDOT-30 tubular MSC had capacitance retention of 88 %, which is similar to previous reports.[27,186] This enhanced cycling stability may originate from several features inherent to the tubular structure: 1) efficient strain accommodation of the PEDOT layers,[65,157] 2) robust fixation of multiple windings on the PEDOT films, and 3) efficient ion transport in confined channels.

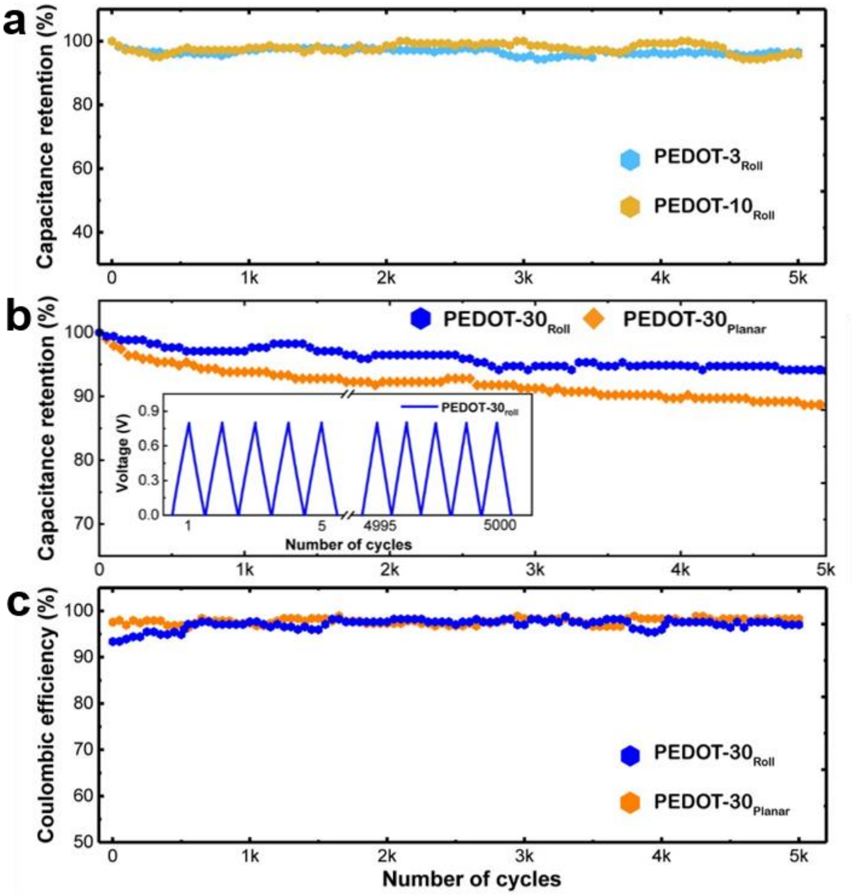

Figure 6.13. a, b) Capacitance retention of tubular devices (PEDOT-3, -10 and -30) over 5000 cycles of GCD measurement. The inset in b) shows the first and last five GCD curves of the 5000 cycles, and a cross-sectional diagram for tubular MSC. c) Coulombic efficiency of tubular and planar PEDOT-30 devices over 5000 cycles of GCD measurement.

6.3.3. Self-protection function of tubular structures

Polymeric layer stacks containing hydrogel and PI layers are intrinsically flexible and robust. Therefore, the curled polymeric framework wrapping up the interdigital electrodes could lead to efficient self-protection against external mechanical forces. Such a property is critical when pushing MSCs towards practical mass production and application. For instance, automated pick-and-place processes for device and circuit integration enforce severe mechanical compression on individual MSCs. Likewise, MSCs for maintenance-free devices and wearable electronics might be compressed and folded during operational deployment. Still, MSCs are expected to maintain proper performance under all circumstances. In the following evaluation of tubular MSCs against mechanical compression, a hard test head with a diameter of 200 μm was used to compress the tube structure (Figure 6.14a). Simultaneously, GCD measurements were performed to record the real-time influence of the compression pressure on the device. Figure 6.14b shows an optical image of the PEDOT-3 device before and after different compression pressures (31.8 kPa ~ 31.8 MPa). In this process, compression cycles were repetitively applied on three areas of the tube's top surface: Close to the left opening (Tube$_{L}$), right opening (Tube$_{R}$) and center (Tube$_{C}$). The compression cycles were applied with a sequence of Tube$_{L}$-Tube$_{R}$-Tube$_{C}$. Gradually increasing compression pressure on the tube is generally accompanied by the larger deformation, thus implying that a higher risk to the damage of devices may occur. The real-time GCD measurement in Figure 6.14c and 5.14d indicates that the capacitance retention of the device stays over 90 % before 31.8 MPa of compression pressure is reached. In the operation, the center part of the tube possesses better tolerance than the left and right parts.

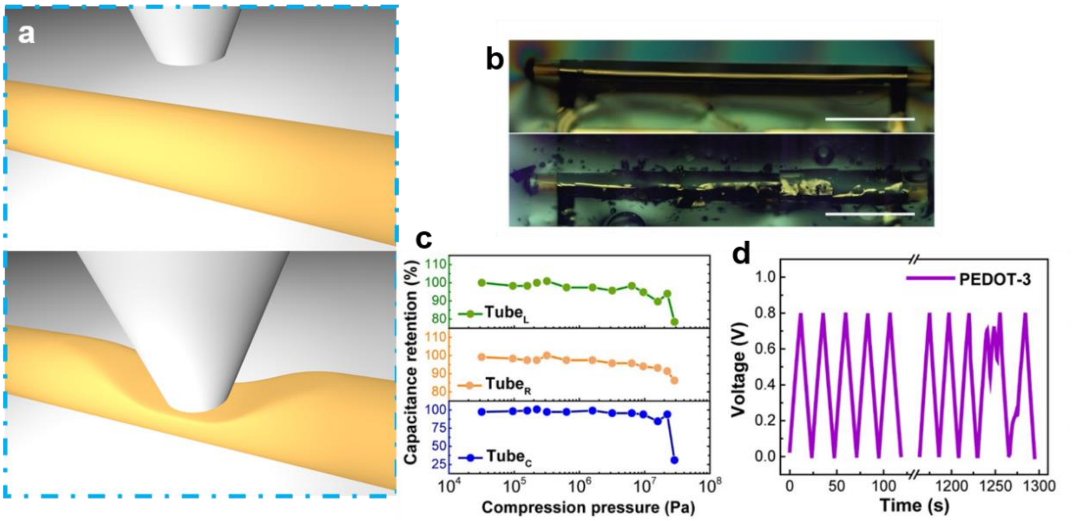

Figure 6.14. a) Schematic illustration of the compressive deformation of the tubular device. b) Optical microscopy images of PEDOT-3 MSC before and after compression, corresponding to the c) capacitance retention curves and d) GCD curves at 9 μA.

Transient degradation and prompt recovery of the *in-operando* device performance were also studied. The optical images in Figure 6.15a and 5.15b reveal that the tubular devices (PEDOT-3, PEDOT-30) maintain their structural integrity after compressing 90 times at 31.8 kPa. Excellent capacitance recovery for both devices in the GCD measurements is recorded several times (Figure 6.15c). For instance, for the PEDOT-30, the capacitance retention decayed to about 96% in the 12th cycle and recovered back to almost 100% afterwards. The PEDOT-3 device exhibited superior compressive stability with the capacitance retention of 98.5 %, compared to the PEDOT-30 device with 84.2 % of capacitance retention. This demonstrates that the tubular device with the low PEDOT load has a better capability to self-protect against compression. GCD curves show that the devices maintained excellent charge-discharge characteristics under repeated compressions at lower pressure (Figure 6.15d).

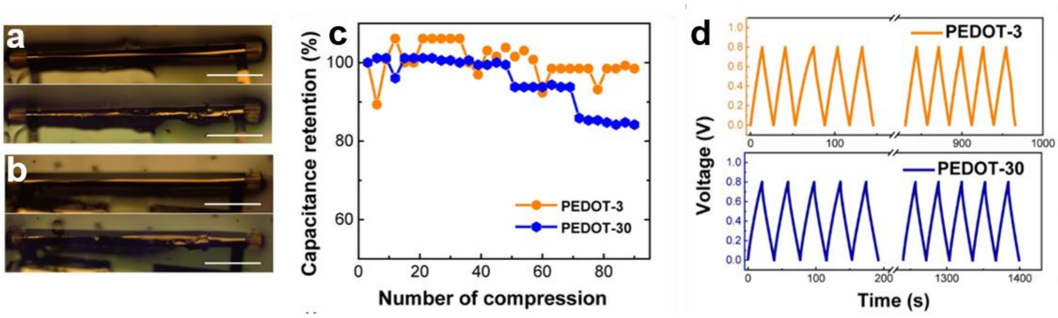

Figure 6.15. a,b) Optical microscopy images of MSCs (PEDOT-3, PEDO-30) over 90 compression cycles at 31.8 kPa, corresponding to the c) capacitance retention curves and d) GCD curves.

For comparison, a higher-pressure compression of 31.8 MPa was applied to the PEDOT-30 device for 66 times, resulting in a much rougher tube surface than that of the PEDOT-3 device (Figure 6.16a). Although the large compression pressure caused substantial deformation and damage to the device topography, a high capacitance retention of 71.9 % for the device was still obtained (Figure 6.16b and 5.16c).

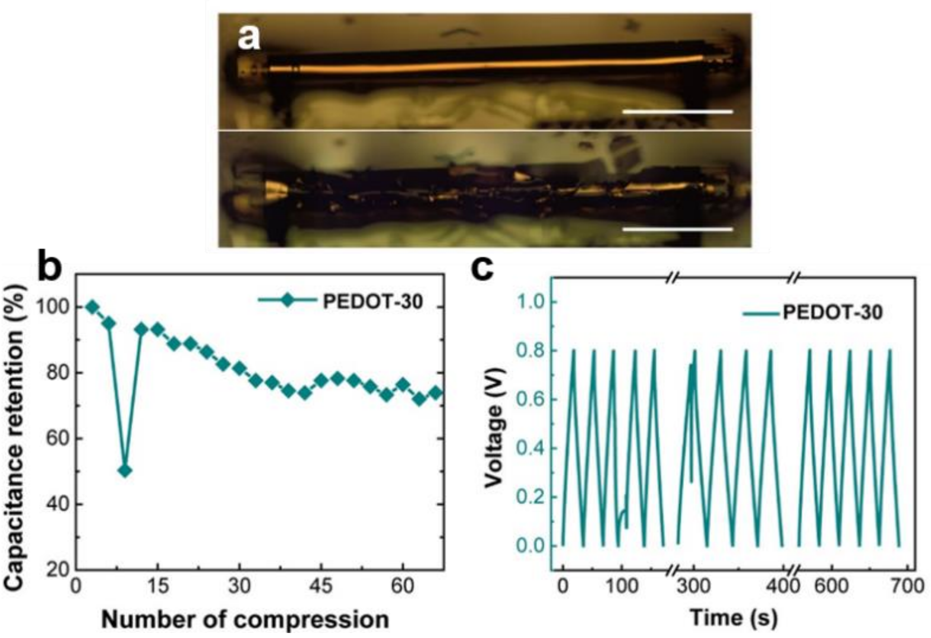

Figure 6.16. a) Optical microscopy images of PEDOT-30 MSC over 66 compression cycles at 31.8 MPa, corresponding to the (b) capacitance retention curves and (c) GCD curves at 30 μA.

In actual operation, the mechanical compressive pressure experienced by the tubular MSC may be continuous and dynamic. Therefore, the capacitance retention of the device under continuous compression was measured on the tube as shown in Figure 6.17. Under the different time of compression (3 s, 1 min, 3 min, 6 min), tubular MSC could not be charged and discharged. However, the device still maintained excellent capacitance retention of 99.5 % after the release of pressure. The disturbed charge-discharge processes immediately recover after the transient decay during operation. The self-protective properties render the tubular MSCs suitable for modern automated mechanical operation lines and durable for practical operation scenarios.

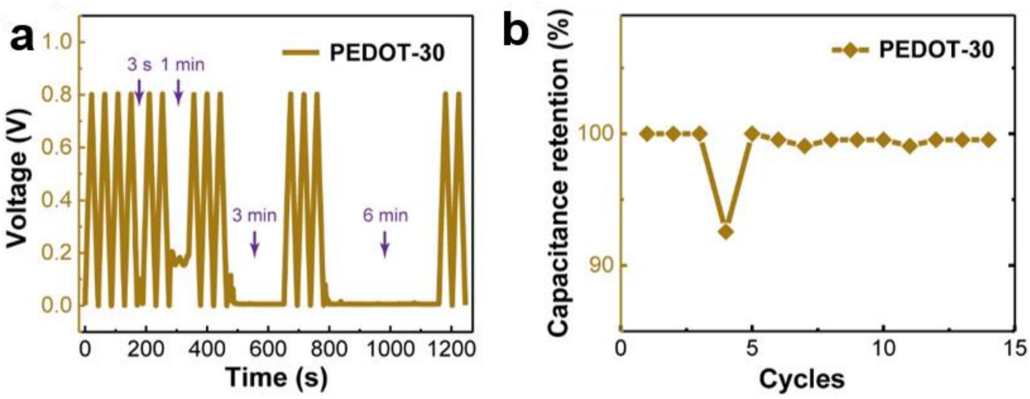

Figure 6.17. GCD curves and capacitance retention curve of PEDOT-30 tubular MSC after applying continuous compression with different time (3 s, 1 min, 3 min, 6 min) at 30 μA.

6.3.4. Assembly of tubular structures in series/parallel

Direct fabrication of MSCs on microelectronic circuits has remained a persistent challenge in MSCs integration. For instance, for MSCs containing electrode materials which are obtained by electrodeposition, the solution environment can easily harm other components on chips. Free-standing MSCs provide a feasible way to achieve integration of MSCs on an electronic chip through direct transferring. Thus, to fabricate a free-standing 3D tubular MSC, the whole device structures should be detachable from substrates. Different from the fabrication method of on-chip tubular MSCs introduced above, the sacrificial layer was firstly spin-coated without patterning. The PI layer with the Cr/Au contact pads can be detached from the substrate together with the rolled-up tube by etching the sacrificial layer completely. Therefore, detached tubular MSCs is possible to be transferred to the target substrates. As shown in Figure 6.18a-5.18c, this transferring process was carried out through simple "pick-and-place" using a tweezer, owing to the flexibility and robustness of the PI layer. The free-standing tubular MSCs detached from the chip substrates in etching solution are conveniently transferred onto flexible paper substrate, and still, maintain their geometries after transferring. As illustrated in Figure 6.18d, a high density of tubular MSC array on paper substrate was further demonstrated by this technique. This can greatly improve the working efficiency of on-chip electronics by applying in parallel the self-assembly fabrication.

For demonstration, four single tubular MSCs were assembled in parallel on paper substrates improving their specific voltage and capacitance (Figure 6.19a). Comparing the CV measurements at 100 mV s^{-1}, the enclosed area of the symmetrical curve of four parallel-connected devices is significantly increased (Figure 6.19b). GCD curves in Figure 6.19c demonstrate that the devices connected in parallel have a four-fold higher capacitance than a single device. The Nyquist plots of both devices in Figure 6.19d demonstrate their excellent capacitor behavior and reduced inner resistance after device assembly.

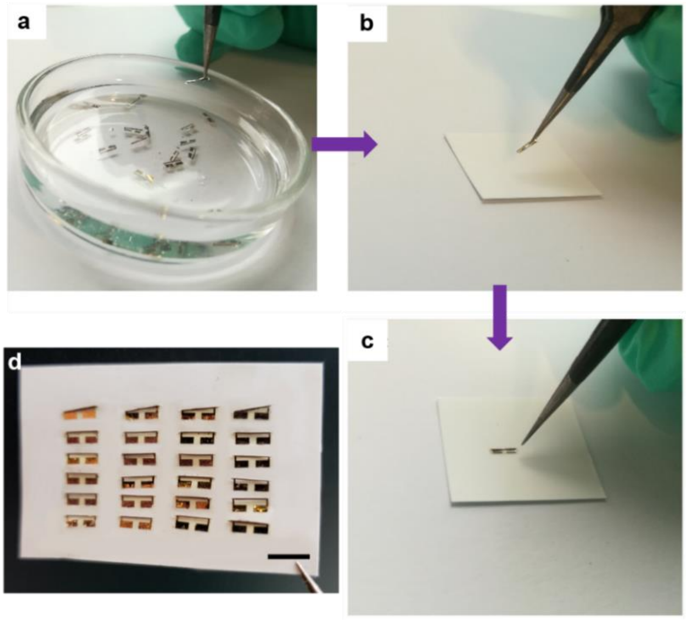

Figure 6.18. a-c) The transfer process of free-standing tubular MSCs from solution to paper using "pick-and-place" method by a tweezer. d) Digital photograph of tubular MSC array (4×6) on paper substrate. Scale bar: 10 mm.

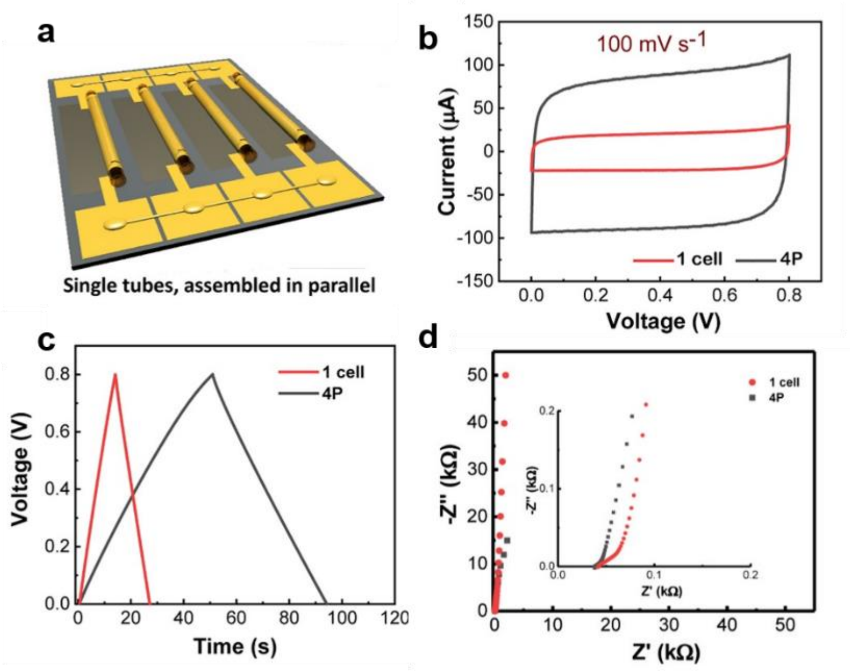

Figure 6.19. Single-tube type MSCs connected in parallel: a) Schematic illustration; b,c,d) CV, GCD and EIS curves of four tubular MSCs connected in parallel and single MSCs.

Different to single tubular devices, four dual-tube type devices connected in series were designed to improve the voltage output (Figure 6.20a). The CV and

GCD curves exhibit a controllable and stable voltage window from 0.8 V to 3.2 V (Figure 6.20b and 6.20c). As shown in the Nyquist plots (Figure 6.20d), this connected device array also has higher inner resistance and capacitance than the single device. In this way, the operation voltage can be increased to drive electronic circuitry. For instance, these four dual-tube devices connected in series can power a commercial timer with a starting voltage of 1.5 V and a blue LED with a starting voltage of 1.9 V (Figure 6.20e and 6.20f). The free-standing tubular MSCs did not show a decline in performance after the transfer process, thus enabling them to be promising candidates for practical integration and applications.

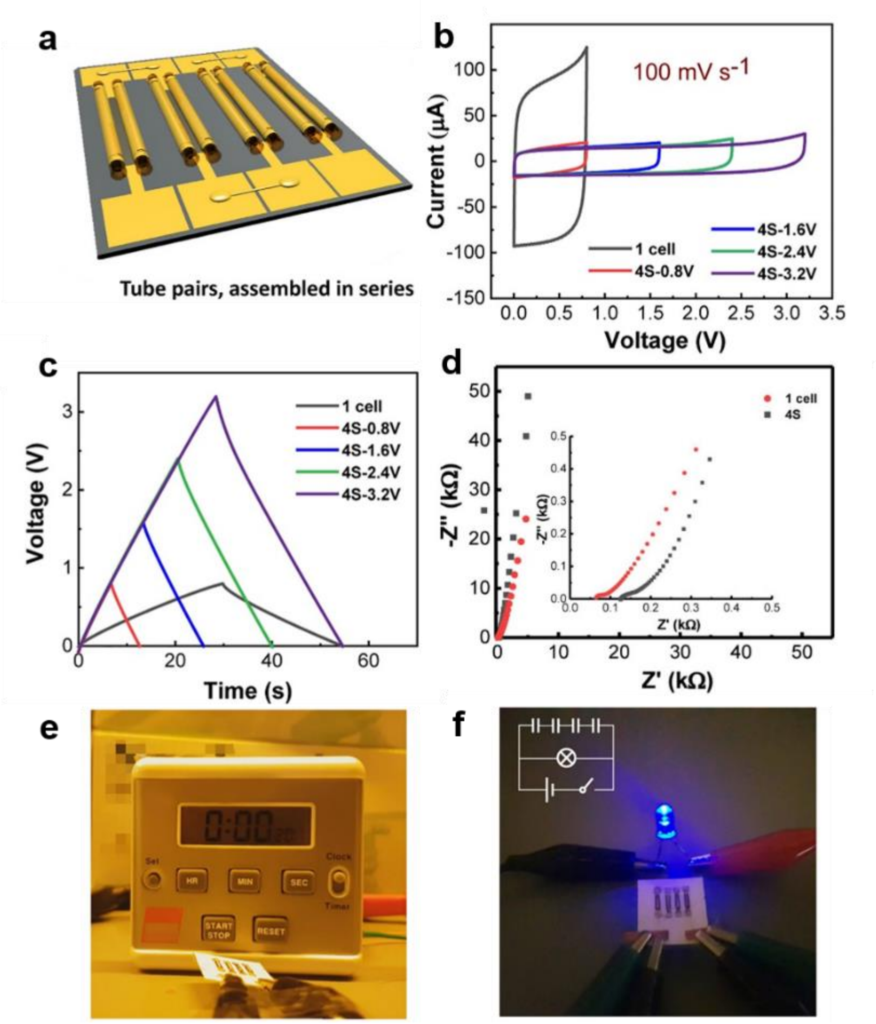

Figure 6.20. Dual-tube type MSCs connected in series: a) Schematic illustration; b,c,d) CV, GCD and EIS curves of four dual-tube type MSCs

connected in series. e,f) Photographs of MSCs connected in series powering a timer and an LED.

Besides, the series and parallel of tubular MSCs resulted in an additional increase in footprint area because of the gaps between devices. Despite this, such tubular MSCs connected in series and parallel still demonstrated their merits of saving footprint area compared to planar devices (Figure 6.21a and 6.21b). In the future, the ultra-long rolling and series in single tube can be designed to further save the footprint area. Self-discharge measurement for tubular MSCs connected in series are presented in Figure 6.21c and 6.21d, showing ~64 % voltage retention for one single tubular MSC within the first half hour and ~51.4 % retention of four tubular MSCs over a period of 1 h.

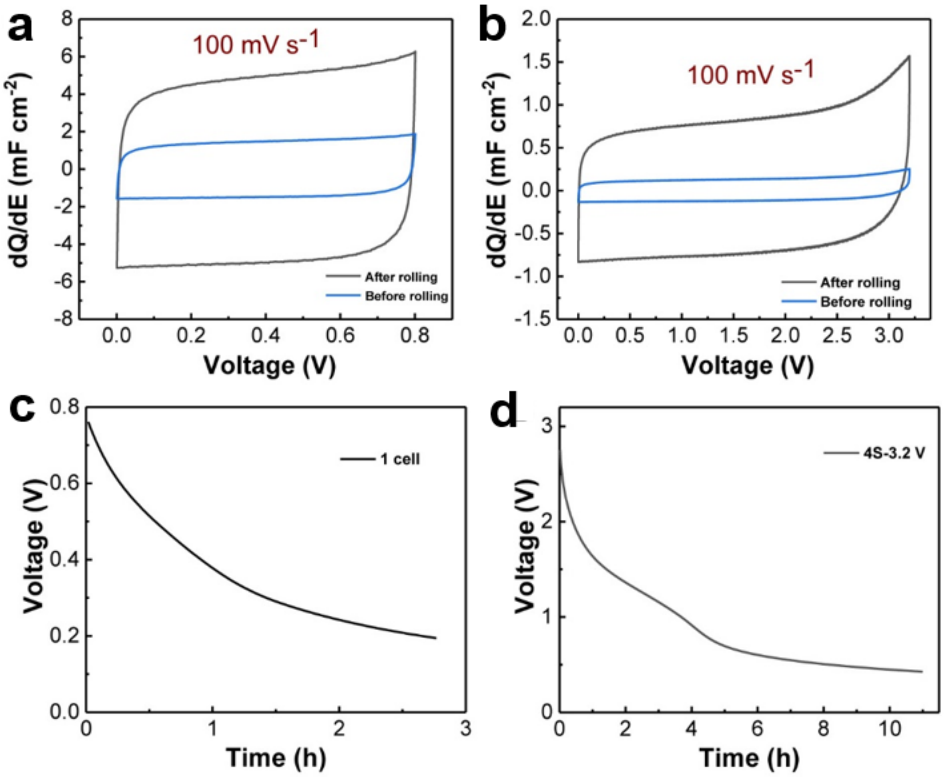

Figure 6.21. Areal CV curves of tubular MSCs connected in parallel a) and b) series, compared to planar devices. c,d) Self-discharge measurement for single device and four devices connected in series.

6.4. Conclusion

In summary, on-chip and free-standing 3D tubular MSCs are successfully designed and fabricated by employing shapeable material technologies that are fully compliant with modern microelectronics industry routines. The planar MSCs consisting of PEDOT electrodes are rolled up into “Swiss-roll” architectures in a controllable self-assembly process, which is challenging to achieve at the microscale by other techniques. Our results show that the rolling process can effectively reduce the footprint area of the original planar device, greatly improving the areal specific capacitance of PEDOT-based tubular MSCs (82.5 mF cm^{-2} at 0.3 mA cm^{-2}, which is nine times higher than state-of-the-art) and power density. Moreover, this tubular architecture enables the tubular MSCs to exhibit an improved capacitance retention up to 96.6 % over 5000 cycles and excellent self-protection against external mechanical compression. Free-standing devices connected in parallel and in series show improved energy density and voltage output, which provides a promising route to integrate 3D tubular MSCs on diverse circuit boards. In summary, our work demonstrates a new powerful strategy to create tubular MSCs with high performance and small footprint area, creating an intriguing counterpart to conventional cylinder-shape energy storage devices at the microscale. The integration strategy developed in this work efficiently bridges diverse newly developed high-performance materials to create microscale “Swiss-roll” energy storage device.

Chapter 7. Tubular nanomembranes for MSCs

7.1. Introduction

MSCs with high energy density and power density can power more types of electronic components.[222] On the other hand, the key metrics of MSCs rely on the integrated areal performance due to the limited space in practical microelectronic circuits. Therefore, loading more active materials through constructing 3D electrode architectures can effectively increase the areal performance in a limited footprint area. To date, the MSCs with 3D architectures mainly contain vertical structures, including porous structures[223], ordered microstructures (pillars[224], trenches[225], walls[226]) and ordered nanostructures (nanowire[227], nanotube[228], nanowall[229]). Owing to the high aspect ratio, superior performances which are much higher than those of common in-plane MSCs can be obtained by these 3D architectures.

In the last chapter, the patterned hydrogel and PI as strain layers have been successfully fabricated to assemble interdigital MSCs into 3D tubular architectures. This self-assembly method endows tubular MSCs with novel features, such as small footprint area, mechanical self-protection, as well as improved cycling performance. It also demonstrates that such tubular MSC possesses higher areal energy density and power density than that of planar type MSC. This provides a promising route to integrate the well-fabricated 3D MSCs on diverse circuit boards and opens up more reliable routes for integrating 3D MSCs and micro-batteries.

It is worth noting that, the inorganic nanomembrane is another type of strain layer which is usually utilized to fabricate tubular devices and Li-ion battery materials.[160,230] These rolled-up micro/nanostructures have also shown the appealing mechanical and electrical properties, such as small footprint, high active surface area, and excellent structure stability against morphological volume expansion.[8] In this regard, combining tubular inorganic nanomembrane with interdigital MSCs should be another promising strategy to construct ultra-small 3D tubular MSCs with a small footprint area.

In this chapter, two types of inorganic strained nanomembranes were studied to force the roll-up of interdigital MSCs. The Al_2O_3/Ti/Cr/Al_2O_3 strained nanomembrane on top of the sacrificial layer was first explored using the photolithography technique. The results show that interdigital current collectors can only be rolled into a “Swiss-roll” architecture with a small yield. To solve this issue, an Al_2O_3/Ni/Cr/Al_2O_3 nanomembrane with a high aspect ratio was further designed and fabricated. With the assist of a magnetic field, such nanomembrane loaded with MnO_2 active material was successfully assembled into 3D MSCs.

7.2. Self-assembly of Al_2O_3/Ti/Cr/Al_2O_3 strained nanomembranes

7.2.1. Fabrication method

The fabrication steps for processing inorganic nanomembrane-based tubular MSCs are schematically illustrated in Figure 7.1. All the patterning of the nanomembrane was performed using AZ5214E by standard photolithography in the cleaning room. The lift-off of all patterns was carried out in acetone and isopropanol.

Firstly, the 20 nm Ge sacrificial layer with a rate of 0.5 Å s^{-1} was deposited by the electron-beam evaporator on top of a Si/SiO_2 substrate with patterned photoresist. After deposition, Ge underwent a 2 h oxidation procedure in an oven at 80 °C under oxygen atmosphere, in order to form GeO_x which is soluble in water. 7 nm Al_2O_3 layer was then grown by ALD (Cambridge Nanotech Savannah100) at 200 °C using TMA and water as precursors. All precursors were high purity and purchased from Sigma-Aldrich. The strained nanomembrane consisting of Ti and Cr was deposited with precise rates of 1 Å s^{-1} and 3 Å s^{-1} below 1×10^{-6} mbar. The second 10 nm Al_2O_3 was deposited on Ti/Cr again. Thus, two layers of dense Al_2O_3 can effectively prevent the MSC from short-circuit after rolling up. Similar to the design of MSC in Chapter 5 and Chapter 6, interdigital current collectors with 5 nm Cr/15 nm Au were finally deposited and patterned.

The next fabrication step consisted of opening a trench using ARP 3510 photoresist and etching Al_2O_3 by a 3.3% HF solution. The sample was immersed into deionized H_2O for four hours to release the nanomembrane in H_2O_2 (30%). After 2 min, the sample was transferred to a solution of H_2O at 50 ^{o}C.

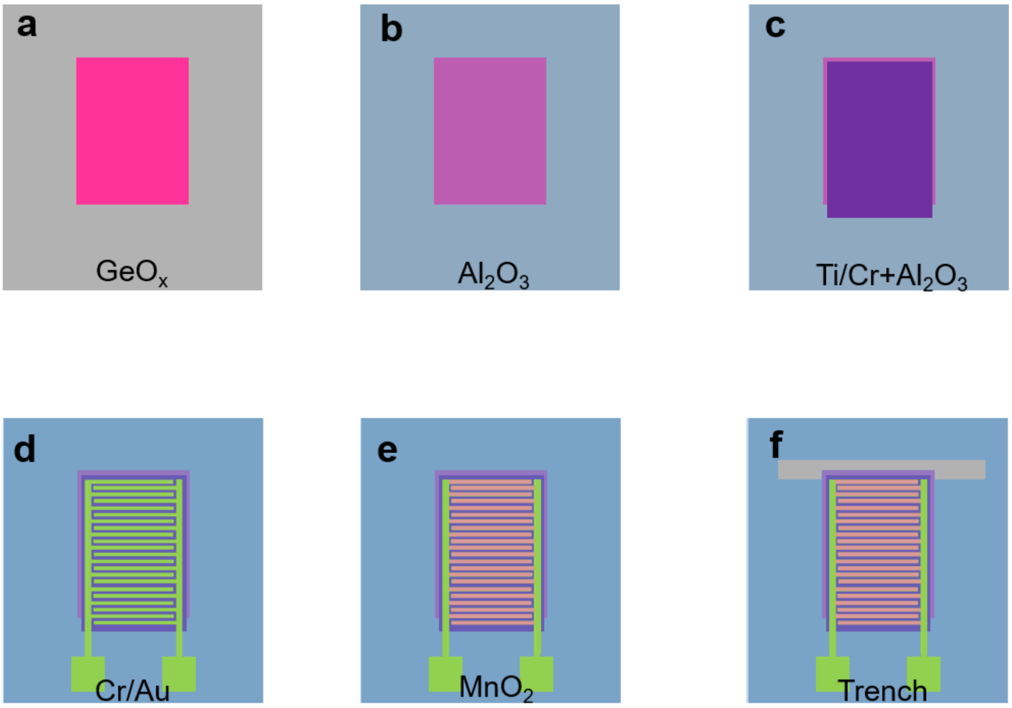

Figure 7.1. A schematic depicting procedures for the self-assembly of tubular MSCs: a) patterning and deposition of Ge as sacrificial layer, b,c) Al_2O_3 and Ti/Cr deposition, d) Cr/Au current collectors, e) MnO_2 deposition by electron beam evaporator or electrodeposition method, f) the trench opening by HF solution.

7.2.2. Results and discussion

The Al_2O_3/Ti/Cr/Al_2O_3 nanomembrane is a powerfully strained multilayer stack that can force the self-assembly of planar devices (*e.g.* capacitor) into "Swiss-roll" architectures.[137,231] In this work, the rolling process of such nanomembrane takes place in neutral aqueous media, accompanying the etching of GeO$_x$ sacrificial layer. The slow dissolution rate for GeO$_x$ nanomembrane limits the planar device's area and aspect ratio, since the density of defects on the device's surface is normally increased with the etching time of the sacrificial layer. Considering this situation, the density of defects was tried to be controllable by increasing the cleaning level of the microfabrication environment, adopting the oxygen plasma to clean the surface of nanomembranes, using moderate metal deposition rates to avoid excessive stress in the deposited layers.

As shown in Figure 7.2, the rolling of this strained nanomembrane with aspect ratios of 0.5 × 1 mm^2 and 0.5 × 0.5 mm^2 was first attempted. Since limited defects on the surface, the yield of the nanomembrane rolling can be controlled at a very high level. Moreover, the rolling process results in the reduction of the footprint area to ~0.013 mm^2, which signifies the area is ~18 times smaller than the original unrolled size (0.050 mm^2).

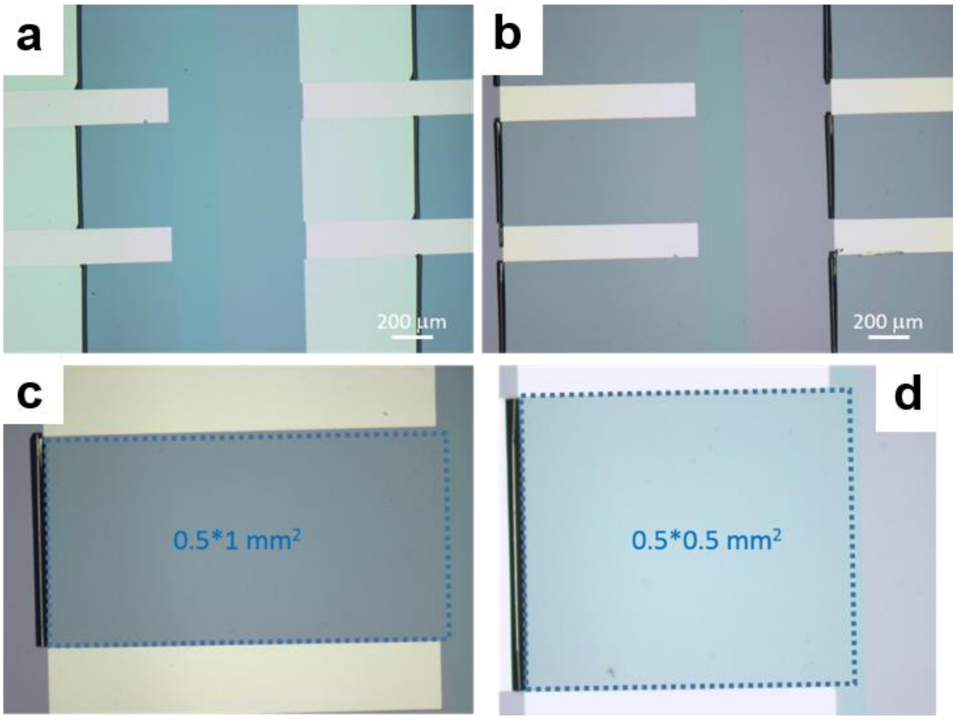

Figure 7.2. Optical microscopy images of Al_2O_3/Ti/Cr/Al_2O_3 strained nanomembrane in rolling process. The dashed lines indicate the area consumed by the planar nanomembrane before rolling.

The SEM images of a tubular Al_2O_3/Ti/Cr/Al_2O_3 in Figure 7.3 further display the detailed information of the rolling process. We can observe that the etching rate of GeO_x sacrificial layer at the edge is faster than that of the middle part. This preferentially lifted edge with defects generally tends to cause the tearing of strained nanomembrane, further resulting in the failure of the rolling process.

In addition to the function of electrical insulation, the dense Al_2O_3 layer shown in Figure 7.3b demonstrates its protection capability for the edges of a device which are not trenched in the rolling process. When GeO_x is etched away and the strained layer is released, the tearing of Al2O3 at the edge is also observed. Therefore, controlling the thickness of Al_2O_3 is an effective strategy to prevent the side effect and the tearing of edge nanomembrane.

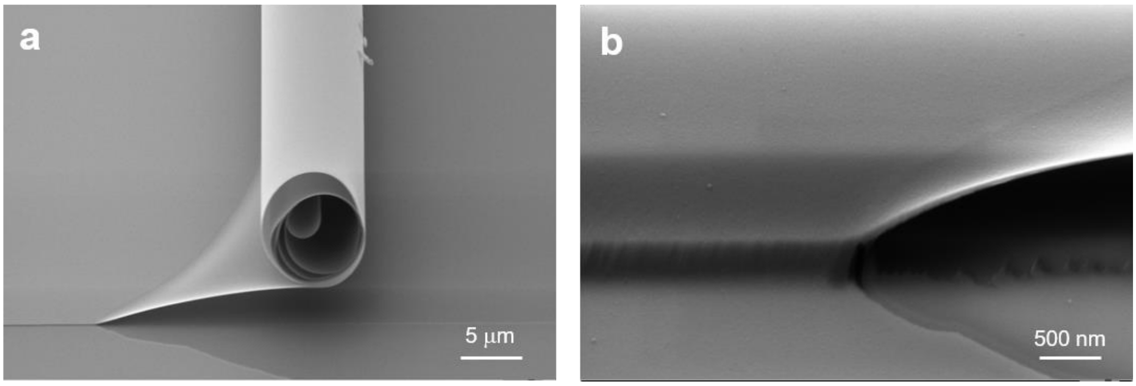

Figure 7.3. SEM images of a) a tubular Al_2O_3/Ti/Cr/Al_2O_3 in rolling process and b) the tearing of Al_2O_3 at the edges of planar nanomembrane.

Unlike the homogenous nanomembrane, interdigital structure contains gaps that are located between finger-type electrodes (Figure 7.4). This geometry may lead to an inhomogeneous stress distribution and decreased yield of final tubular architectures. Additionally, the thickness of the strained nanomembrane is limited to 60 nm, thus requiring that the electrode thickness must be also limited at a nanoscale level.

Therefore, interdigital Cr/Au current collectors with a thickness of 20 nm was then deposited on the strained nanomembrane. After planar devices were immersed in water at 50 °C for 4 h, some devices with the interdigital structure were finally self-assembled into the tube with a yield of 30 % (Figure 7.4b). This attempt results in the reduction of the footprint area to ~0.03 mm^2 and is ~16 times smaller than the planar size (0.050 mm^2). The diameter of tubes can be controlled at around 60 μm.

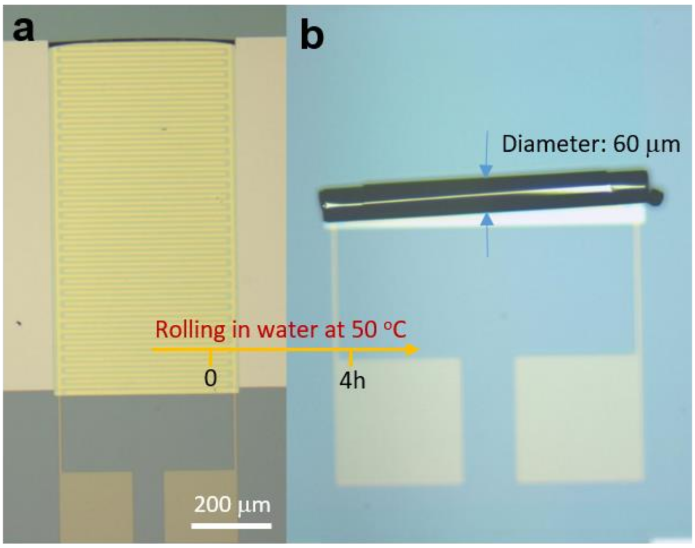

Figure 7.4. Optical microscopy images of interdigital current collectors on strained nanomembrane: a) before and b) after rolling.

In Figure 7.5a-7.5c, the SEM image shows the cross-section of a tubular structure with Cr/Au electrodes. This cut shows multiple windings of the "Swiss-roll" architecture, which consists of the strained layer and the finger-type electrodes. Compared to the tubular structure without electrode in Figure 7.5d, the electrodes inside tubes make the tube looser, implying the more space between two adjacent layers. For tubular MSCs, this 3D geometry structure should be beneficial on the ion transport between electrodes.

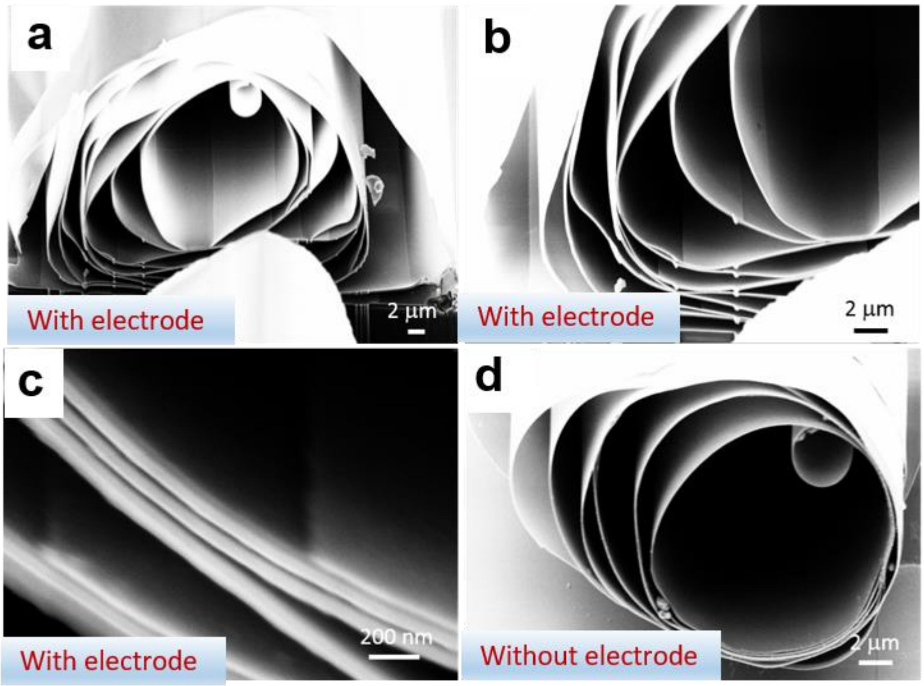

Figure 7.5. a-c) SEM images of cross-section of an electrode-loaded tube prepared by FIB-cutting with different magnifications. d) SEM image of a tube opening without loading of electrodes.

7.3. Self-assembly of Al_2O_3/Ni/Cr/Al_2O_3 strained nanomembranes

7.3.1. Fabrication method

The fabrication flow for MnO_2-based tubular MSCs with the assist of magnetic field is illustrated in Figure 6.1.

Sacrificial layer: MC solution was prepared by mixing 100 mg of MC powder with 100 ml water at 80 °C. The mixture was then cooled down to room temperature under continuous stirring. Spin coating of MC was performed at 3000 rpm for 35 s on a SiO_2 substrate that results in an MC layer of a few nanometer thickness. After that, the substrate is baked on a hotplate at 120 °C for 4 min.

Protection layer: The MC layer was encapsulated by a 15 nm Al_2O_3 layer deposited by thermal ALD. The deposition was done in a FlexAL system with a chuck temperature of 150 °C at a growth rate of 0.6 Å/cycle.

Metal layers: Ni/Cr metal deposition was performed inside an electron-beam evaporator with a base pressure better than $1 \times e^{-7}$ mbar on a water-cooled sample holder rotating with 4 rpm. 15 nm Ni was deposited at 1 Å s^{-1} and 20 nm Cr at 3 Å s^{-1}. For the contact pads, 5 nm Cr was deposited at 1 Å s^{-1} for adhesion and 50 nm Au at 2 Å s^{-1}. For current collectors, 5 nm Cr was deposited at 1 Å s^{-1} and 20 nm Au at 2 Å s^{-1}. Patterning of metal was done by lift-off in acetone from an AZ 5214 E resist mask processed in negative mode.

MnO_2 deposition: MnO_2 was electrochemically deposited on Au electrodes in a standard three-electrode system using a patterned interdigital Au/Cr electrode as the working electrode, a Pt wire as the counter electrode, and Ag/AgCl (saturated KCl) as a reference electrode. The electrolyte solution contained 0.1 M of Manganese (II) acetate ($Mn(CH_3COO)_2$) and 0.1 M of sodium sulfate (Na_2SO_4). A certain cycles of CV scan from 0 V to 0.45 V at 50 mV s^{-1} were

applied during the process. Then the interdigital MnO_2 electrode was washed with deionized water and air-dried at room temperature.

Trench opening: Reactive-ion etching (RIE) was performed in a Plasmalab 100 tool. For etching Al_2O_3, the following process parameters were used: 0.06 mbar, 50 sccm CF_4, 200W radio frequency, and 35 °C. The etch rate was measured by a stylus profilometer to be 3-4 nm/min.

Assembling process: The assembly was performed inside a dipole electromagnet with 50 mm pole gap and 115 mm pole face diameter at 10 kOe magnetic field. The sample is fixed inside a PTFE holder with vacuum suction.

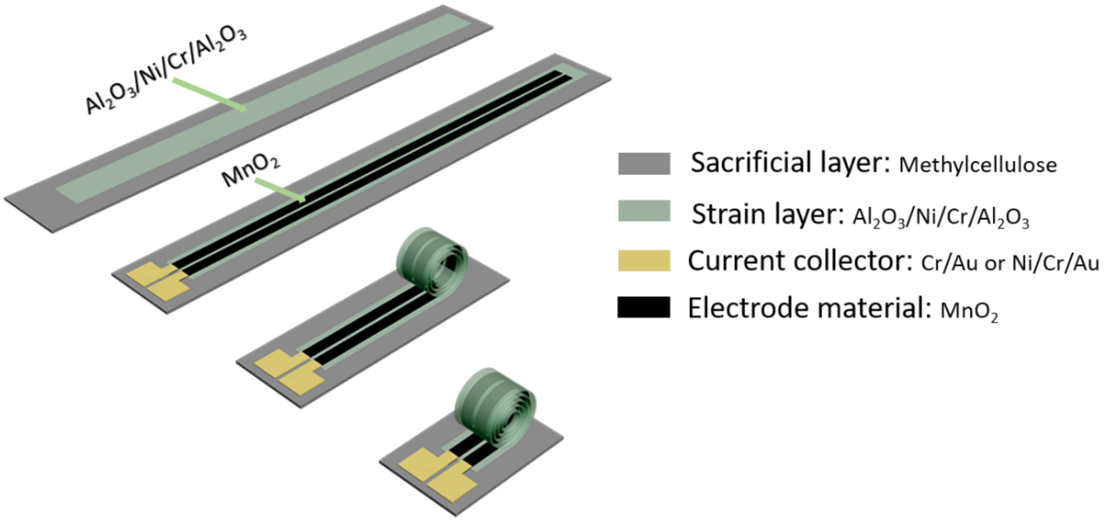

Figure 7.6. Schematic illustration of the fabrication of a tubular MSC based on MnO_2 electrodes and its rolling under the assist of magnetic field.

7.3.2. Results and discussion

The $Al_2O_3/Ti/Cr/Al_2O_3$ nanomembrane has been demonstrated as a strain layer to assemble the interdigital electrode into 3D “Swiss-roll” architecture in the previous section. However, this self-assembly strategy also shows some challengeable issues: 1) Low yield caused by the tearing from nanomembrane edges, 2) slow-rolling rate determined by the etching rate of GeO_x sacrificial layer, and 3) the low-aspect-ratio between device’s length and width.

To solve those issues, an alternative strategy for controlling the rolling of a high-aspect-ratio nanomembrane in magnetic fields was employed in this section. In this approach, the MC sacrificial layer can be quickly dissolved in aqueous solution, thus promoting the rolling process with high speed. Simultaneously, the rolling direction of Al_2O_3/Ni/Cr/Al_2O_3 magnetic nanomembrane can be precisely controlled by the external magnetic fields. As shown in Figure 7.7, the planar trapezoidal structure with a length of 5.2 mm and a width of 0.2/0.3 mm was designed. Two stripe-type electrodes with the gap size of 5 μm, 10 μm, and 15 μm were fabricated on its surface.

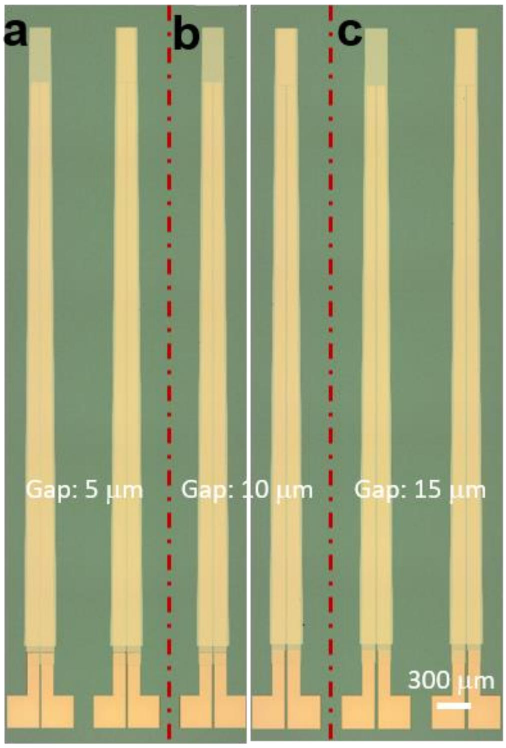

Figure 7.7. Optical microscopy images of current collectors on the Al_2O_3/Ni/Cr/Al_2O_3 strained nanomembrane.

MnO_2 has been considered as a promising alternative material for supercapacitor electrode due to its low cost and high theoretical capacitance range from 1100 to 1300 F g^{-1}.[232] Especially, the chemical and associated electrode potentials of MnO_2 in neutral aqueous electrolytes are a continuous function of the degree of charge. The charge storage mechanism in the MnO_2 electrode, used in aqueous electrolyte, was accompanied by the surface state varying from III to IV. Moreover, only a thin layer of MnO_2 is involved in the redox process and is electrochemically active.[232] Therefore, it is essential to determine a deposition strategy that can fabricate a thin layer of MnO_2 with the high specific surface area on the strained nanomembrane.

In Chapter 5 and Chapter 6, a standard three-electrode system was utilized to electrodeposit PEDOT active material with the high surface area. Therefore, this successful electrochemical method was also employed here to fabricate the MnO_2 electrode on the strained nanomembrane. Owing to the limitation of intrinsic strain energy, the thickness of MnO_2 is required to be precisely controlled at a nanometre scale level (Figure 7.8a). Figure 7.8b is a representative SEM image of the uniformly electrodeposited MnO_2 layer on the surface of Au current collectors. This image clearly shows that the MnO_2 layer consists of flower-like MnO_2 nanoparticles.

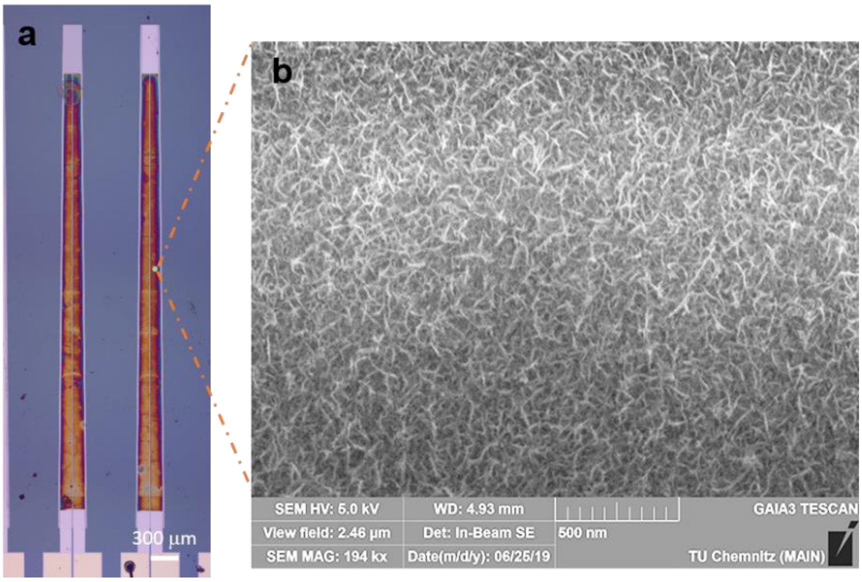

Figure 7.8. a) Optical microscopy image of MnO_2 electrodes on the Al_2O_3/Ni/Cr/Al_2O_3 nanomembrane. b) SEM image of electrodeposited MnO_2.

Table 7.1. Deposition parameters and thickness of MnO_2

Devices	CV cycles	Thickness of MnO_2
$C_{0.5}$	0.5	15.8 nm
C_1	1	19.7 nm
C_2	2	33.1 nm
C_4	4	53.6 nm

MnO_2 electrodes with different thicknesses were electrodeposited on Au current collectors by controlling the CV cycles (0.5, 1, 2, and 3 cycles). Here, the electrodes are denoted by $C_{0.5}$, C_1, C_2, and C_4, respectively. As shown in Table

7.1, the MnO_2 thickness can be controlled between 15.8 nm and 53.6 nm, providing the possibility for the successful self-assembly.

The real-time photographs in Figure 7.9 record the rolling process for samples $C_{0.5}$ and C_1 in magnetic fields. The bright lines represent the self-assembled tube. For the devices ($C_{0.5}$ and C_1) without the current collector on the head, their rolling can be successfully controlled along the designed direction. This result also demonstrates that this strained nanomembrane can roll up MnO_2 electrodes with the thickness up to 19.7 nm.

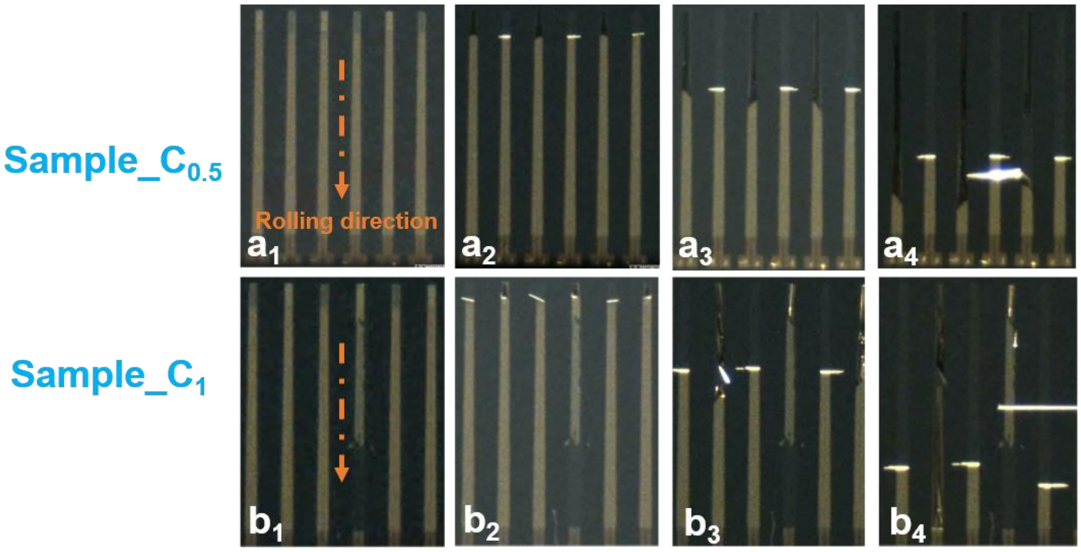

Figure 7.9. Real-time photographs of the rolling process after samples ($C_{0.5}$ and C_1) were immersed in aqueous solution.

Figure 7.10 shows the final tubes ($C_{0.5}$) with a diameter of ~186 μm. This rolling process results in the reduction of the footprint area to ~0.056 mm^2 and is ~23 times smaller than the planar size (1.3 mm^2). After the tubular device is sealed by LiCl gel-type electrolyte, its electrochemical performance was then investigated using CV at 0.05 V s^{-1} in a potential window of 0.8 V, as shown in Figure 7.10b. The closed CV curve with a certain area demonstrates that such tubular device possesses a certain capacitance behavior of the supercapacitor. However, the asymmetric curve implies that the tubular device should be further optimized.

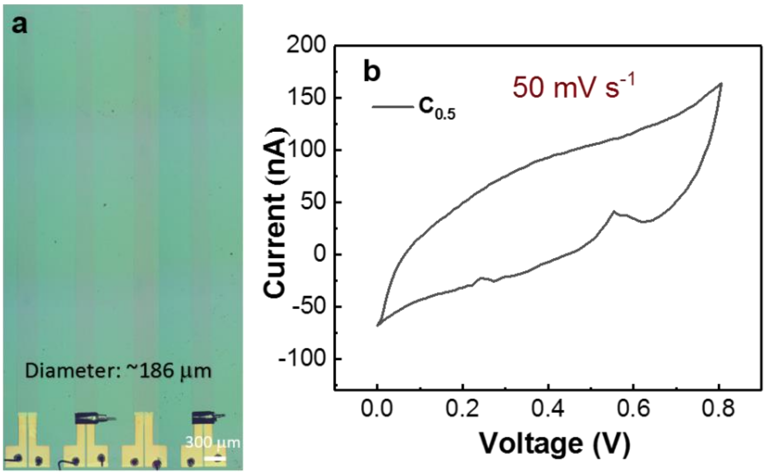

Figure 7.10. a) Optical microscopy image of tubular MSC with the loading of MnO_2. b) CV curve of this tubular MSC ($C_{0.5}$) over a potential window of 0.8 V at 50 mV s^{-1}.

7.4. Conclusion

Based on the rolled-up nanotechnology and photolithography methods, the Al_2O_3/Ti/Cr/Al_2O_3 nanomembranes were fabricated on the GeO_x sacrificial layer. Such strained nanomembranes consisting of an interdigital current collector can be self-assembled into 3D “Swiss-roll” architecture by etching GeO_x. However, the tearing from nanomembrane edges was a challenging issue which causes the low yield of final tubular devices. Therefore, an alternative strategy for controlling the rolling in magnetic fields was further investigated. The results show that this magnetic assisted method can drive the rolling of high-aspect-ratio Al_2O_3/Ni/Cr/Al_2O_3 nanomembranes in few seconds. Electrodeposited MnO_2 was selected as a representative active material to develop the fabrication method and explore the optimized rolling parameters. The results show the rolling process can effectively reduce the footprint area of original planar devices.

Chapter 8. Summary and outlook

8.1. Summary

The dissertation aims to explore MSCs with the functionalization and high areal electrochemical performance. MSCs have been regarded as a promising micro-power towards the application in integrated and miniaturized electronics. To date, the biggest challenge in the research on MSCs is to develop a reliable and smart fabrication technology which can integrate diverse functional materials into devices. One ideal strategy is to transform planar MSCs from two-dimensional to three-dimensional architectures using strain engineering. By this approach, the active materials in supercapacitors can be wrapped inside this configuration with a self-protection function and a decreased footprint area.

In this dissertation, planar interdigital MSC electrodes were firstly designed and fabricated using the photolithography technique. A thermo-responsible electrolyte was covered on the surface of PEDOT based electrodes to achieve the function of switch on/off. Additionally, four MSCs and wafer-scale 100 MSCs connected in series and parallel were also designed and fabricated, demonstrating that the voltage and capacitance output can be adjustable by such fabrication techniques.

Subsequently, the planar interdigital PEDOT electrodes were fabricated onto the strained polymeric layer stacks and self-assembled into a tubular “Swiss-roll” architecture by selectively etching the sacrificial layer. Such a polymeric framework consisting of the swelling hydrogel and PI layer can ensure the excellent ion transport between PEDOT electrodes and provide efficient self-protection for the tubular MSC against external compression up to about 30 MPa. It exhibits an areal capacitance of 82.5 mF cm^{-2} at 0.3 mA cm^{-2} with a potential window of 0.8 V, an energy density and power density of 7.73 μWh cm^{-2} and 17.8 mW cm^{-2} (0.3 and 45 mA cm^{-2}), and an improved cycling stability with a capacitance retention up to 96.6 % over 5000 cycles. Furthermore, as-fabricated tubular MSC arrays can be detached from their surface and transferred onto target substrates. The connection of devices in parallel/series greatly improves their capacitance and voltage output.

Nanoscale Al_2O_3/Ti/Cr/Al_2O_3 strained layer was another choice to assemble interdigital MSC into the tubular architecture. The investigation shows that the tearing from nanomembrane edges generally causes the low yield of final tubular devices. Therefore, Ni element was further introduced into the strained layer to achieve a controllable rolling in the magnetic field. The result shows that this magnetic assisted method can effectively drive the rolling of a high-aspect-ratio Al_2O_3/Ni/Cr/Al_2O_3 nanomembrane in few seconds. Stripe-type MnO_2 electrodes with a thickness of 19.7 nm were then rolled into the tubular structure.

8.2. Outlook

Polymeric layer stacks have been demonstrated as a platform to self-assemble PEDOT-based interdigital MSCs. The hydrogel layer inside can ensure the ion transport between rolled electrodes. Reduced footprint area and improved cycling performance have been achieved. However, there are still many aspects that need to be investigated in future research.

1. One direction of further research is to develop the tubular asymmetric/hybrid MSCs. The advantage of asymmetric/hybrid MSCs is their excellent electrochemical performance, compared to symmetric ones. Therefore, introducing those novel MSCs into tubular structure can greatly promote the development of tubular MSCs.
2. Another research direction is to investigate tubular MSCs with other functionalization (*e.g.* electrochromism, flexibility as well as wearability). For instance, such tubular MSCs have shown the self-protection function. Therefore, a detailed study on the related mechanical function should be carried out, thus expanding the application of tubular MSCs.

Magnetically assisted self-assembly of inorganic nanomembrane is an effectively and attractive strategy to construct 3D MSCs with a limited footprint area. Further work should be carried out to optimize the electrode structure and electrochemical performance.

Bibliography

[1] J. Wang, F. Li, F. Zhu, O. G. Schmidt, *Small Methods* **2018**, *3*, 1800367.

[2] C. Lethien, J. Le Bideau, T. Brousse, *Energy Environ. Sci.* **2019**, *12*, 96.

[3] M. Beidaghi, Y. Gogotsi, *Energy Environ. Sci.* **2014**, *7*, 867.

[4] N. A. Kyeremateng, T. Brousse, D. Pech, *Nat. Nanotechnol.* **2016**, *12*, 7.

[5] L. Liu, Q. Weng, X. Lu, X. Sun, L. Zhang, O. G. Schmidt, *Small* **2017**, *13*, 1701847.

[6] J. Ren, Y. Zhang, W. Bai, X. Chen, Z. Zhang, X. Fang, W. Weng, Y. Wang, H. Peng, *Angew. Chem. Int. Ed.* **2014**, *53*, 7864.

[7] J. F. M. Oudenhoven, L. Baggetto, P. H. L. Notten, *Adv. Energy Mater.* **2011**, *1*, 10.

[8] J. Deng, X. Lu, L. Liu, L. Zhang, O. G. Schmidt, *Adv. Energy Mater.* **2016**, *6*, 1600797.

[9] M. S. Islam, C. A. J. Fisher, *Chem. Soc. Rev.* **2014**, *43*, 185.

[10] N. S. Choi, Z. Chen, S. A. Freunberger, X. Ji, Y. K. Sun, K. Amine, G. Yushin, L. F. Nazar, J. Cho, P. G. Bruce, *Angew. Chem. Int. Ed.* **2012**, *51*, 9994.

[11] Y. Zhai, Y. Dou, D. Zhao, P. F. Fulvio, R. T. Mayes, S. Dai, *Adv. Mater.* **2011**, *23*, 4828.

[12] Z. Wu, L. Li, J. M. Yan, X. B. Zhang, *Adv. Sci.* **2017**, *4*, 1600382.

[13] S. Chen, Y. Liu, J. Chen, *Chem. Soc. Rev.* **2014**, *43*, 5372.

[14] R. Burt, G. Birkett, X. S. Zhao, *Phys. Chem. Chem. Phys.* **2014**, *16*, 6519.

[15] P. Simon, Y. Gogotsi, *Nat. Mater.* **2008**, *7*, 845.

[16] E. Lim, C. Jo, J. Lee, *Nanoscale* **2016**, *8*, 7827.

[17] L. L. Zhang, X. S. Zhao, *Chem. Soc. Rev.* **2009**, *38*, 2520.

[18] H. Helmholtz, *Ann. Phys.* **1879**, *243*, 337.

[19] D. L. Chapman, *London, Edinburgh, Dublin Philos. Mag. J. Sci.* **1913**, *25*, 475.

[20] M. Gouy, *J. Phys. Theor. Appl.* **1910**, *9*, 457.

[21] H. O. Stern-Hamburg, *J. Electrochem. Appl. Phys. Chem.* **1924**, *30*, 508.

[22] V. Augustyn, P. Simon, B. Dunn, *Energy Environ. Sci.* **2014**, *7*, 1597.

[23] A. Ferris, S. Garbarino, D. Guay, D. Pech, *Adv. Mater.* **2015**, *27*, 6625.

[24] Y. Q. Li, X. M. Shi, X. Y. Lang, Z. Wen, J. C. Li, Q. Jiang, *Adv. Funct. Mater.* **2016**, *26*, 1830.

[25] X. Shi, Z. S. Wu, J. Qin, S. Zheng, S. Wang, F. Zhou, C. Sun, X. Bao, *Adv. Mater.* **2017**, *29*, 1703034.

[26] M. Zhu, Y. Huang, Y. Huang, H. Li, Z. Wang, Z. Pei, Q. Xue, H. Geng, C. Zhi, *Adv. Mater.* **2017**, *29*, 1605137.

[27] P. Zhang, J. Wang, W. Sheng, F. Wang, J. Zhang, F. Zhu, X. Zhuang, R. Jordan, O. G. Schmidt, X. Feng, *Energy Environ. Sci.* **2018**, *11*, 1717.

[28] N. T. Nguyen, S. Ozkan, I. Hwang, X. Zhou, P. Schmuki, *J. Mater. Chem. A* **2017**, *5*, 1895.

[29] S. M. Mirvakili, I. W. Hunter, *Adv. Mater.* **2017**, *29*, 1700671.

[30] P. Zhang, F. Zhu, F. Wang, J. Wang, R. Dong, X. Zhuang, O. G. Schmidt, X. Feng, *Adv. Mater.* **2017**, *29*, 1604491.

[31] H. Ji, X. Liu, Z. Liu, B. Yan, L. Chen, Y. Xie, C. Liu, W. Hou, G. Yang, *Adv. Funct. Mater.* **2015**, *25*, 1886.

[32] M. Beidaghi, Y. Gogotsi, *Energy Environ. Sci.* **2014**, *7*, 867.

[33] L. Liu, Z. Niu, J. Chen, *Chem. Soc. Rev.* **2016**, *45*, 4340.

[34] D. Yu, Q. Qian, L. Wei, W. Jiang, K. Goh, J. Wei, J. Zhang, Y. Chen, *Chem. Soc. Rev.* **2015**, *44*, 647.

[35] G. Sun, X. Wang, P. Chen, *Mater. Today* **2015**, *18*, 215.

[36] X. Wang, K. Jiang, G. Shen, *Mater. Today* **2015**, *18*, 265.

[37] S. J. Varma, K. Sambath Kumar, S. Seal, S. Rajaraman, J. Thomas, *Adv. Sci.* **2018**, *5*, 1800340.

[38] N. Liu, Y. Gao, *Small* **2017**, *13*, 1701989.

[39] D. Pech, M. Brunet, H. Durou, P. Huang, V. Mochalin, Y. Gogotsi, P. L. Taberna, P. Simon, *Nat. Nanotechnol.* **2010**, *5*, 651.

[40] H. Hu, K. Zhang, S. Li, S. Ji, C. Ye, *J. Mater. Chem. A* **2014**, *2*, 20916.

[41] J. Bin In, B. Hsia, J. H. Yoo, S. Hyun, C. Carraro, R. Maboudian, C. P. Grigoropoulos, *Carbon N. Y.* **2015**, *83*, 144.

[42] J. Gao, C. Shao, S. Shao, F. Wan, C. Gao, Y. Zhao, L. Jiang, L. Qu, *Small* **2018**, *14*, 1801809.

[43] M. F. El-Kady, V. Strong, S. Dubin, R. B. Kaner, *Science* **2012**, *335*, 1326.

[44] J. Yoo, S. Byun, C. W. Lee, C. Y. Yoo, J. Yu, *Chem. Mater.* **2017**, *30*, 3979.

[45] N. Kurra, B. Ahmed, Y. Gogotsi, H. N. Alshareef, *Adv. Energy Mater.* **2016**,

6, 1601372.

[46] H. Pang, Y. Zhang, W. Y. Lai, Z. Hu, W. Huang, *Nano Energy* **2015**, *15*, 303.

[47] Y. Wang, Y. Z. Zhang, D. Dubbink, J. E. ten Elshof, *Nano Energy* **2018**, *49*, 481.

[48] W. Liu, C. Lu, H. Li, R. Y. Tay, L. Sun, X. Wang, W. L. Chow, X. Wang, B. K. Tay, Z. Chen, J. Yan, K. Feng, G. Lui, R. Tjandra, L. Rasenthiram, G. Chiu, A. Yu, *J. Mater. Chem. A* **2016**, *4*, 3754.

[49] M. F. El-Kady, R. B. Kaner, *Nat. Commun.* **2013**, *4*, 1475.

[50] S. Wang, N. Liu, J. Tao, C. Yang, W. Liu, Y. Shi, Y. Wang, J. Su, L. Li, Y. Gao, *J. Mater. Chem. A* **2015**, *3*, 2407.

[51] X. Pu, M. Liu, L. Li, S. Han, X. Li, C. Jiang, C. Du, J. Luo, W. Hu, Z. L. Wang, *Adv. Energy Mater.* **2016**, *6*, 1601254.

[52] S. Bae, H. Kim, Y. Lee, X. Xu, J. S. Park, Y. Zheng, J. Balakrishnan, T. Lei, H. Ri Kim, Y. I. Song, Y. J. Kim, K. S. Kim, B. Özyilmaz, J. H. Ahn, B. H. Hong, S. Iijima, *Nat. Nanotechnol.* **2010**, *5*, 574.

[53] R. Guo, J. Chen, B. Yang, L. Liu, L. Su, B. Shen, X. Yan, *Adv. Funct. Mater.* **2017**, *27*, 1702394.

[54] J. Q. Xie, Y. Q. Ji, J. H. Kang, J. L. Sheng, D. S. Mao, X. Z. Fu, R. Sun, C. P. Wong, *Energy Environ. Sci.* **2019**, *12*, 194.

[55] G. Chisholm, P. J. Kitson, N. D. Kirkaldy, L. G. Bloor, L. Cronin, *Energy Environ. Sci.* **2014**, *7*, 3026.

[56] K. Sun, T. S. Wei, B. Y. Ahn, J. Y. Seo, S. J. Dillon, J. A. Lewis, *Adv. Mater.* **2013**, *25*, 4539.

[57] W. Yu, H. Zhou, B. Q. Li, S. Ding, *ACS Appl. Mater. Interfaces* **2017**, *9*, 4597.

[58] Z. Wang, Q. Zhang, S. Long, Y. Luo, P. Yu, Z. Tan, J. Bai, B. Qu, Y. Yang, J. Shi, H. Zhou, Z. Y. Xiao, W. Hong, H. Bai, *ACS Appl. Mater. Interfaces* **2018**, *10*, 10437.

[59] Y. L. Kong, I. A. Tamargo, H. Kim, B. N. Johnson, M. K. Gupta, T. W. Koh, H. A. Chin, D. A. Steingart, B. P. Rand, M. C. McAlpine, *Nano Lett.* **2014**, *14*, 7017.

[60] J. T. Muth, D. M. Vogt, R. L. Truby, Y. Mengüç, D. B. Kolesky, R. J. Wood, J. A. Lewis, *Adv. Mater.* **2014**, *26*, 6307.

[61] K. Shen, J. Ding, S. Yang, *Adv. Energy Mater.* **2018**, *8*, 1800408.

[62] T. Göhlert, P. F. Siles, T. Päßler, R. Sommer, S. Baunack, S. Oswald, O. G. Schmidt, *Nano Energy* **2017**, *33*, 387.

[63] P. Huang, C. Lethien, S. Pinaud, K. Brousse, R. Laloo, V. Turq, M. Respaud, A. Demortière, B. Daffos, P. L. Taberna, B. Chaudret, Y. Gogotsi, P. Simon, *Science* **2016**, *351*, 691.

[64] H. Xiao, Z. S. Wu, L. Chen, F. Zhou, S. Zheng, W. Ren, H. M. Cheng, X. Bao, *ACS Nano* **2017**, *11*, 7284.

[65] Z. Liu, Z. S. Wu, S. Yang, R. Dong, X. Feng, K. Müllen, *Adv. Mater.* **2016**, *28*, 2217.

[66] J. Lin, C. Zhang, Z. Yan, Y. Zhu, Z. Peng, R. H. Hauge, D. Natelson, J. M. Tour, *Nano Lett.* **2013**, *13*, 72.

[67] A. Ramadoss, B. Saravanakumar, S. W. Lee, Y. S. Kim, S. J. Kim, Z. L. Wang, *ACS Nano* **2015**, *9*, 4337.

[68] R. Yang, Y. Qin, L. Dai, Z. L. Wang, *Nat. Nanotechnol.* **2009**, *4*, 34.

[69] F. R. Fan, Z. Q. Tian, Z. Lin Wang, *Nano Energy* **2012**, *1*, 328.

[70] Z. L. Wang, *ACS Nano* **2013**, *7*, 9533.

[71] Y. Zi, J. Wang, S. Wang, S. Li, Z. Wen, H. Guo, Z. L. Wang, *Nat. Commun.* **2016**, *7*, 10987.

[72] Z. L. Wang, *Faraday Discuss.* **2014**, *176*, 447.

[73] Z. L. Wang, J. Chen, L. Lin, *Energy Environ. Sci.* **2015**, *8*, 2250.

[74] J. Chun, B. U. Ye, J. W. Lee, D. Choi, C. Y. Kang, S. W. Kim, Z. L. Wang, J. M. Baik, *Nat. Commun.* **2016**, *7*, 12985.

[75] Y. Song, X. Cheng, H. Chen, J. Huang, X. Chen, M. Han, Z. Su, B. Meng, Z. Song, H. Zhang, *J. Mater. Chem. A* **2016**, *4*, 14298.

[76] Y. Zi, L. Lin, J. Wang, S. Wang, J. Chen, X. Fan, P. K. Yang, F. Yi, Z. L. Wang, *Adv. Mater.* **2015**, *27*, 2340.

[77] S. Qin, Q. Zhang, X. Yang, M. Liu, Q. Sun, Z. L. Wang, *Adv. Energy Mater.* **2018**, *8*, 1800069.

[78] E. Navarrete-Astorga, D. Solís-Cortés, J. Rodríguez-Moreno, E. A. Dalchiele, R. Schrebler, F. Martín, J. R. Ramos-Barrado, *Chem. Commun.* **2018**, *54*, 10762.

[79] Y. Fu, H. Wu, S. Ye, X. Cai, X. Yu, S. Hou, H. Kafafy, D. Zou, *Energy Environ. Sci.* **2013**, *6*, 805.

[80] H. Sun, X. You, J. Deng, X. Chen, Z. Yang, P. Chen, X. Fang, H. Peng, *Angew. Chem. Int. Ed.* **2014**, *53*, 6664.

[81] J. Xu, H. Wu, L. Lu, S. F. Leung, D. Chen, X. Chen, Z. Fan, G. Shen, D. Li, *Adv. Funct. Mater.* **2014**, *24*, 1840.

[82] Y. Yin, K. Feng, C. Liu, S. Fan, *J. Phys. Chem. C* **2015**, *119*, 8488.

[83] J. Kim, S. M. Lee, Y. H. Hwang, S. Lee, B. Park, J. H. Jang, K. Lee, *J. Mater. Chem. A* **2017**, *5*, 1906.

[84] R. Liu, C. Liu, S. Fan, *J. Mater. Chem. A* **2017**, *5*, 23078.

[85] Z. Liu, Y. Zhong, B. Sun, X. Liu, J. Han, T. Shi, Z. Tang, G. Liao, *ACS Appl. Mater. Interfaces* **2017**, *9*, 22361.

[86] T. Chen, L. Qiu, Z. Yang, Z. Cai, J. Ren, H. Li, H. Lin, X. Sun, H. Peng, *Angew. Chem. Int. Ed.* **2012**, *51*, 11977.

[87] X. Chen, H. Sun, Z. Yang, G. Guan, Z. Zhang, L. Qiu, H. Peng, *J. Mater. Chem. A* **2014**, *2*, 1897.

[88] G. Wee, T. Salim, Y. M. Lam, S. G. Mhaisalkar, M. Srinivasan, *Energy Environ. Sci.* **2011**, *4*, 413.

[89] A. P. Cohn, W. R. Erwin, K. Share, L. Oakes, A. S. Westover, R. E. Carter, R. Bardhan, C. L. Pint, *Nano Lett.* **2015**, *15*, 2727.

[90] C. Li, M. M. Islam, J. Moore, J. Sleppy, C. Morrison, K. Konstantinov, S. X. Dou, C. Renduchintala, J. Thomas, *Nat. Commun.* **2016**, *7*, 13319.

[91] K. Wang, H. Wu, Y. Meng, Y. Zhang, Z. Wei, *Energy Environ. Sci.* **2012**, *5*, 8384.

[92] D. Wei, M. R. J. Scherer, C. Bower, P. Andrew, T. Ryhänen, U. Steiner, *Nano Lett.* **2012**, *12*, 1857.

[93] Y. Guo, W. Li, H. Yu, D. F. Perepichka, H. Meng, *Adv. Energy Mater.* **2017**, *7*, 1601623.

[94] K. Li, Y. Shao, S. Liu, Q. Zhang, H. Wang, Y. Li, R. B. Kaner, *Small* **2017**, *13*, 1700380.

[95] Y. Zhong, Z. Chai, Z. Liang, P. Sun, W. Xie, C. Zhao, W. Mai, *ACS Appl. Mater. Interfaces* **2017**, *9*, 34085.

[96] X. Chen, H. Lin, J. Deng, Y. Zhang, X. Sun, P. Chen, X. Fang, Z. Zhang, G. Guan, H. Peng, *Adv. Mater.* **2014**, *26*, 8126.

[97] Y. Tian, S. Cong, W. Su, H. Chen, Q. Li, F. Geng, Z. Zhao, *Nano Lett.* **2014**, *14*, 2150.

[98] Y. Chen, Y. Wang, P. Sun, P. Yang, L. Du, W. Mai, *J. Mater. Chem. A* **2015**, *3*, 20614.

[99] Y. Huang, M. Zhu, Y. Huang, W. Meng, Q. Gong, G. Li, C. Zhi, *J. Mater. Chem. A* **2015**, *3*, 21321.

[100] F. Zhou, Z. Ren, Y. Zhao, X. Shen, A. Wang, Y. Y. Li, C. Surya, Y. Chai, *ACS Nano* **2016**, *10*, 5900.

[101] Y. Zhou, Y. Zhao, J. Fang, T. Lin, *RSC Adv.* **2016**, *6*, 110164.

[102] Z. Bi, X. Li, Y. Chen, X. He, X. Xu, X. Gao, *ACS Appl. Mater. Interfaces* **2017**, *9*, 29872.

[103] G. Cai, P. Darmawan, X. Cheng, P. S. Lee, *Adv. Energy Mater.* **2017**, *7*, 1602598.

[104] P. Yang, P. Sun, W. Mai, *Mater. Today* **2016**, *19*, 394.

[105] L. Zhang, M. Liao, L. Bao, X. Sun, H. Peng, *Small Methods* **2017**, *1*, 1700211.

[106] G. Cai, X. Wang, M. Cui, P. Darmawan, J. Wang, A. L. S. Eh, P. S. Lee, *Nano Energy* **2015**, *12*, 258.

[107] P. Zhang, F. Zhu, F. Wang, J. Wang, R. Dong, X. Zhuang, O. G. Schmidt, X. Feng, *Adv. Mater.* **2017**, *29*, 1604491.

[108] D. Chen, D. Wang, Y. Yang, Q. Huang, S. Zhu, Z. Zheng, *Adv. Energy Mater.* **2017**, *7*, 1700890.

[109] H. Wang, B. Zhu, W. Jiang, Y. Yang, W. R. Leow, H. Wang, X. Chen, *Adv. Mater.* **2014**, *26*, 3638.

[110] Y. Huang, M. Zhong, Y. Huang, M. Zhu, Z. Pei, Z. Wang, Q. Xue, X. Xie, C. Zhi, *Nat. Commun.* **2015**, *6*, 10310.

[111] Y. Yue, N. Liu, Y. Ma, S. Wang, W. Liu, C. Luo, H. Zhang, F. Cheng, J. Rao, X. Hu, J. Su, Y. Gao, *ACS Nano* **2018**, *12*, 4224.

[112] Y. Huang, Y. Huang, M. Zhu, W. Meng, Z. Pei, C. Liu, H. Hu, C. Zhi, *ACS Nano* **2015**, *9*, 6242.

[113] X. Hou, B. Liu, X. Wang, Z. Wang, Q. Wang, D. Chen, G. Shen, *Nanoscale* **2013**, *5*, 7831.

[114] D. Kim, J. Yun, G. Lee, J. Sook Ha, *Nanoscale* **2014**, *6*, 12034.

[115] L. Sun, X. Wang, K. Zhang, J. Zou, Z. Yan, X. Hu, Q. Zhang, *Nano Energy* **2015**, *15*, 445.

[116] X. Wang, S. Yao, X. Wu, Z. Shi, H. Sun, R. Que, *RSC Adv.* **2015**, *5*, 17938.

[117] J. Xu, G. Shen, *Nano Energy* **2015**, *13*, 131.

[118] C. Chen, J. Cao, Q. Lu, X. Wang, L. Song, Z. Niu, J. Chen, *Adv. Funct. Mater.* **2017**, *27*, 1604639.

[119] J. Yun, Y. Lim, G. N. Jang, D. Kim, S. J. Lee, H. Park, S. Y. Hong, G. Lee, G. Zi, J. S. Ha, *Nano Energy* **2016**, *19*, 401.

[120] D. Kim, K. Keum, G. Lee, D. Kim, S. S. Lee, J. S. Ha, *Nano Energy* **2017**, *35*, 199.

[121] Y. Song, H. Chen, X. Chen, H. Wu, H. Guo, X. Cheng, B. Meng, H. Zhang, *Nano Energy* **2018**, *53*, 189.

[122] Z. Yang, J. Deng, X. Chen, J. Ren, H. Peng, *Angew. Chem- Int. Ed.* **2013**, *125*, 13695.

[123] Y. Zhang, W. Bai, X. Cheng, J. Ren, W. Weng, P. Chen, X. Fang, Z. Zhang, H. Peng, *Angew. Chem. Int. Ed.* **2014**, *53*, 14564.

[124] D. Qi, Z. Liu, Y. Liu, W. R. Leow, B. Zhu, H. Yang, J. Yu, W. Wang, H. Wang, S. Yin, X. Chen, *Adv. Mater.* **2015**, *27*, 5559.

[125] G. Xiong, A. Kundu, T. S. Fisher, *Thermal Effects in Supercapacitors*, Springer, **2015**.

[126] N. Vichare, P. Rodgers, V. Eveloy, M. G. Pecht, *IEEE Trans. Device Mater. Reliab.* **2004**, *4*, 658.

[127] R. Kötz, M. Hahn, R. Gallay, *J. Power Sources* **2006**, *154*, 550.

[128] H. Yang, W. R. Leow, X. Chen, *Adv. Mater.* **2018**, *30*, 1704347.

[129] Y. Dou, T. Pan, A. Zhou, S. Xu, X. Liu, J. Han, M. Wei, D. G. Evans, X. Duan, *Chem. Commun.* **2013**, *49*, 8462.

[130] H. Yang, Z. Liu, B. K. Chandran, J. Deng, J. Yu, D. Qi, W. Li, Y. Tang, C. Zhang, X. Chen, *Adv. Mater.* **2015**, *27*, 5593.

[131] Y. Shi, H. Ha, A. Al-Sudani, C. J. Ellison, G. Yu, *Adv. Mater.* **2016**, *28*, 7810.

[132] Z. Liu, H. I. Wang, A. Narita, Q. Chen, Z. Mics, D. Turchinovich, M. Kläui, M. Bonn, K. Müllen, *J. Am. Chem. Soc.* **2017**, *139*, 9443.

[133] J. Zou, M. Zhang, J. Huang, J. Bian, Y. Jie, M. Willander, X. Cao, N. Wang, Z. L. Wang, *Adv. Energy Mater.* **2018**, *8*, 1702671.

[134] M. F. El-Kady, M. Ihns, M. Li, J. Y. Hwang, M. F. Mousavi, L. Chaney, A. T. Lech, R. B. Kaner, *Proc. Natl. Acad. Sci. U. S. A.* **2015**, *112*, 4233.

[135] X. Tian, J. Jin, S. Yuan, C. K. Chua, S. B. Tor, K. Zhou, *Adv. Energy Mater.* **2017**, *7*, 1700127.

[136] O. G. Schmidt, K. Eberl, *Nature* **2001**, *410*, 168.

[137] R. Sharma, C. C. B. Bufon, D. Grimm, R. Sommer, A. Wollatz, J. Schadewald, D. J. Thurmer, P. F. Siles, M. Bauer, O. G. Schmidt, *Adv. Energy Mater.* **2014**, *4*, 1301631.

[138] C. C. Bof Bufon, J. D. Cojal González, D. J. Thurmer, D. Grimm, M. Bauer, O. G. Schmidt, *Nano Lett.* **2010**, *10*, 2506.

[139] D. Karnaushenko, D. D. Karnaushenko, D. Makarov, S. Baunack, R. Schäfer, O. G. Schmidt, *Adv. Mater.* **2015**, *27*, 6582.

[140] D. Karnaushenko, N. Münzenrieder, D. D. Karnaushenko, B. Koch, A. K. Meyer, S. Baunack, L. Petti, G. Tröster, D. Makarov, O. G. Schmidt, *Adv. Mater.* **2015**, *27*, 6797.

[141] D. Joung, K. Agarwal, H. R. Park, C. Liu, S. H. Oh, J. H. Cho, *Adv. Electron. Mater.* **2016**, *2*, 1500459.

[142] D. Karnaushenko, T. Kang, V. K. Bandari, F. Zhu, O. G. Schmidt, *Adv. Mater.* **2019**, 1902994.

[143] G. G. Stoney, *Proc. R. Soc. London* **1909**, *82*, 172.

[144] P. Cendula, S. Kiravittaya, Y. F. Mei, C. Deneke, O. G. Schmidt, *Phys. Rev. B-Condens. Matter Mater. Phys.* **2009**, *79*, 085429.

[145] X. Wang, Y. Chen, O. G. Schmidt, C. Yan, *Chem. Soc. Rev.* **2016**, *45*, 1308.

[146] F. Gabler, D. D. Karnaushenko, D. Karnaushenko, O. G. Schmidt, *Nat. Commun.* **2019**, *10*, 3013.

[147] H. X. Ji, X. L. Wu, L. Z. Fan, C. Krien, I. Fiering, Y. G. Guo, Y. Mei, O. G. Schmidt, *Adv. Mater.* **2010**, *22*, 4591.

[148] J. Deng, H. Ji, C. Yan, J. Zhang, W. Si, S. Baunack, S. Oswald, Y. Mei, O. G. Schmidt, *Angew. Chem. Int. Ed.* **2013**, *52*, 2326.

[149] L. Zhang, J. Deng, L. Liu, W. Si, S. Oswald, L. Xi, M. Kundu, G. Ma, T. Gemming, S. Baunack, F. Ding, C. Yan, O. G. Schmidt, *Adv. Mater.* **2014**, *26*, 4527.

[150] X. Liu, J. Zhang, W. Si, L. Xi, B. Eichler, C. Yan, O. G. Schmidt, *ACS Nano* **2015**, *9*, 1198.

[151] Y. Chen, C. Yan, O. G. Schmidt, *Adv. Energy Mater.* **2013**, *3*, 1269.

[152] C. Yan, W. Xi, W. Si, J. Deng, O. G. Schmidt, *Adv. Mater.* **2013**, *25*, 539.

[153] X. Sun, C. Yan, Y. Chen, W. Si, J. Deng, S. Oswald, L. Liu, O. G. Schmidt, *Adv. Energy Mater.* **2014**, *4*, 1300912.

[154] S. Huang, L. Zhang, X. Lu, L. Liu, L. Liu, X. Sun, Y. Yin, S. Oswald, Z. Zou, F. Ding, O. G. Schmidt, *ACS Nano* **2017**, *11*, 821.

[155] J. Deng, C. Yan, L. Yang, S. Baunack, S. Oswald, H. Wendrock, Y. Mei, O. G. Schmidt, *ACS Nano* **2013**, *7*, 6948.

[156] X. Lu, J. Deng, W. Si, X. Sun, X. Liu, B. Liu, L. Liu, S. Oswald, S. Baunack, H. J. Grafe, C. Yan, O. G. Schmidt, *Adv. Sci.* **2015**, *2*, 1500113.

[157] W. Si, I. Mönch, C. Yan, J. Deng, S. Li, G. Lin, L. Han, Y. Mei, O. G. Schmidt, *Adv. Mater.* **2014**, *26*, 7973.

[158] D. D. Karnaushenko, D. Karnaushenko, D. Makarov, O. G. Schmidt, *NPG Asia Mater.* **2015**, *7*, e188.

[159] D. D. Karnaushenko, D. Karnaushenko, H. J. Grafe, V. Kataev, B. Büchner, O. G. Schmidt, *Adv. Electron. Mater.* **2018**, *4*, 1800298.

[160] D. Karnaushenko, T. Kang, O. G. Schmidt, *Adv. Mater. Technol.* **2019**, *4*, 1800692.

[161] S. M. George, *Chem. Rev.* **2010**, *110*, 111.

[162] C. A. Wilson, R. K. Grubbs, S. M. George, *Chem. Mater.* **2005**, *17*, 5625.

[163] A. E. Marquardt, E. M. Breitung, T. Drayman-Weisser, G. Gates, R. J. Phaneuf, *Herit. Sci.* **2015**, *3*, 37.

[164] X. Xia, D. Chao, Y. Zhang, J. Zhan, Y. Zhong, X. Wang, Y. Wang, Z. X. Shen, T. Jiangping, H. J. Fan, *Small* **2016**, *12*, 3048.

[165] S. Zheng, Z. Li, Z. S. Wu, Y. Dong, F. Zhou, S. Wang, Q. Fu, C. Sun, L. Guo, X. Bao, *ACS Nano* **2017**, *11*, 4009.

[166] D. Aradilla, M. Delaunay, S. Sadki, J. M. Gérard, G. Bidan, *J. Mater. Chem. A* **2015**, *3*, 19254.

[167] W. Liu, X. Yan, J. Chen, Y. Feng, Q. Xue, *Nanoscale* **2013**, *5*, 6053.

[168] W. Liu, Y. Feng, X. Yan, J. Chen, Q. Xue, *Adv. Funct. Mater.* **2013**, *23*, 4111.

[169] K. Guo, Y. Wan, N. Yu, L. Hu, T. Zhai, H. Li, *Energy Storage Mater.* **2018**, *11*, 144.

[170] Z. Liu, X. Tian, X. Xu, L. He, M. Yan, C. Han, Y. Li, W. Yang, L. Mai, *Nano Res.* **2017**, *10*, 2471.

[171] H. Xu, X. Hu, H. Yang, Y. Sun, C. Hu, Y. Huang, *Adv. Energy Mater.* **2015**, *5*, 1401882.

[172] Z. Li, M. Shao, L. Zhou, R. Zhang, C. Zhang, J. Han, M. Wei, D. G. Evans,

X. Duan, *Nano Energy* **2016**, *20*, 294.

[173] J. Yun, Y. Lim, H. Lee, G. Lee, H. Park, S. Y. Hong, S. W. Jin, Y. H. Lee, S. S. Lee, J. S. Ha, *Adv. Funct. Mater.* **2017**, *27*, 1700135.

[174] L. Sun, X. Wang, K. Zhang, J. Zou, Q. Zhang, *Nano Energy* **2016**, *22*, 11.

[175] J. Ren, L. Li, C. Chen, X. Chen, Z. Cai, L. Qiu, Y. Wang, X. Zhu, H. Peng, *Adv. Mater.* **2013**, *25*, 1155.

[176] C. Zhang, J. Xiao, L. Qian, S. Yuan, S. Wang, P. Lei, *J. Mater. Chem. A* **2016**, *4*, 9502.

[177] L. Li, J. Zhang, Z. Peng, Y. Li, C. Gao, Y. Ji, R. Ye, N. D. Kim, Q. Zhong, Y. Yang, H. Fei, G. Ruan, J. M. Tour, *Adv. Mater.* **2016**, *28*, 838.

[178] Y. Da, J. Liu, L. Zhou, X. Zhu, X. Chen, L. Fu, *Adv. Mater.* **2018**, 1802793.

[179] L. Qin, Q. Tao, A. El Ghazaly, J. Fernandez-Rodriguez, P. O. Å. Persson, J. Rosen, F. Zhang, *Adv. Funct. Mater.* **2018**, *28*, 1703808.

[180] M. Zhu, Y. Huang, Y. Huang, H. Li, Z. Wang, Z. Pei, Q. Xue, H. Geng, C. Zhi, *Adv. Mater.* **2017**, *29*, 1605137.

[181] J. Ye, H. Tan, S. Wu, K. Ni, F. Pan, J. Liu, Z. Tao, Y. Qu, H. Ji, P. Simon, Y. Zhu, *Adv. Mater.* **2018**, *30*, 1801384.

[182] L. Li, C. Fu, Z. Lou, S. Chen, W. Han, K. Jiang, D. Chen, G. Shen, *Nano Energy* **2017**, *41*, 261.

[183] Y. Nan, Z. Wang, *Handbook of Microscopy for Nanotechnology*, **2005**.

[184] **N.d.**, https://www.microchemicals.com/products/photoresis.

[185] G. A. Snook, G. Z. Chen, *J. Electroanal. Chem.* **2008**, *612*, 140.

[186] N. Kurra, M. K. Hota, H. N. Alshareef, *Nano Energy* **2015**, *13*, 500.

[187] N. Sakmeche, S. Aeiyach, J.-J. Aaron, M. Jouini, J. C. Lacroix, P.-C. Lacaze, *Langmuir* **1999**, *15*, 2566.

[188] S. Cosnier, A. Karyakin, *Electropolymerization: Concepts, Materials and Applications*, **2011**.

[189] J. Wang, V. K. Bandari, D. Karnaushenko, Y. Li, F. Li, P. Zhang, S. Baunack, D. D. Karnaushenko, C. Becker, M. Faghih, T. Kang, S. Duan, M. Zhu, X. Zhuang, F. Zhu, X. Feng, O. G. Schmidt, *ACS Nano* **2019**, *13*, 8067.

[190] Z. L. Wang, *Nano Today* **2010**, *5*, 512.

[191] P. Zhang, F. Wang, M. Yu, X. Zhuang, X. Feng, *Chem. Soc. Rev.* **2018**, 7426.

[192] M. R. Lukatskaya, B. Dunn, Y. Gogotsi, *Nat. Commun.* **2016**, *7*, 12647.

[193] A. Raj, D. Steingart, *J. Electrochem. Soc.* **2018**, *165*, B3130.

[194] L. Liu, H. Zhao, Y. Lei, *InfoMat* **2019**, 74.

[195] Y. Huang, M. Zhong, F. Shi, X. Liu, Z. Tang, Y. Wang, Y. Huang, H. Hou, X. Xie, C. Zhi, *Angew. Chem. Int. Ed.* **2017**, *56*, 9141.

[196] Y. Yue, Z. Yang, N. Liu, W. Liu, H. Zhang, Y. Ma, C. Yang, J. Su, L. Li, F. Long, Z. Zou, Y. Gao, *ACS Nano* **2016**, *10*, 11249.

[197] J. Tao, N. Liu, J. Rao, L. Ding, M. R. Al Bahrani, L. Li, J. Su, Y. Gao, *Nanoscale* **2014**, *6*, 15073.

[198] S. Wang, N. Liu, C. Yang, W. Liu, J. Su, L. Li, C. Yang, Y. Gao, *RSC Adv.* **2015**, *5*, 85799.

[199] N. Liu, W. Ma, J. Tao, X. Zhang, J. Su, L. Li, C. Yang, Y. Gao, D. Golberg, Y. Bando, *Adv. Mater.* **2013**, *25*, 4925.

[200] J. Rogers, Y. Huang, O. G. Schmidt, D. H. Gracias, *MRS Bull.* **2016**, *41*, 123.

[201] Y. Zhang, F. Zhang, Z. Yan, Q. Ma, X. Li, Y. Huang, J. A. Rogers, *Nat. Rev. Mater.* **2017**, *2*, 17019.

[202] S. Xu, Z. Yan, K. I. Jang, W. Huang, H. Fu, J. Kim, Z. Wei, M. Flavin, J. McCracken, R. Wang, A. Badea, Y. Liu, D. Xiao, G. Zhou, J. Lee, H. U. Chung, H. Cheng, W. Ren, A. Banks, X. Li, U. Paik, R. G. Nuzzo, Y. Huang, Y. Zhang, J. A. Rogers, *Science* **2015**, *347*, 154.

[203] A. M. Abdullah, X. Li, P. V. Braun, J. A. Rogers, K. J. Hsia, *Adv. Mater.* **2018**, *30*, 1801669.

[204] P. Cendula, S. Kiravittaya, I. Mönch, J. Schumann, O. G. Schmidt, *Nano Lett.* **2011**, *11*, 236.

[205] C. Xu, X. Wu, G. Huang, Y. Mei, *Adv. Mater. Technol.* **2018**, 1800486.

[206] M. Medina-Sánchez, B. Ibarlucea, N. Pérez, D. D. Karnaushenko, S. M. Weiz, L. Baraban, G. Cuniberti, O. G. Schmidt, *Nano Lett.* **2016**, *16*, 4288.

[207] A. R. Jalil, H. Chang, V. K. Bandari, P. Robaschik, J. Zhang, P. F. Siles, G. Li, D. Bürger, D. Grimm, X. Liu, G. Salvan, D. R. T. Zahn, F. Zhu, H. Wang, D. Yan, O. G. Schmidt, *Adv. Mater.* **2016**, *28*, 2971.

[208] W. Huang, J. Zhou, P. J. Froeter, K. Walsh, S. Liu, M. D. Kraman, M. Li, J. A. Michaels, D. J. Sievers, S. Gong, X. Li, *Nat. Electron.* **2018**, *1*, 305.

[209] G. Wang, X. Lu, Y. Ling, T. Zhai, H. Wang, Y. Tong, Y. Li, *ACS Nano* **2012**, *6*, 10296.

[210] N. Kurra, M. K. Hota, H. N. Alshareef, *Nano Energy* **2015**, 500.

[211] J. Lin, C. Zhang, Z. Yan, Y. Zhu, Z. Peng, R. H. Hauge, D. Natelson, J. M. Tour, *Nano Lett.* **2013**, *13*, 72.

[212] C. Meng, J. Maeng, S. W. M. John, P. P. Irazoqui, *Adv. Energy Mater.* **2014**, *4*, 1301269.

[213] P. Huang, C. Lethien, S. Pinaud, K. Brousse, R. Laloo, V. Turq, M. Respaud, A. Demortière, B. Daffos, P. L. Taberna, B. Chaudret, Y. Gogotsi, P. Simon, *Science* **2016**, *351*, 691.

[214] E. Eustache, C. Douard, A. Demortière, V. De Andrade, M. Brachet, J. Le Bideau, T. Brousse, C. Lethien, *Adv. Mater. Technol.* **2017**, *2*, 1700126.

[215] J. H. Pikul, H. Gang Zhang, J. Cho, P. V. Braun, W. P. King, *Nat. Commun.* **2013**, *4*, 1732.

[216] M. Beidaghi, C. Wang, *Adv. Funct. Mater.* **2012**, *22*, 4501.

[217] X. Wang, B. D. Myers, J. Yan, G. Shekhawat, V. Dravid, P. S. Lee, *Nanoscale* **2013**, *5*, 4119.

[218] G. Li, M. Yarali, A. Cocemasov, S. Baunack, D. L. Nika, V. M. Fomin, S. Singh, T. Gemming, F. Zhu, A. Mavrokefalos, O. G. Schmidt, *ACS Nano* **2017**, *11*, 8215.

[219] Z. S. Wu, K. Parvez, S. Li, S. Yang, Z. Liu, S. Liu, X. Feng, K. Müllen, *Adv. Mater.* **2015**, *27*, 4054.

[220] C. J. Zhang, M. P. Kremer, A. Seral-Ascaso, S. H. Park, N. McEvoy, B. Anasori, Y. Gogotsi, V. Nicolosi, *Adv. Funct. Mater.* **2018**, *28*, 1705506.

[221] J. Q. Xie, Y. Q. Ji, J. H. Kang, J. L. Sheng, D. S. Mao, X. Z. Fu, R. Sun, C. P. Wong, *Energy Environ. Sci.* **2019**, *12*, 194.

[222] N. A. Kyeremateng, T. Brousse, D. Pech, *Nat. Nanotechnol.* **2016**, *12*, 7.

[223] M. F. El-Kady, M. Ihns, M. Li, J. Y. Hwang, M. F. Mousavi, L. Chaney, A. T. Lech, R. B. Kaner, *Proc. Natl. Acad. Sci.* **2015**, *112*, 4233.

[224] X. Wang, Y. Yin, X. Li, Z. You, *J. Power Sources* **2014**, *252*, 64.

[225] E. Eustache, C. Douard, A. Demortière, V. De Andrade, M. Brachet, J. Le Bideau, T. Brousse, C. Lethien, *Adv. Mater. Technol.* **2017**, *2*, 1700126.

[226] J. Pu, X. Wang, T. Zhang, S. Li, J. Liu, K. Komvopoulos, *Nanotechnology* **2016**, *27*, 045701.

[227] D. P. Dubal, D. Aradilla, G. Bidan, P. Gentile, T. J. S. Schubert, J. Wimberg, S. Sadki, P. Gomez-Romero, *Sci. Rep.* **2015**, *5*, 9771.

[228] A. Ponrouch, S. Garbarino, E. Bertin, D. Guay, *J. Power Sources* **2013**, *221*, 228.

[229] T. M. Dinh, A. Achour, S. Vizireanu, G. Dinescu, L. Nistor, K. Armstrong, D. Guay, D. Pech, *Nano Energy* **2014**, *10*, 288.

[230] H. Li, J. Song, L. Wang, X. Feng, R. Liu, W. Zeng, Z. Huang, Y. Ma, L. Wang, *Nanoscale* **2017**, *9*, 193.

[231] D. Grimm, C. C. Bof Bufon, C. Deneke, P. Atkinson, D. J. Thurmer, F. Schäffel, S. Gorantla, A. Bachmatiuk, O. G. Schmidt, *Nano Lett.* **2013**, *13*, 213.

[232] Y. Wang, Y. Song, Y. Xia, *Chem. Soc. Rev.* **2016**, *45*, 5925.

List of Figures

List of Tables

Theses

1. Demanded by next-generation microelectronics, the research on micro-supercapacitors integrated with more functions has aroused great interest in recent years.
2. Constructing the 3D electrode for micro-supercapacitors architectures is an effective strategy to increase the areal performance under a limited footprint area.
3. The interdigital electrode is a common configuration used in micro-supercapacitors, owing to its advantage in the microfabrication process.
4. Rolled-up technology is a unique approach to self-assemble 2D films into 3D structures in micro/nanoscale by using strain engineering.
5. One promising advantage of rolled-up technology is that the rolled-up structure can endow micro-devices (*e.g.* supercapacitor) with high areal performance.
6. The strained layer used in rolled-up technology is divided into two categories: inorganic nanomembrane and polymeric layer stacks.
7. Electrochemical deposition is a method using the redox reaction to synthesize active materials with the micro/nanoscale thickness and a high specific area for supercapacitors.
8. Micro-supercapacitors array is designed and fabricated through the combination between photolithography and electrochemical deposition method.
9. Interdigital electrodes are rolled into the tubular hydrogel/polyimide strained layer. The hydrogel layer is covered on the electrode surface, moisturizing the electrodes and generating an efficient pathway for ion transport.
10. The robust structure of the polymeric layer provides efficient protection against external compression.
11. Tubular micro-supercapacitors possess greatly improved areal electrochemical performance, compared to that of the planar micro-supercapacitor.

12. The enhanced cycling stability for tubular micro-supercapacitors is observed, owing to the efficient strain accommodation of electrodes in the tubular structure.
13. Free-standing tubular micro-supercapacitors can be transferred to different substrates and assembled in parallel/series to improve the specific voltage and capacitance.
14. Under the assist of magnetic fields, a high-aspect-ratio electrode of micro-supercapacitor can be self-assembled into “Swiss-roll” architecture through the strain release of the inorganic nanomembrane.

Acknowledgment

At this point I would like to acknowledge all the people who have helped me complete this thesis.

First and foremost, I would like to thank my supervisor Prof. Dr. Oliver G. Schmidt for giving me the opportunity to study in IIN Chemnitz. Under his supervision and support, wonderful research works are successful completed. It has been an honor to be his PhD student.

I would like to thank my second supervisor Prof. Dr. Feng Zhu for his kind help, guidance, and discussion in these four years. His encouragement and enthusiasm brought me through difficult periods in this time.

I would like to thank the China Scholarship Council for the financial support of my study.

I would like to thank Dr. Panpan Zhang, Prof. Xiaodong Zhuang, and Prof. Xinliang Feng in TU Dresden for his experimental experience sharing and collaboration.

Next, I would like to thank Vineeth Kumar Bandari for his suggestion in microfabrication process. Many thanks go to Paul Plocica and Eric Pankenin for their technical help in the lab. Thank Yucheng Zhu and Chen Liu for their fabrication work on my projects. Thank Dr. Stefan Baunack, Shaista Andleeb and Somayeh Moradi for their help in SEM measurements. Thank Dr. Daniil Karnaushenko for his support for experiment materials. Thank Lixiang Liu for her discussion and the help for XRD measurements. Thank Dr. Junwen Deng, Dr. Xueyi Lu, Dr. Xiaolei Sun and Dr. Yin Yin for their experience sharing on experiments. Thanks also to Dr. Minshen Zhu, Fei Li, Jiang Qu, Yang Li, Shengkai Duan and Tianming Li, for the discussion on experiments and helps on my life. Many thanks Felix Gabler for helping me fabricate magnetic nanomembranes. I would like also to thank my other colleagues who are always willing to help me from all aspects: Ronny Engelhard, Dr. Libo Ma, Karthikeyan Loganathan Manga, Yue Gu, Subao Shi, Yang Nan, Bingkun Sun, Zhe Li, and Yu Hong.

Lastly, I would like to acknowledge the contribution of my parents, grandparents and parents in law. Especially I want to thank my wife Lixiang Zhang for all her support. I am very grateful to her for bringing our son Qingchen Wang to the world during the PhD pursuit. In order to support my study, she gave up her job and was fully raising our child.

Publications and presentations

Peer-review papers

1. **J. Wang,** V. K. Bandari, D. Karnaushenko, Y. Li, *et al. Self-Assembly of Integrated Tubular Microsupercapacitors with Improved Electrochemical Performance and Self-Protective Function.* ***ACS Nano,*** 2019, 7, 8067-8075.
2. **J. Wang**, F. Li, F. Zhu, and O. G. Schmidt. *Recent Progress in Micro-Supercapacitor Design, Integration, and Functionalization.* ***Small Methods,*** 2019, 8, 1800367.
3. F. Li, **J. Wang,** L. Liu, J. Qu, *et al. Self-Assembled Flexible and Integratable 3D Microtubular Asymmetric Supercapacitors*. ***Advanced Science,*** 2019, 1901051. (Contribute equally to the first author)
4. P. Zhang, **J. Wang,** W. Sheng, F. Wang. *et al. Thermoswitchable On-Chip Microsupercapacitors: One Potential Self-Protection Solution for Electronic Devices.* ***Energy & Environmental Science,*** 2018, 7, 1717-1722. (Contribute equally to the first author)
5. P. Zhang, F. Zhu, F. Wang, **J. Wang,** *et al. Stimulus-Responsive Micro-Supercapacitors with Ultrahigh Energy Density and Reversible Eectrochromic Window.* ***Advanced Materials,*** 2017, 7, 1604991-1604498.

Presentations

1. **J. Wang**, “Rolled-up Liquid Electrolyte Based Micro-Supercapacitors”, Talk, PhD Seminar, IFW Dresden, Germany, 07.03.2017.

1. **J. Wang**, “On-Chip and Free-standing Integrated 3D Tubular Micro-supercapacitors”, Talk, PhD Seminar, IFW Dresden, Germany, 25.04.2018.

2. **J. Wang**, “3D Micro-Energy Storage Based on Rolled-up and Microfabrication Techniques”, Talk, PhD Seminar, IFW Dresden, Germany, 25.06.2019.

Curriculum Vita

Personal Information

Name: Jinhui Wang

Date of Birth: 12.01.1988

Place of Birth: Shandong, China

Nationality: Chinese

Education

12/2015-07/2020	Ph.D. student in Leibniz Institute for Solid State and Materials Research Dresden (IFW), and Chemnitz University of Technology, Germany
09/2012-07/2015	Master of Material science and engineering, Beijing University of Chemical Technology (BUCT), China
09/2012-07/2015	Bachelor of Material science and engineering, Liaocheng University, China